Measurement of Charm and Beauty Jet Cross Sections in Neutral Current Deep Inelastic Scattering at HERA

THE UNIVERSITY
of LIVERPOOL

Thesis submitted in accordance with the requirements of the University of Liverpool for the degree of Doctor in Philosophy

by

Ahmad Jawade Rahmat

September 2008

Oliver Lodge Laboratory
University of Liverpool

Abstract

The cross section for charm and beauty jets is measured in neutral current deep inelastic scattering in $e^{\pm}p$ collisions at HERA II.

The data set used is based on an integrated luminosity of 189 pb^{-1} and was recorded using the H1 detector in 2006 and 2007. A method, based on the distance of closest approach of the track to the primary vertex, is used to identify the fractions of events associated with heavy-flavoured mesons. The charm and beauty jet cross sections are measured in the visible ranges of the leading jet transverse momentum of $P_T^{Jet} > 6\ GeV/c$, and pseudorapidity $|\eta^{jet}| < 1.5$. The measurements are made in the range of inelasticity $0.07 < y < 0.63$, Bjorken scaling variable $0.0002 \leq x \leq 0.032$, and four momentum transferred $5 \leq Q^2 \leq 1585\ GeV^2$ .The cross sections are presented as a function of the transverse momentum and pseudo-rapidity of the leading jet. The measurements are compared with NLO QCD predictions.

"One day Chuang Tzu fell asleep, and while he slept he dreamed that he was a butterfly, flying happily about. And this butterfly did not know that it was Chuang Tzu dreaming. Then he awoke, to all appearances himself again, but now he did not know whether he was a man dreaming that he was a butterfly or a butterfly dreaming that he was a man."

-THE TEACHINGS OF CHUANG TZU

"Charm is deceptive and beauty is fleeting "

(Proverbs 31:30, RSV)

Dedications

This thesis is dedicated to;

The fond memory of my dad, Dr.A.Rahmat (1940-2008),

Angela

and our beloved son, Gabriel.

Acknowledgement

Every journey, every expedition, starts with one person and ends with the help of others, and this one is no exception. Hereby I gratefully acknowledge the help and assistance of others without whom this work that lies within these pages would not have been.

Physics World: I am indebted to the following people, groups and organisations for their help, patience, assistance and countless useful discussions;

My supervisor Prof.T.Greenshaw for being supportive and for his help in the proof reading of this work.

Dr.A.Mehta"my surrogate supervisor" for all his help and assistance in the analysis side and for his help with the proof reading of this work, for his invaluable discussions and insights for being thorough, thank you very much. Also Dr.P.Thompson from Birmingham University, I am very grateful for all your help and assistance with the analysis, thank you.

Dr.S.Maxfield for his help with the proof reading of this document in its entirety. For his generosity and depth of knowledge in this field and many invaluable discussions and corrections, for being meticulous and thorough, thank you very much. Dr.B.King for being nice and convivial and for asking me how my son is doing. Thank you. Dr.C.Touramanis for always being encouraging. All the H1 physics community abroad and here in Liverpool, thank you. Susan-Katrin Ketels, the student-liaison officer in Hamburg, thanks for being very kind and efficient.

Mrs.Norma Riding, from physics canteen, thanks for always being nice and feeding us.

Rev.P.Rossiter and Mr.P.Davenport, thank you for always smiling.

Thanks are also due to the Particle Physics and Astrophysics Research Council (now STFC) for their financial support for the first three years of this work.

Fellow Ph.D students past and present: I would like to thank (anti-clockwise) Dr.P.Prideaux, Dr.A.Rimmer, A.Mohamed, Dr.C.Veelken for being very helpful and good company while I was stationed in Hamburg. I would also like to thank T. Woollioscroft, N.Almond and Dr.D.Scraggs for being good friends.

Thanks are due also to (clockwise) P.Prichard, M.Flowerdew, I.Bingham, L.Dwyer and N.Austin for making the office in the last six months of this work bearable.

The World outside Physics: I would like to thank Mr.K.Douglas for being a very nice and understanding person and for giving me time off, from my weekend job, to concentrate on writing this thesis, I am very grateful, thanks.

It is unfortunate that time did not allow my dad to see this thesis, I am sure he would have been very proud, I love you dad and I will always miss you, thanks for all that you have done for me. To my mum, thanks for being there and for being supportive. To my brother, thank you for being the best brother and a very good friend.

To my girlfriend, Angela, I am so lucky to have you, thanks for always believing in me even when I didn't believe in myself, for your love, for being kind, for being the best mum I have ever seen, and for giving me a home, a family, a sense of belonging, for putting up with me for the past thirteen years, I hope we can be together till the end. Thank you, without you none of this would have been possible.

Finally, to my son, Gabriel, you are the reason that everyday is beautiful and meaningful, I am sorry that I missed so much of your growing up, I hope this thesis will justify my absence and not being there for you, when you took your first step, when you were ill and needed someone to comfort you, I doubt that it would, but you were always there with me giving me a reason to carry on. Thanks for gracing our lives with your presence. Also big thanks for hugging me when I was sad and for the Eskimo kisses.

Contents

1 Introduction 14

2 H1 Experiment at HERA 17

2.1 Introduction 17

2.2 The HERA Accelerator 18

2.3 The H1 Detector 20

2.3.1 Gaseous Tracking Detectors 24

2.3.2 Central Track Detector 25

2.3.3 Central Silicon Tracker 28

2.3.4 Hit Finding 31

2.3.5 The Forward Tracker 31

2.3.6 Backward Drift Chamber 31

2.4 Calorimetry 32

2.4.1 The H1 Calorimeters 33

2.4.2 Liquid Argon Calorimeter 34

2.4.3 The Spaghetti Calorimeter 36

2.5 The Luminosity System 38

2.6 Trigger System and Data Acquisition 40

2.6.1 The SpaCal Trigger 45

2.7 The Detector Simulation 47

3 Theoretical Overview 48

3.1 The Kinematics of *ep* Scattering 50

3.2 DIS: Probing the structure of the Proton 55

3.2.1 Scaling and the Quark-Parton Model 59

3.2.2 QCD evolution 61

3.2.3 DGLAP evolution 63

3.2.4 BFKL evolution 66

3.2.5 CCFM evolution 67
3.2.6 Radiative QED Corrections 70
3.3 Production Mechanism of Heavy Quarks in DIS 70
3.4 Hadronisation 78
3.5 Monte Carlo Event Generators 81
4 Event Selection 84
4.1 Data set 84
4.2 Kinematics 85
4.3 DIS and Jet Event Selection 85
4.4 Trigger Selection 87
4.5 DIS Control Plots 89
4.6 Track Selection 93
4.7 Calibration 94
4.8 Rejection of Non-*ep* Background 95
5 Event Reconstruction 97
5.1 Analysis Strategy 97
5.1.1 Experimental Signatures of Heavy Quarks 98
5.1.2 Impact Parameter 99
5.1.3 Decay Length 103
5.2 Track and Vertex Reconstruction determination 104
5.2.1 Track Reconstruction 104
5.2.2 CST improved tracks 106
5.2.3 Reconstruction of the Primary Vertex 107
5.3 Impact Parameter Resolution 108
5.3.1 Track Resolution 109
5.3.2 Track Finding Efficiency 111
5.4 HFS Reconstruction and Jet Finding 115
5.4.1 HFS Reconstruction 115

5.4.2 Jet Finding 117
6 Flavour Separation 119
6.1 Lifetime Tagging Method 121
6.1.1 Jet Axis 122
6.1.2 Matching of Tracks to Quark Axis 123
6.1.3 Details of the Track Selection 124
6.2 Impact Parameter and Significance in Lifetime tagging 127
6.2.1 Impact Parameter 127
6.2.2 Significance 129
6.3 Fit Procedure 135
7 The Results 137
7.1 The Cross Section 137
7.2 Determination of the Cross Sections 138
7.3 The Measured Differential Cross Sections 139
7.4 Systematic Errors 143
7.5 Comparison with the Leading Order Models 148
7.6 Next-to-Leading Order Calculations 149
8 Conclusion 153
Appendices 155
A Tables of Results 156
B Reconstruction Methods 160
C Running Coupling Constant 163
D Example Events in H1 Detector 166
References 171

List of Figures

2.1: The HERA accelerator (left) and its pre-accelerator, PETRA (right). **18**

2.2a: The H1 detector. **21**

2.2b: r z-view of the tracking system and calorimeters of the H1 detector. The layout of the central silicon tracker (CST) is shown separately below in a larger scale. The dashed and full lines indicate the polar angle acceptance borders for tracks measured with high quality in the CST and the central drift chambers (CJC), respectively. The dotted lines indicate the typical minimal and maximal polar angles for selected jets which are reconstructed in the LAr calorimeter. **23**

2.3: Schematic drawing of a single cell of a gaseous tracking detector: the upper picture shows a cross section along the electric field direction in the detector and the lower picture cross sections transverse to the electric field. **24**

2.4: Drawings of an MWPC: the sketch on the left depicts a single MWPC, whereas that on the right shows a multi-layered MWPC in which each dot represents a wire, viewed end on. A particle, deflected by a magnetic field, "hits" a series of wires and from these hits the measured trajectory shown as the curved arrow can be deduced. **25**

2.5: A vertical cross section through the H1 tracking system, showing the central, forward, and silicon trackers and the backward drift chamber (BDC). **26**

2.6: Radial view of the CTD, showing the cells of the CJC1 and CJC2. ..... **28**

2.7: A radial view of the CST. **29**

2.8: a) Two views of the half ladders from which the CST is constructed: left p side; right n side. b) Side view of the interaction region of the H1 detector. The three silicon strip detectors FST, CST and BST are indicated. **30**

2.9: The layout of the H1 calorimeters shown in the r-z plane: the LAr calorimeter consists of an electromagnetic (EMC) and hadronic (HAC) part; to the rear of the detector is the SpaCal,

which also has electromagnetic and hadronic sections; surrounding the entire detector is the tail catcher or backing calorimeter which also serves as a muon detector. **34**

2.10: Side view of LAr in the r-ϕ plane, showing (in the upper half) the orientation of the absorber layers and (in the lower half) the segmentation of the read-out cells. **36**

2.11: Cross section of the backward region of the H1 Detector showing the electromagnetic and hadronic sections of the SpaCal. **37**

2.12: The H1 Luminosity System.....**39**

2.13: An overview of the event rates in the H1 Trigger System. **41**

2.14: A schematic overview of the L1 and L4 trigger systems. **42**

2.15: The $\mathrm{r}\phi$ view of a charged particle track from the interaction point traversing the central drift chambers of the H1 detector. The sense and cathode wires of the chambers are indicated **44**

2.16: Typical time distribution of signals in the SpaCal as shown by the online histogram system. The left peak corresponds to proton beam related background, while the right peak shows the position in time of ep interactions. **46**

2.17: Side view (left figure) and radial view (right figure) of low Q^2 DIS event in H1 detector. The scattered positron is detected in the SpaCal. **47**

3.1: Virtual boson exchange in ep scattering via NC (left) and CC (right) interactions 51

3.2: Kinematics of ep scattering. 51

3.3: Deep Inelastic Scattering. The incident electron, scattered lepton, exchange boson and proton have four-momenta $\kappa^{\mu}, \kappa^{'\mu}, q^{\mu}$ and p^{μ} respectively. 55

3.4: Cross-section for Neutral Current (blue) and Charge Current (red) as a function of Q^2 [30] **56**

3.5: Proton structure function $F_2(x,Q^2)$ as a function of Q^2 for a range of different x values. **58**

3.6: Illustration of proton structure as observed at different Q^2 value....**61**

3.7: The proton structure function $F_2(x, Q^2)$ as a function of Bjorken x. **62**

3.8: Graphs of the leading order DGLAP *splitting functions* $P_{ij}^{(0)}(x/y)$ *for* $P_{qq}(q \longrightarrow qg)$, $P_{qg}(g \longrightarrow q\bar{q})$, *and for* $P_{gg}(g \longrightarrow gg)$ *splitting(from left).* **64**

3.9: Feynman diagrams contributing to the Next to Leading Order (NLO) splitting functions $\mathrm{P}_{\mathrm{qq}}^{(1)}$ and $\mathrm{P}_{\mathrm{q\bar{q}}}^{(1)}$. **64**

3.10: Schematic phase space diagram for deep inelastic scattering. Directions of DGLAP and BFKL evolutions are marked by arrows. In the non-perturbative regions $Q^2 < \Lambda^2_{QCD}$ (blue *rectangle) the coupling is large and not much is known here in terms of perturbative QCD. The saturation region (yellow area) an be understood by means of perturbative methods at low x.* **66**

3.11: Feynman diagrams of the first order QED corrections to the lepton-quark scattering corresponding to the initial (a) and final (b) state radiation of the photon from the interacting electron. **69**

3.12: The left plot illustrate the dominant production process for charm and beauty quarks in ep collision at HERA, the photon gluon fusion (PGF) reaction. The right plot depicts for comparison the simplest diagram for light quark scattering **71**

3.13: Leading order resolved photon diagrams for charm and beauty production in the massive scheme (left) and in the massless scheme (right). **72**

3.14: Running coupling constant α_s of the strong force as a function of hard scale μ 72

3.15: Gluon density in the proton as a function of the proton momentum fraction x carried by the gluon for three different values of the photon virtuality Q2, as determined from the scaling violations of the inclusive structure function F_2. .....**73**

3.16: Factorisation of heavy flavour production in QCD in proton structure, photon structure, hard matrix element and fragmentation (left).Illustration of factorisation principle (right). **74**

3.17: Leading diagrams for heavy quark production in the massless scheme at leading order (a) and next-to-leading order (b-d). **75**

3.18: Possible hard scales in the photon gluon fusion process. **75**

3.19: Leading diagrams for heavy quark production in the massive scheme at leading order (a) and next-to-leading order (b-d). **77**

3.20: Leading order diagrams for charm production in DIS in the variable flavour number scheme: On the left the QPM diagram is shown, on the right the PGF diagram and the middle the 'subtraction diagram'. **78**

3.21: Illustration of the Lund string hadronisation model. a) The tube-like colour field between a quark and an anti-quark according to the QCD potential(cf. equation 3.44). b) Formation of colourless hadrons according to the Lund fragmentation model. **79**

3.22: Peterson fragmentation functions for charm and beauty (next-to-leading order parameters ϵ_c and ϵ_b are used). **80**

3.23: Principle layout of an event generator with initial and final state parton shower (PS), leading order matrix element (ME) and hadronisation. **82**

4.1: Control distributions after selection cuts and trigger selection for the values of of $\log_{10} Q^2$ (left) and inelasticity, y(right). **90**

4.2: The scattered electron energy spectrum (left) and polar angle θ.(right) for the DIS event sample. **90**

4.3: The Z position of the primary interaction vertex (left) and x_{Bj}.(right) for the DIS event sample. **91**

4.4: The distribution of the variable $E - P_z$ for the DIS event sample. **92**

4.5: The distribution of ϕ for the DIS event sample **92**

4.6: Control distributions after selection cuts and trigger selection for the values of of $\log_{10}Q^2$, $\log_{10}x$, energy of the scattered positron E, θ and ϕ angles of the scattered positron and the z coordinate of the vertex position. **93**

4.7: The transverse momentum P_T (left figure) and the angle θ (right figure) of all CST tracks. The contributions from various quark flavours are shown after applying the scale factors obtained from the fit to the subtracted significance distributions of the data (cf. Chapter 6). ..**94**

4.8: The distribution of the P_T balance **95**

5.1: Schematic illustration of impact parameter in the $r\phi$-plane. **100**

5.2: Sign convention of the impact parameter δ. **102**

5.3: The signed impact parameter δ of a track, shows symmetric (asymmetric) distribution of light flavour shown in green (heavy flavour, shown in blue and red) events around zero, . **103**

5.4: The track parameters $(\kappa, \phi_0, \theta, dca, z_0)$ describe the helix in a) the $r\phi$ and b) the z s plane with respect to the origin of the H1 coordinate system. **105**

5.5: CST track reconstruction. **107**

5.6: Schematic view of the various contributions to impact parameter resolution [71]. The table on the right shows these contribution in HERA I and HERA II (in which the data for this analysis were gathered), hence the resolution of the detector is superior in HERA II phase of operation compared with HERA I phase. **109**

5.7: Shows the link probability, P_{link},, for matching successfully one(more than one) CJC track(s) to a CST hit(s) on the left plot (on the right plot).The data (solid black points with error bars) are adequately described by Monte Carlo (solid black line) the difference is due to the CJC error description **110**

5.8: The efficiency of one or more CST hits is shown above and it was found to be 91% for e^-p (left) and 95% for e^+p (right). The Monte Carlo efficiency is shown separately for the default (dashed red line) and modified (solid black line) version. The solid black dots are the data. .. **111**

5.9: CST track finding efficiency for tracks with at least 2 CST hits and $P_{link} > 0.001$ as function of P_T^{track}(a) and z_{CST}(b). The Monte Carlo efficiency is shown separately for the default (dashed red line) and modified (solid black line) version. The distribution of the data are shown as the solid black dots. **112**

5.10: Gaussian width of dca_{RV} distribution as a function of the track direction around the beam. Tracks with at least two CST hits and $P_T > 0.3\ GeV$ are shown for data (black dots) and

simulation by RAPGAP (red dots). The shape of the curve corresponds to $\sim \sigma_x^2 \sin^2(\phi) + \sigma_y^2 cos^2(\phi)$ with parameter $\sigma_x = 90\ \mu m$ and $\sigma_y = 20\ \mu m$. On the right the distribution is shown as a function of P_T and it can be seen that the resolution improves with increase in P_T. **113**

5.11: The error on DCA, the contribution from data and Monte Carlo simulation are shown. **114**

5.12: Illustrates the different ranges for Central (green), Combined(blue) and Forward (red) tracks with regards to the angle θ[58] **116**

6.1: Basic tagging methods for heavy flavour events. **120**

6.2: The number of jets per event. The contributions from the various quark flavours are shown in different colours. **122**

6.3: Illustration of the distance of the closest approch (DCA) and quark axis in rϕ-plane. **123**

6.4: The number CST tracks per event before (left figure) and after (right figure) track association to the quark axis **124**

6.5: Control distributions of the selected tracks. The expectation from RAPGAP Monte Carlo simulation is included in the figures (black solid lines), the contribution from different flavours are shown (colour coded).In the last couple of plots (track length and number of CST hits) only the total expectation from MC (solid blue) and the data(solid dots) are shown. **126**

6.6: Distribution of the reconstructed impact parameter (left) and its error (right).The data is well described by the Monte Carlo simulation. The asymmetric distribution of heavy quarks can be observed (red and blue colours) with a positive skew, whereas the light quarks (green) distribution is symmetric around zero.. ..... **128**

6.7: Distribution of the reconstructed impact parameter with $|\delta| < 0.1\ cm$ cut. **129**

6.8: Distribution of the significance for all tracks with a cut of $|\delta| < 0.1\ cm$. The simulation from RAPGAP Monte Carlo is included in the figure, showing the contributions from the various quark flavours (colour coded) after applying the scale factors obtained from the fit to the subtracted significance distributions of the data(see section 6.3) **130**

6.9: The significance distribution (a) first significance, S_1 (b) second significance, S_2(c) and the third highest absolute significance S_3 of the selected tracks. Included in the figure is the expectation from Monte Carlo simulation for light, c and b quarks. The contributions from various quark flavours are shown after applying the scale factors (see section 6.3) obtained from the fit to the data. **132**

6.10: The subtracted distributions of S_1, S_2 and S_3. The figures include the expectation from Monte Carlo simulation and show the different contribution from various quark flavours after applying the scale factors (see section 6.3) obtained from the fit to the data. **133**

6.11: The significance and the subtracted distributions of S_1, S_2 and S_3 for bin 6 GeV $> P_T >$ 8 GeV1. The figures include the expectation from Monte Carlo simulation and show the

contributions from various quark flavours after applying the scale factors obtained from the fit to the data. **134**

7.1: Differential charm and beauty jets cross sections. The figure on the left (right) shows Beauty (Charm) jet cross section as a function of transverse momentum of the leading jet, $^{d\sigma}/_{dp_T}$. The solid black dots are the data points, the inner error bars indicate the statistical uncertainty and the outer error bars shows the statistical and systematic errors added in quadrature. The solid blue line (red) shows the expectations of the RAPGAP (CASCADE) Monte Carlo. As it can be observed from the plots, the data are well described by RAPGAP Monte Carlo in comparison to the CASCADE Monte Carlo expectation. **140**

7.2: Differential charm and beauty jets cross sections. The figure on the left (right) shows Beauty (Charm) jet cross section as a function of pseudorapidity of the leading jet, $^{d\sigma}/_{d\eta}$. The solid black dots are the data points, the inner error bars indicate the statistical uncertainty and the outer error bars shows the statistical and systematic errors added in quadrature. The solid blue line (red) shows the expectations of the RAPGAP (CASCADE) Monte Carlo. **140**

7.3: The significance distributions S_1, S_2 and S_3 in linear (left figures) and logarithmic (right figures) scales for the interval $4 < P_T \leq 6$ GeV. The Monte Carlo expectations are also shown before (black lines) and after (red dashed lines) DCA smearing. **145**

7.4: Differential charm and beauty jets cross-sections normalised, so that the area under the curve is unity, as a function of the transverse momentum of the leading jet for beauty (top-left) and charm (top-right) Also shown are the normalised cross sections as a function of pseudorapidity of the leading jet for beauty (bottom-left) and charm (bottom-right). The solid black dots are the data points, the inner error bars indicate the statistical uncertainty and the outer error bars shows the statistical and systematic errors added in quadrature. The solid blue line (red) shows the expectations of the RAPGAP (CASCADE) Monte Carlo. **146**

7.5: The mass of two tracks for the negative subtracted events with $0.1 < |\delta| < 0.5\ cm$ for e^-p (e^+p) left (right). Also shown in the plots are the contribution from the variation of the expectation of Monte Carlo by $\pm 30\%$. **147**

7.6: Predictions of the NLO calculation with (red lines) and without (blue) hadronisation corrections applied are compared with the measured differential cross sections as functions of P_T for beauty jets (top-left) and for charm jets (top-right) and with $^{d\sigma}/_{d\eta}$ for beauty jets (bottom-left) and charm jets (bottom-right). The figure also shows the NLO predictions after varying the scales $\mu_r^2 = \mu_f^2 = (m_h^2 + P_T^2)$ by factors of 4 (red dotted lines) and ¼ (red dash-dotted lines). **152**

D.1: Shows an example of a NC event with high Q^2 in the H1 Detector from HERA II data taking period. **166**

D.2: Cosmic (top) and halo-muon (bottom) events in H1 Detector. **167**

D.3: Beam-gas event in the H1 detector. **167**

D.4: Shows the precision of the Central Silicon Detector (CST), which measures the hits very precisely (10 micometer) which in turn is instrumental in search for the decay length or secondary vertices of the heavy quark (charm, bottom) decays, the event is from HERA I data taking period. **168**

D.5: Shows a NC DIS event with a single jet **169**

D.6: Shows a scattered electron with final state QED radiation. **170**

List of Tables

4.1: The trigger element composition of ST 61. The logical operators used in the definition are "&&" for "and", " **| |**" for "or" and "!" for a logical "not". **88**

5.1: Fragmentation fractions of c quarks to charm hadrons ([63]) (left table) and of b quarks to beauty hadrons [64] (right table). **98**

5.2: Properties of some charm and beauty hadrons [65]. **99**

5.6: The table on the right shows these contribution in HERA I and HERA II (in which the data for this analysis were gathered), hence the resolution of the detector is superior in HERA II phase of operation compared with HERA I phase. **109**

6.1: Track selection criteria. **125**

7.1: The measured differential cross section of charm jet together with statistic, systematic, and total errors for each individual P_T interval are listed. Also shown in the tables are the Hadronisation and QED correction factors for each P_T interval. **141**

7.2: The measured differential cross section of beauty jet together with statistic, systematic, and total errors for each individual P_T interval are listed. Also shown in the tables are the Hadronisation and QED correction factors for each P_T interval. **142**

7.3: The measured differential cross section of charm jet together with statistic, systematic, and total errors for each individual η interval are listed. Also shown in the tables are the Hadronisation and QED correction factors for each corresponding η interval. **142**

7.4: The measured differential cross section of beauty jet together with statistic, systematic, and total errors for each individual η interval are listed. Also shown in the tables are the Hadronisation and QED correction factors for each corresponding η interval. **143**

7.5: The systematic errors **148**

Chapter 1

" All science is either Physics or stamp collecting."
Ernest Rutherford

Introduction

In particle physics the properties of the constituents of matter and their interactions are investigated. To date the microscopic world is described very successfully by the "Standard Model" (SM) of particle physics. In SM the fundamental building blocks of matter are six quarks and six leptons. They interact via different forces, the electroweak and strong interactions. The theory of the strong force is described by Quantum Chromo Dynamics (QCD) which is central to this thesis and it describes the interaction between quarks by the exchange of gluons.

Deep inelastic lepton-proton experiments have played an important role in the understanding of the structure of the proton and in establishing QCD as the theory of the strong interaction. Compared to earlier experiments with fixed proton targets the lepton-proton collider HERA with its much larger lepton-proton centre-of-mass energy allows the exploration of proton structure and hence the fundamental constituents of matter at a significantly higher resolution.

The HERA electron[1]-proton collider in Hamburg, Germany was the only electron-proton collider in the world. For over a decade until its decommissioning in late 2007 the experiment H1 and its sister experiment ZEUS were recording and analysing data from HERA and probing the structure of matter down to scales of $\sim 10^{-18}$ m and expanding the existing knowledge of the structure of matter on the smallest accessible scales.

The topic of this thesis is the measurement of cross sections for the production of heavy-flavoured, i.e. charm and beauty flavoured, hadron jets. The dominant production

[1] In this thesis, the term electron is used to refer to both electron (e^-) and positron (e^+).

mechanism of heavy quarks at HERA is photon gluon fusion (PGF) in which a heavy quark-antiquark pair is produced by the interaction between a photon from the incoming electron and a gluon from the incoming proton. This process provides a good testing ground of QCD.

Previous measurements of *charm* and *beauty* at HERA were mostly based on the explicit reconstruction of e.g. a D^* meson [1] in the case of *charm*, while for *beauty* the semi-leptonic decay of a *b* hadron into electrons and mesons was used as a signature. In these measurements the statistical accuracy of the data was limited by the branching fractions and lepton identification requirements. In recent years, at H1 a new approach has been developed which is solely based on hadronic information (i.e. jets) utilising lifetime information. In this approach events containing heavy quarks are distinguished from the light quark events by the long lifetime of *charm* and *beauty* flavoured hadrons, which leads to displacement of the tracks from the primary vertex. This technique which is based on the precise spatial information available from the H1 silicon vertex detector was introduced in the measurements of *charm* and *beauty* structure functions $F_2^{c\bar{c}}$ and $F_2^{b\bar{b}}$ in the deep inelastic scattering regime [67].

This analysis presents the first measurements of the cross sections of *charm* and *beauty* jets in the Deep Inelastic Scattering (DIS) regime using a method based on the impact parameter and reconstruction of the displacement of the tracks from the primary vertex, using precise spatial information from the H1 vertex detector.

The thesis proceeds as follows; chapter 2 presents an overview of the H1 experiment with emphasis placed on the components of the detector that are essential for this analysis. Chapter 3 describes the Standard Model of particle physics, and the phenomenology of heavy quark production at HERA. Chapter 4 is about the event selection, outlining the criteria which have been used to select events containing heavy flavour hadrons. Chapter 5 gives details of the event reconstruction procedures applied to facilitate the extraction of information pertaining to heavy flavoured hadrons from the collisions. Chapter 6 deals with the method used to determine the fraction of events which contain charm and beauty jets. Chapter 7 presents the results: cross sections for *charm* and *beauty* jet production. The thesis concludes with chapter 8, where a summary, outlook and discussion of the results are given.

A Note on Units

Throughout this thesis a system of natural units is used whereby $\hbar = c = 1$

Chapter 2

"Take interest in these sacred dwellings which we call laboratories.
There it is that humanity grows greater, stronger, better".
Louis Pasteur

The H1 Experiment at HERA

2.1 Introduction

This chapter starts with a brief description of HERA accelerator and an overview of the H1 detector with emphasis on the components of the detector that are more relevant to this analysis ,a full description of the detector may be found in [2] .

The H1 detector is located in the North Hall of HERA[2] at DESY[3], in Hamburg, Germany. HERA collides electrons or positrons with protons in order to probe the structure of the proton and is the world's first accelerator to collide different particle species at high energy. HERA consists of two separate concentric storage rings located in a single tunnel of about 6300 m length. A schematic overview of HERA, including the injectors and a chain of pre-accelerators, is shown in figure 2.1

[2] HERA is an acronym for Hadron Elektron Ring Anlage.
[3] DESY stands for Deutsches Elektronen Synchrotron.

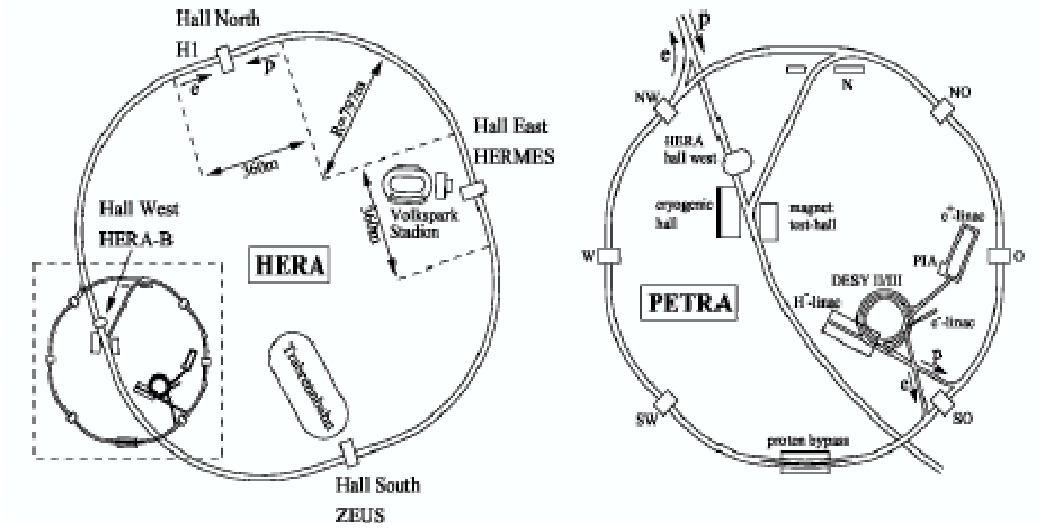

Figure 2.1: The HERA accelerator (left) and its pre-accelerator, PETRA (right).

Four experiments are located around the HERA ring: two multi-purpose detectors, H1 and ZEUS, and two fixed target experiment HERMES and HERA-B. The latter stopped operation in 2003.

2.2 The HERA Accelerator

Construction of the HERA accelerator was completed in 1990 and the HERA experiments began taking data in 1992. HERA accelerates protons to an energy of 920 GeV (820 GeV before 1998) and electrons (or positrons) to an energy of 27.5 GeV and collides the two counter-rotating beams head on at the H1 and ZEUS interaction points. The two fixed target experiments, HERMES and HERA-B, make use of only one of the HERA beams. HERMES studies the collisions of the electron beam with polarised gas targets to investigate the spin structure of the proton and HERA-B investigates the production of b-quarks by bombarding a wire target with the proton beam.

The centre-of-mass energy of the collisions that take place within the colliding beam experiments is 319 GeV (301 GeV before 1998). The RF[4] buckets that transport the electron and proton bunches are 96 ns apart, corresponding to a frequency of 10.4 MHz. Electrons are injected at 12 GeV and are guided round their ring by a warm magnet system, while protons are injected at 40 GeV into a ring with superconducting dipole magnets.

In operation, electron (or positron) and proton beams are stored in the HERA rings in up to 220 bunches, every bunch consisting of approximately 10^{11} particles. The particles within these bunches are spread along the longitudinal direction with an approximately Gaussian distribution of width $\sigma_z \simeq 1$ cm for the electron bunches and $\sigma_z \simeq 10$ cm for the protons. As a direct result of this spread, the electron-proton interaction points are approximately normally distributed around the nominal interaction point with $\sigma_z \simeq 10$ cm. Typically, only 175 of the 220 RF buckets in each beam are filled with particles. Most of these bunches collide with bunches from the opposing beam at the interaction points, but some bunches coincide with empty RF buckets in the opposing beam. These "pilot" bunches are used for the study of beam-related backgrounds(cf. Appendix D, Figure D.2 and Figure D.3), caused, for example, by the collision of beam particles with the residual gas atoms in the beam-pipe (beam-gas interactions) or collisions of stray beam particles with the beam-pipe and adjacent material (beam-wall interactions).

The performance of HERA accelerator, measured in terms of the produced luminosity, improved steadily from its first collisions in 1992 until the end of the HERA-I running period in the year 2000. HERA then underwent a luminosity upgrade, designed to increase the luminosity by a factor of three, and operation restarted in 2002. The planned luminosity increase was rapidly achieved, but severe backgrounds in the H1 and ZEUS detectors plagued initial HERA-II running following the upgrade. These were

[4] In this scheme five PETRA fills are needed to produce a complete HERA luminosity filling. The beams are synchronised in luminosity operation. This is achieved by making the *revolution frequencies* of the protons and of the electrons equal and by phase-locking the two RF frequencies. In this way it is ensured that the collision points are centred in the interaction regions.

investigated and measures introduced to combat them and the operation of HERA and the H1 and ZEUS detectors proceeded smoothly from 2004. The data discussed in this thesis were taken in the years 2006 and 2007 corresponding to an integrated luminosity of 189 pb^{-1}.

2.3 The H1 Detector

H1 detector [2], illustrated in figures (2.2a and 2.2b) is a general purpose detector designed to measure the charge, momentum and direction of the particles emanating from the electron-proton collisions that take place in its centre. Here, a right-handed (RH) Cartesian coordinate system is used to aid the description of the detector and the paths of particles it measures. The origin of this system is at the nominal interaction point, the x direction is towards the centre of the ring, the y direction is vertically upwards and the z, or forward, direction completes the RH system and points along the direction of the proton beam. The corresponding spherical coordinate system is defined such that $\theta = 0°$ is in the proton beam direction and consequently $\theta = 180°$ is in the electron, or backward, direction. The azimuthal angle ϕ is measured with respect to the x axis and the r coordinate gives the distance of points from the z axis.

The H1 detector is asymmetric in the z direction, being bulkier in the forward direction: due to the asymmetry in the energy of the incoming electron and proton beams, the centre-of-mass of the ep collisions is strongly boosted along the proton direction hence most of the high energy particles are detected in the forward region. The backward detectors are dedicated mainly to the identification and measurement of the scattered electron. In total, the H1 detector measures approximately $12_{\text{length}} \times 10_{\text{width}} \times 15_{\text{height}}$ m^3 and weighs about 2 800 metric tonnes.

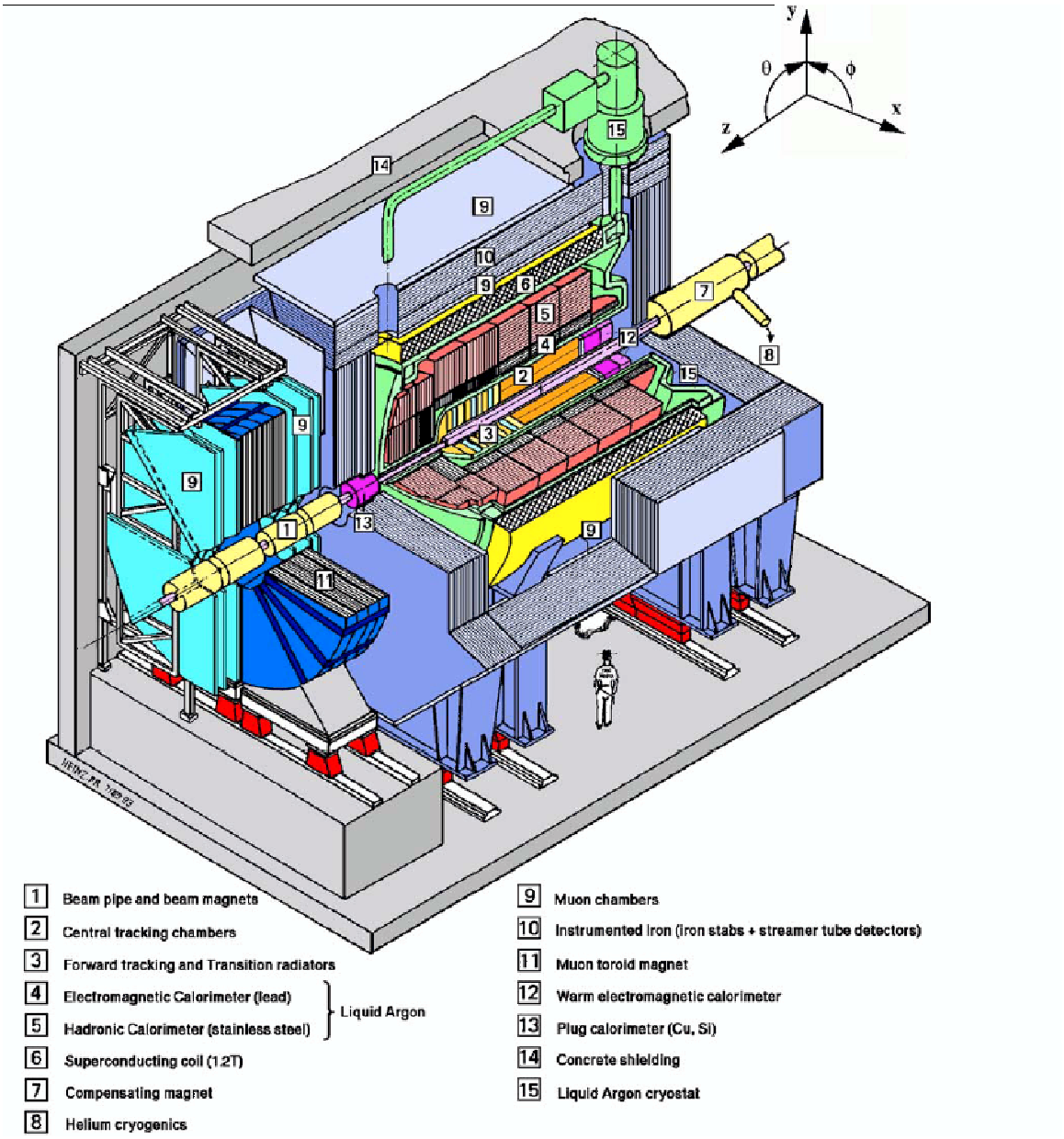

Figure 2.2a: The H1 detector.

Surrounding the beam-pipe in a cylindrical arrangement are the tracking detectors which are subdivided into forward (number 3,fig2.2a), central (number 2,fig 2.2a) and backward (number 12, fig 2.2a) regions. Outside the trackers are the calorimeters. The Liquid Argon Calorimeter (LAr – numbers 4 and 5, fig 2.2a) covers the forward and central regions ($4° \leq \theta \leq 154°$) and the Spaghetti Calorimeter (SpaCal – number 12,fig 2.2a) covers the backward region ($153° \leq \theta \leq 177°$). The LAr calorimeter consists of an electromagnetic section (number 4,fig 2.2a), which is built out of lead plates, and a hadronic section (number 5, fig 2.2a) which is constructed of steel plates. These plates form the passive material of the calorimeters in which the electromagnetic and hadronic showers develop, respectively. Both sets of plates are interspersed with liquid argon which allows the measurement of the charged particles produced in the electromagnetic and hadronic showers. The passive material in the SpaCal is lead, with the readout being performed using scintillating fibres. An additional Plug calorimeter (number 13, fig2.2a) is installed around the beam-pipe in the very forward region in order to increase the detector acceptance for particles produced at very small polar angles. The main body of the H1 detector is encased in layers of instrumented iron (number 10, fig2.2a) which provide the return yoke for the experiment's magnetic field, make possible the measurement of penetrating muon tracks and also provide a crude calorimetric measurement of any energy leaking out of the central calorimeters.

In the negative z-direction the luminosity system is placed close to the beam pipe (number 1, fig 2.2a).

In the forward direction, the Forward Proton Spectrometer (FPS) and Forward Neutron Calorimeter (FNC) are installed to allow studies of interactions containing a leading baryon.

In figure (2.2b) a r-z-section of the H1 tracking chambers and calorimeters is displayed, where a few important detector polar acceptance borders are indicated as lines.

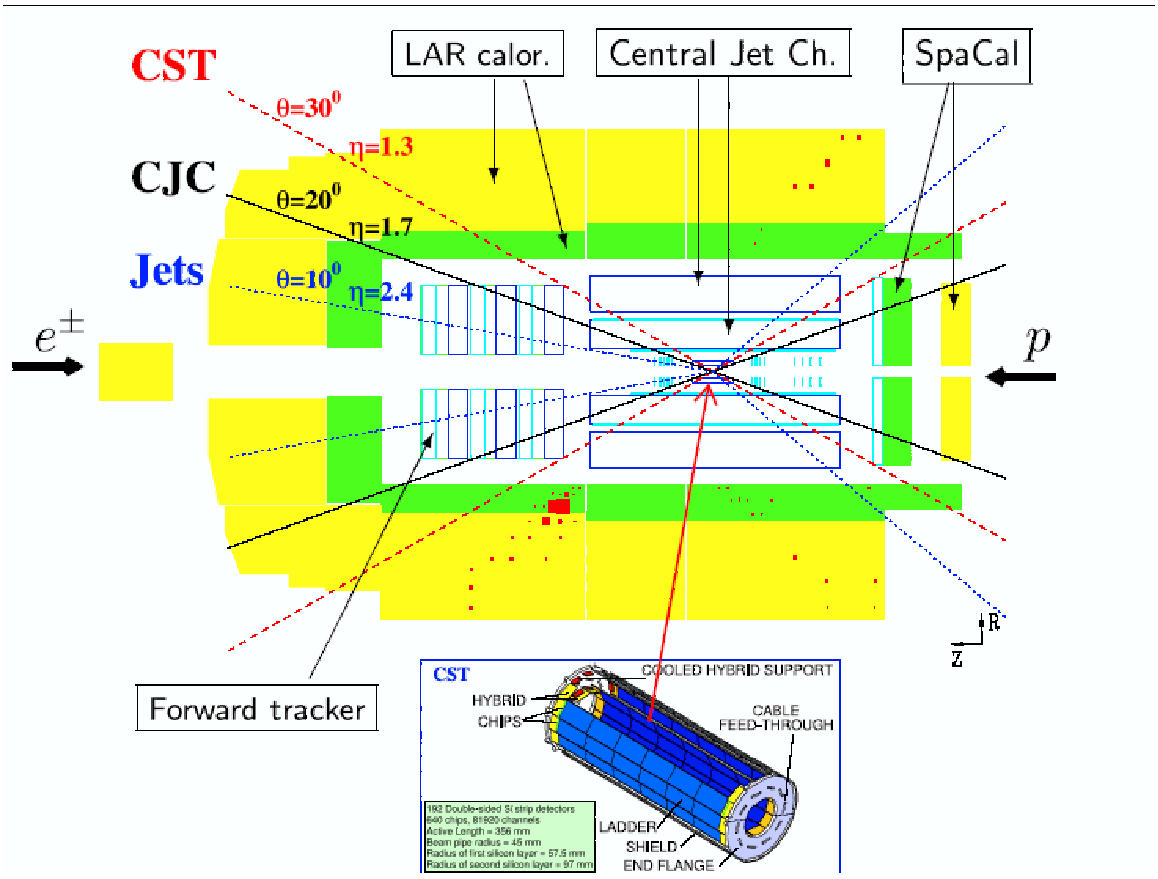

Figure 2.2b: *rz-view of the tracking system and calorimeters of the H1 detector. The layout of the central silicon tracker (CST) is shown separately below in a larger scale. The dashed and full lines indicate the polar angle acceptance borders for tracks measured with high quality in the CST and the central drift chambers (CJC), respectively. The dotted lines indicate the typical minimal and maximal polar angles for selected jets which are reconstructed in the LAr calorimeter*.

The two main methods of particle detection employed by H1 are *tracking* and *calorimetry*. A track is the reconstructed trajectory of a charged particle, from which the particle's momentum can be determined and by using a calorimeter to measure the development of the electromagnetic or hadronic shower initiated by the particle, information about its energy can be obtained. These two detection methods are discussed in more detail in the following.

2.3.1 Gaseous Tracking Detectors

H1 uses two types of detectors for tracking: gaseous detectors such as drift chambers and multi wire proportional chambers, and silicon detectors. The operating principle of the gaseous detectors and the layout of these in H1 are described here and the silicon detectors are discussed in the following section.

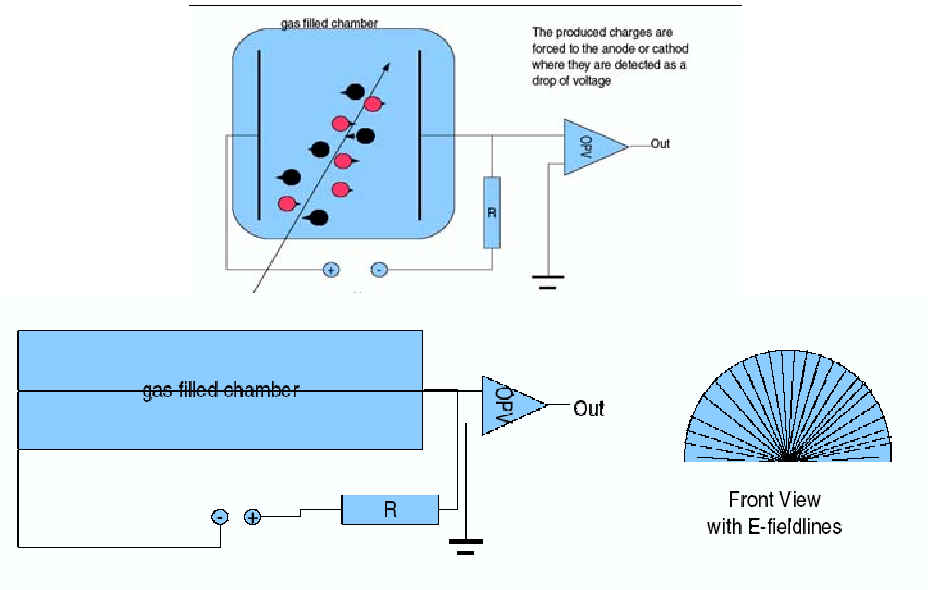

Figure 2.3: Schematic drawing of a single cell of a gaseous tracking detector: the upper picture shows a cross section along the electric field direction in the detector and the lower picture cross sections transverse to the electric field.

The gaseous chambers consist of gas-filled cells across which an electric field is established by anode wires and cathode plates of wires, as is shown schematically in Figure 2.3. A charged particle passing through the chamber causes ionization in the gas. The resulting electrons move at an approximately constant velocity, the drift velocity, toward the anode wires as a result of the constant electric field which permeates the majority of the chamber. When the drifting electrons get close to the anode, they experience an increasing electric field strength. They are accelerated by this field to an extent which causes them to ionize further gas molecules as they collide with these. This gas amplification process leads to an increase in the number of electrons and ions close to the anode and eventually to a measurable electronic pulse on the anode wire. In drift

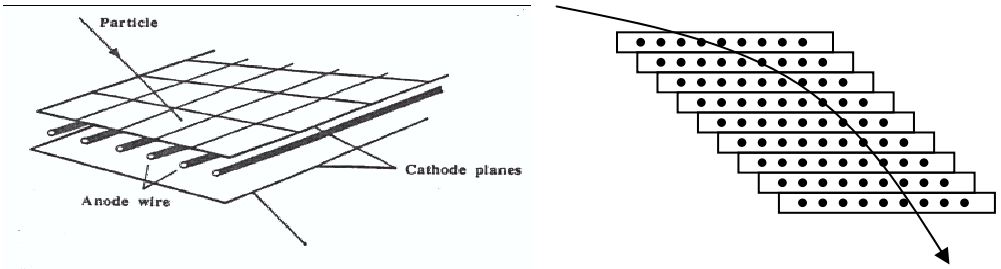

Figure 2.4: Drawings of an MWPC: the sketch on the left depicts a single MWPC, whereas that on the right shows a multi-layered MWPC in which each dot represents a wire, viewed end on. A particle, deflected by a magnetic field, "hits" a series of wires and from these hits the measured trajectory shown as the curved arrow can be reconstructed.

chambers, the time taken for the electrons to drift to the wire and the known drift velocity are used to determine the position at which the original fast particle traversed the chamber. Multi-wire proportional chambers (MWPCs), as illustrated in Figure 2.4, have a much closer anode spacing than drift chambers, so the signal appears very quickly. In the MWPCs of the H1 experiment, the particle's position is deduced purely from that of the anode on which the signal appears. The short time difference between the particle passing through the chamber and the electronic signal makes MWPCs particularly useful for triggering purposes.

The layout of the H1 tracking system is illustrated in Figure 2.5. The various components of this system are discussed below.

2.3.2 Central Track Detector

The Central Track Detector (CTD) consists of six chambers in total which are housed in an aluminium tank. It is the principal tracking device of H1 and provides track reconstruction and triggering in the polar angle range $15° \leq \theta \leq 165°$. The six chambers of the CTD, from the inside out, are: the Central Inner Proportional Chamber (CIP), the Central Inner z Chamber (CIZ), the inner Central Jet Chamber (CJC1), the

Central Outer z Chamber (COZ), the Central Outer Proportional Chamber (COP), and the outer Central Jet Chamber (CJC2).

The main tracking components of the CTD are the two cylindrical concentric drift chambers, CJC1 and CJC2, illustrated in Figure 2.6. CJC1 has 30 cells with 24 sense wires each, whilst CJC2 has 60 cells each containing 32 sense wires. The sense wires run parallel to the beam and allow precise measurement of tracks in the $(r-\phi)$ plane [3]. Each cell is inclined by 30° to the radial direction.

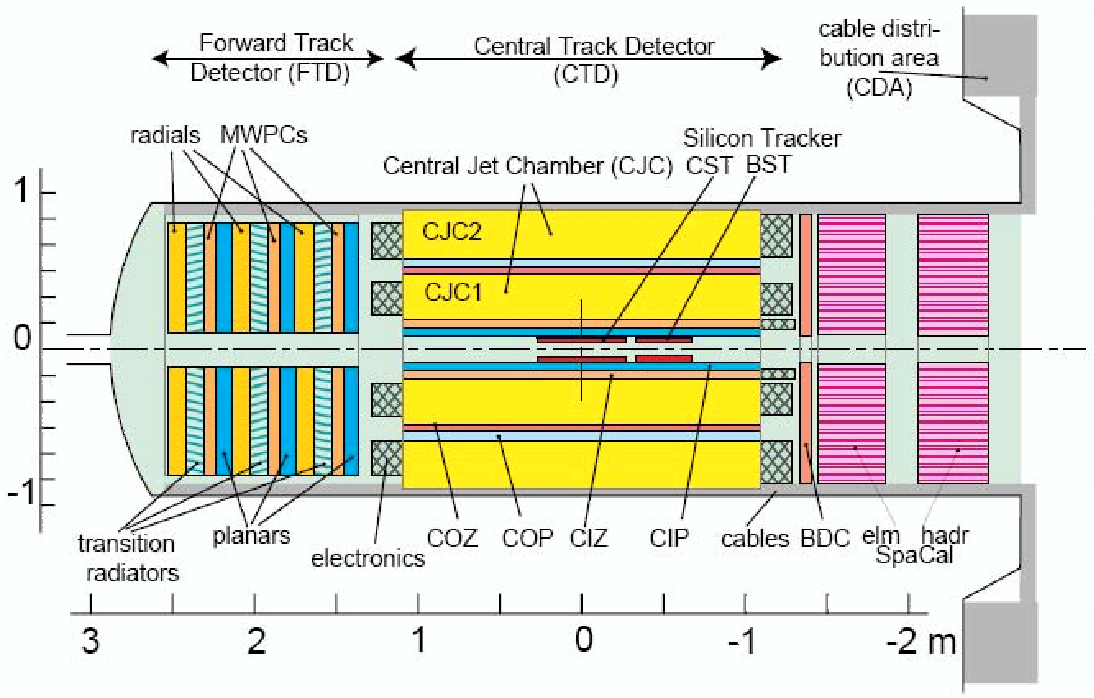

Figure 2.5: A vertical cross section through the H1 tracking system, showing the central, forward, and silicon trackers and the backward drift chamber (BDC).

This value is chosen to ensure that the direction of the electrons drifting towards the anode wires under the influence of the electric field in the CJC and the solenoidal magnetic field is roughly perpendicular to the anode wire plane. This minimises the influence of the drift velocity changes close to the anode wires on the measured hit positions. A further advantage of the tilted cell structures is that each high momentum track then crosses a sense wire plane at least once in CJC1 and CJC2. Ensuring that the tracks match at the crossing point allows the time at which the particle crossed the wire

plane to be determined to an accuracy of approximately 0.5 ns. This allows easy separation of the tracks coming from different bunch crossings and also allows determination of the time, t_0, at which the interactions producing the tracks occurred at the interaction-point (IP). From the drift time, single hits are reconstructed with a spatial resolution of $\sigma_{r-\phi} \approx 170\mu\text{m}$ [2] in the $(r-\phi)$ plane. Along the anode wires, a resolution of $\sigma_z \approx 30\text{mm}$, of the order of 1 % of the wire length, is obtained by charge division, that is comparing the magnitudes of the charge signals measured at each end of the sense wire. Combining the measurements of all anodes wires hit by a track allows the determination of the energy loss of an ionizing particle with a relative uncertainty of about 10% [2].

Track identification, or pattern recognition, in the CJC is based on the precise $(r-\phi)$ information. Triplets of close hits are identified, then linked to form tracks. A helical fit is used to determine the track parameters, for example the curvature from which the transverse momentum is calculated. For tracks that are consistent with having originated from the IP, a constrained fit is used, imposing the condition that the tracks pass through a common interaction vertex. This results in improved precision. Tracks which do not pass through the IP are assigned either to secondary vertices (restricted to decays of neutral particles into pairs of oppositely charged particles) or to non-vertex fitted tracks. These latter may result from cosmic muons sources (cf. Appendix D) or other sources of background, for example. The *z* information of the tracks is greatly improved by the procedure of fitting all tracks to a common vertex and the resulting precision of the vertex determination in the *z* plane is around 1 cm. The *z* resolution is improved by two orders of magnitude by including hits from the CIZ and the COZ [4] in the track reconstruction, as their signal wires are perpendicular to the *z*-axis.

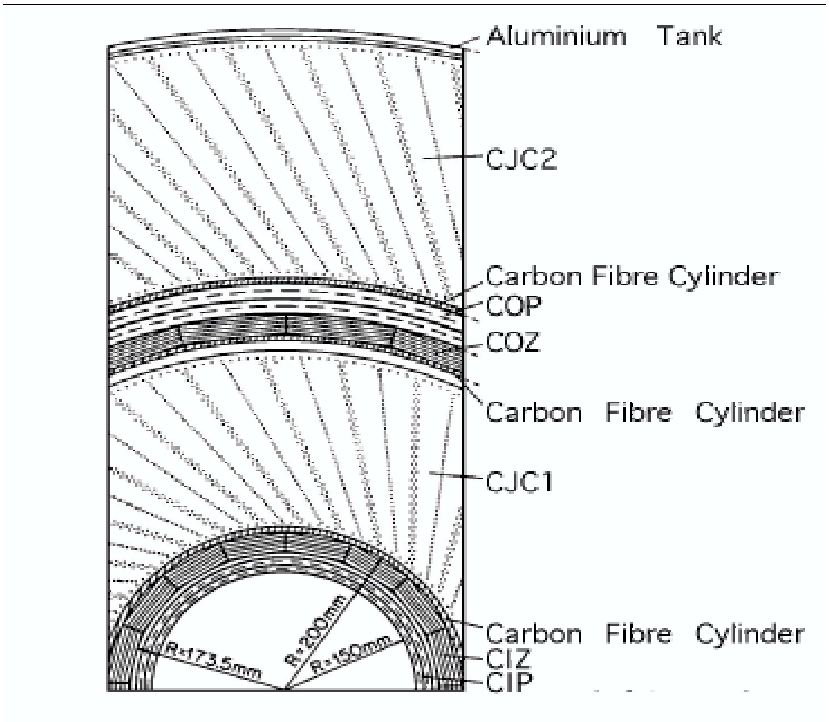

Figure 2.6: Radial view of the CTD, showing the cells of the CJC1 and CJC2.

The CTD contains two MWPCs for triggering on tracks pointing to the nominal vertex region in the z plane. These are the CIP and COP chambers, respectively [5]. They have little impact on the final track measurement, but provide fast space-point information with a timing resolution of better than 96 ns. The information from the CIP and COP chambers is combined with that from MWPCs in the forward tracker to produce the z-vertex trigger: demanding a vertex within the interaction region along the *z*-axis allows the rejection of backgrounds due to cosmic rays and beam gas interactions, for example.

2.3.3 Central Silicon Tracker

The innermost tracking detector at H1 is the Central Silicon Tracker (CST). It consists of two cylindrical layers of double sided silicon strip sensors arranged concentrically around the beam axis at radii of 5.7 cm and 9.7 cm. Figure 2.7 shows a schematic $r\phi$ view of the CST . The active length of the CST is 35.6 cm, so it covers the polar angle range $30° < \theta < 150°$. The inner CST layer contains 12 and the outer CST 20 identical

and slightly overlapping ladders, each composed of two half ladders of 22.1 cm length and 3.4 cm width. Each half ladder, as is illustrated in Figure 2.8(a), consists of three silicon sensors and a hybrid structure carrying the readout electronics.

On the outer face (p-side) of each sensor, there are 1280 p^+ strip implants running parallel to the *z*-axis with a pitch of 25 μm. Every second strip is read out, leading to a single hit resolution in the rϕ projection of 12 μm [6]. The opposite side (n-side) is used to determine the *z*-position of the incident particles. Here the n^+ strip implants of 88 μm pitch are oriented perpendicular to the z-axis. Every n-side strip is read out via an additional metal layer. The intrinsic hit resolution in *z* is significantly worse than the rϕ resolution due to the larger pitch. The *z* resolution depends on the incident angle of a track and has a minimum of 22 μm for $\theta \sim 90°$ [7].

Signals from neighbouring strip on both the p- and n-sides are combined into clusters by a hit-finding algorithm. The association of p- and n-side clusters to hits results in three-dimensional space points which are then attached to tracks identified in the CJC, allowing more precise determination of the trajectories of these tracks close to the IP [7].

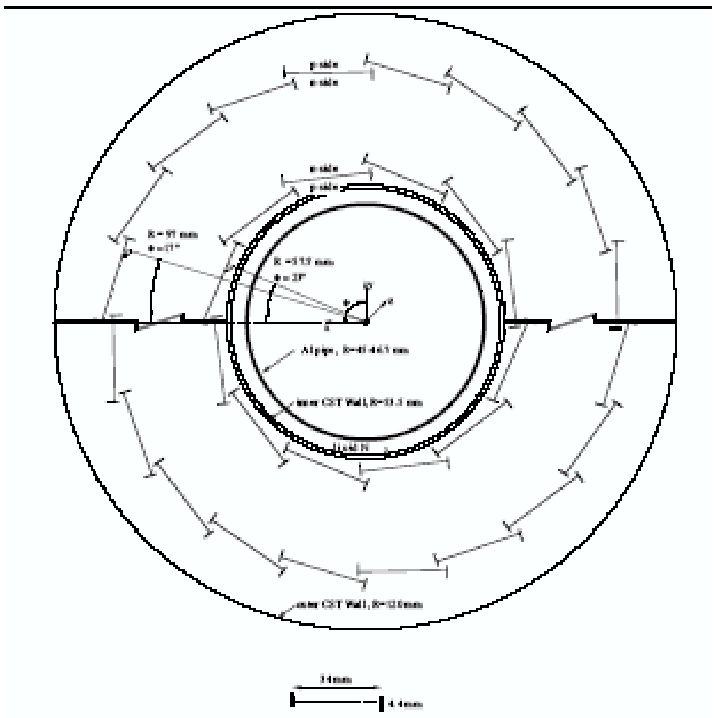

Figure 2.7: A radial view of the CST.

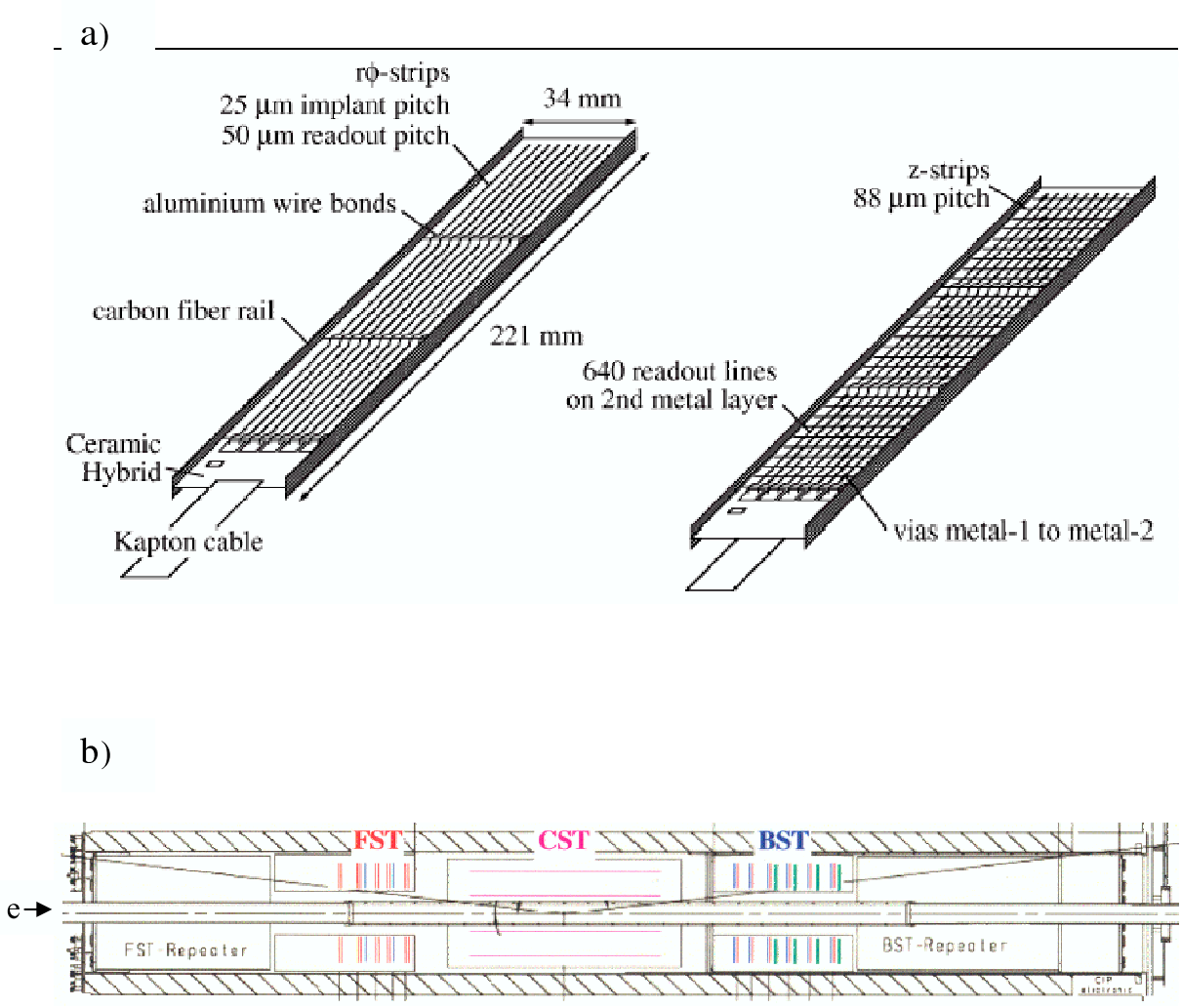

Figure 2.8: a) Two views of the half ladders from which the CST is constructed: left p side; right n side. b) Side view of the interaction region of the H1 detector. The three silicon strip detectors FST, CST and BST are indicated.

The upgrade for HERA II is consisted of the new H1 Forward Silicon Tracker (FST) which extends the central silicon tracker (CST), into the forward direction (see figure 2.8b). The FST consists of five layers of two silicon strip planes and it covers a range of polar angles between 8° and 16°. The additional angular acceptance of the FST leads to an increase of the reach for charm physics in Bjorken-*x*. In 2004 data, the FST was

shown to have a signal hit efficiency of close to 100% and a track efficiency of larger than 95% [82].

2.3.4 Hit Finding

The hit finding algorithm is described in [7]. Charged particles crossing the CST produce pairs of positive and negative charge carriers leading to signals which are read out by the silicon strips. In a first step neighbouring strips with a signal above noise threshold define a *cluster*. The center-of-gravity of the cluster then determines the hit position. This is done independently for the *p*- and *n*-side. In a second step the association of *p*- and *n*-side clusters results in three dimensional *space points*.
The total signal-to-noise ratio of a cluster must exceed five (four) on the *p*-side (*n*-side). On the *n*-side an additional metal layer is needed for the readout which deteriorates the signal-to-noise ratio by a factor of two compared to the *p*-side.

2.3.5 The Forward Tracker

The Forward Tracker Detector (FTD) is shown in Figure 2.2a (number 3). It consists of three supermodules arranged along the z-axis. Prior to the year 2000, each supermodule consisted of three planar drift chambers, a MWPC, a transition radiator and a radial drift chamber, in increasing *z*. The FTD covers the polar angle range $5° < \theta < 25°$ [2].

2.3.6 Backward Drift Chamber

The Backward Drift Chamber (BDC), the position of which is shown in Figure 2.5, is designed to provide an accurate measurement of the angle of the scattered electron in DIS processes with $Q^2 < 100$ GeV^2. It is mounted in front of the SpaCal calorimeter, which is described below, and has a similar angular acceptance: $153° < \theta < 177.5°$ [8].

2.4 Calorimetry

Calorimeters provide information on the energy of the particles which enter them. The incident particles are stopped in the calorimeter volume by interactions with the atoms of the calorimeter material, in which they lose energy and produce daughter particles. The number of these daughter particles is proportional to the energy of the incoming particle, so detecting and counting them allows the energy of the incident particle to be determined. The nature of the interactions that produce the daughter particles depends on the type of the incoming particle. Hadrons undergo primarily strong interactions with the nuclei of the atoms, while electrons and photons interact electromagnetically in the electric field of the nucleus.

When an electron or a photon traverses the absorber, it rapidly loses energy through a combination of bremsstrahlung ($e \rightarrow e\gamma$) and pair production ($\gamma \rightarrow e^+e^-$). The characteristic length scale for these processes is the radiation length, X_0, which is the mean distance over which $1/e$ of the incident particle's initial energy is lost. For lead, $X_0 = 0.56$ cm.

Strongly interacting particles (i.e. hadrons), undergo both elastic and inelastic scattering with the nuclei of the absorber material. Consequently, a shower of secondary (daughter) particles develops, which propagate through the material interacting further until the energy of the particles are sufficiently low that progression can be brought to a halt by either ionisation or nuclear capture. The characteristic length scale for this process is the interaction length, λ, which is much larger than X_0, e.g. $\lambda = 17$ cm for lead. In order to ensure that all the energy of an incident particle is absorbed, hadronic calorimeters are therefore considerably larger than electromagnetic ones.

The different shower development mechanisms for electromagnetic and hadronic particles usually result in different numbers of daughter particles being produced for a given incident energy. Typically, the response to hadronic particles is around 30% lower than that of electrons or photons. The calorimeter is then said to be *non-compensating*.

In addition, a hadronic shower typically contains both hadronic and electromagnetic components, because any neutral pions produced in the shower decay into photons and initiate an electromagnetic shower. Therefore a correction for this effect has to be applied in the reconstruction of hadronic energy.

2.4.1 The H1 calorimeters

The H1 calorimeters are constructed of alternating *passive* and *active* layers. The interactions described above take place largely in the passive layers, and the resulting daughter particles are detected in the active layers. Figure 2.9 shows the layout of the H1 calorimeters.

In the electromagnetic section of the LAr calorimeter (EMC), the passive or absorber material is lead, while the active material is LAr. The charged daughter particles traversing the LAr ionise the argon atoms. The resulting ions drift to electrodes in an applied electric field resulting in a measurable electronic signal which is proportional to the number of daughter particles and hence to the energy of the incident particle. In the hadronic section of the LAr (HAC), the active material is again LAr, but the absorber is stainless steel. In the electromagnetic SpaCAL, the absorber is lead and the active material scintillating fibres which are embedded in the lead. The signal here is the scintillation light produced by the daughter particles in the fibres. The same materials are used in the hadronic SPaCAL, which sits behind the electromagnetic SpaCAL. The instrumented iron consists of iron layers interspersed with streamer tubes and the Plug is a copper/silicon calorimeter.

The combined coverage offered by the LAr and SPaCal amounts to a laboratory pseudo-rapidity range of $-3.8 < \eta < 3.6$. The Plug calorimeter extends the acceptance in the forward region and the instrumented iron or the tail catcher measures energy leakage from the main calorimeters.

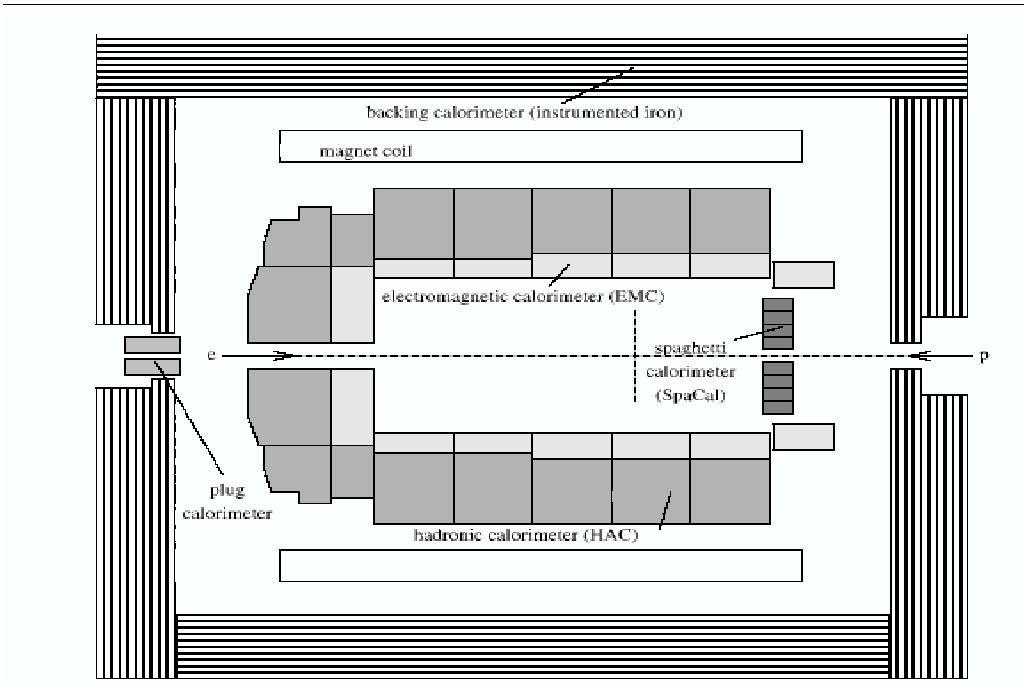

Figure 2.9: The layout of the H1 calorimeters shown in the r-z plane: the LAr calorimeter consists of an electromagnetic (EMC) and hadronic (HAC) part; to the rear of the detector is the SpaCal, which also has electromagnetic and hadronic sections; surrounding the entire detector is the tail catcher or backing calorimeter which also serves as a muon detector.

2.4.2 Liquid Argon Calorimeter

The Liquid Argon calorimeter [9] is used for the measurement of scattered electrons in high Q^2 events (i.e. $Q^2 > 100$ GeV^2) and is the main detector for the reconstruction of energies in the hadronic final state. The LAr provides a polar angle coverage of $4° < \theta < 154°$, corresponding to a laboratory pseudo-rapidity range of $-1.43 < \eta < 3.35$.

As is shown in Figure 2.10, the EMC and HAD section of the LAr both use a single liquid argon cryostat. The LAr is located within the solenoid to reduce the amount of dead material encountered by particles before they reach the calorimeter. The LAr is subdivided into eight wheels, the Backward Barrel (BBE), three Central Barrels (CB1, CB2 and CB3), two forward Barrels (FB1 and FB2) and the Inner and Outer Forward

(IF and OF) wheels. Each of the wheels is divided into eight φ octants. The BBE is purely electromagnetic, all the other wheels have both hadronic and electromagnetic sections. Furthermore, due to the asymmetric beam energies, both the EMC and HAC sections are deeper in the forward region, where the energy of the incident particles is generally higher.

The electromagnetic (EMC) part of the LAr is constructed from 2.4 mm thick lead plates as absorber, interspersed by gaps of width 2.35 mm filled with liquid argon as sampling medium. The hadronic section (HAC) of LAr is constructed from 16 mm thick stainless steel plates which functions as absorber layer, with alternating layers of liquid argon filled gaps of twice 2.4 mm width. The total depth of the absorber material varies between 20...30 X_o in the electromagnetic section and 4.5...8 λ for the combined electromagnetic and hadronic sections. The LAr consists of 45 000 individual readout channels, which provide a fine granularity that is almost uniform in η and φ. Analysing the measured shower shapes with the resolution provided at this granularity provides electron-pion discrimination down to 1 part per 1000. The LAr is a non-compensating calorimeter. However, the fine granularity of the readout allows the electromagnetic components of hadronic showers to be identified and weighting factors to be applied to achieve compensation.

The energy resolution of the LAr calorimeter, as obtained in test beam measurements, is

$\frac{\sigma_E^{em}}{E} = \frac{0.15}{\sqrt{E(GeV)}}$ for electrons detected in the EMC and $\frac{\sigma_E^{had}}{E} = \frac{0.50}{\sqrt{E(GeV)}}$ for charged pions detected in the EMC and HAC [9].

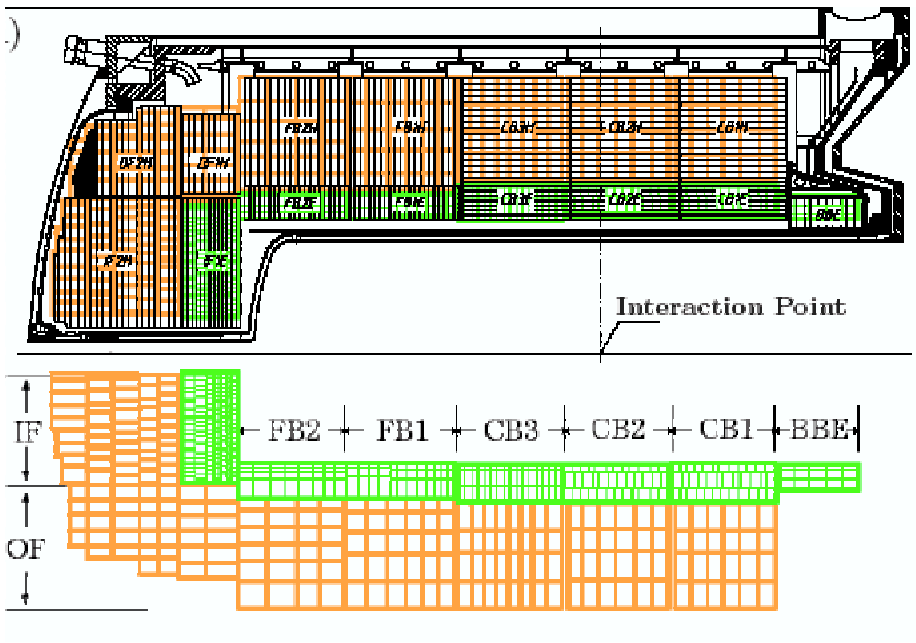

Figure 2.10: Side view of LAr in the r-φ plane, showing (in the upper half) the orientation of the absorber layers and (in the lower half) the segmentation of the read-out cells.

2.4.3 The Spaghetti Calorimeter

The "Spaghetti" Calorimeter (SpaCal) [10] takes its name from the long thin scintillating fibres that are used in its construction. The SpaCal is situated in the backward region of H1 and is illustrated in Figure 2.11.

The SpaCal covers the angular range $153^\circ \leq \theta \leq 177.5^\circ$, which corresponds approximately to Q^2 values in the range $1 \leq Q^2 \leq 100$ GeV^2. It provides efficient electron identification in this region (the probability of misidentifying an electron as a pion is less than 1 in 100 at energies of 5 GeV and is much smaller than this at higher energies) and good measurement of both the electron energy and the angle through which it is scattered, the latter requiring information on the primary vertex position. The SpaCal also provides some information on the hadronic energy in the backward direction.

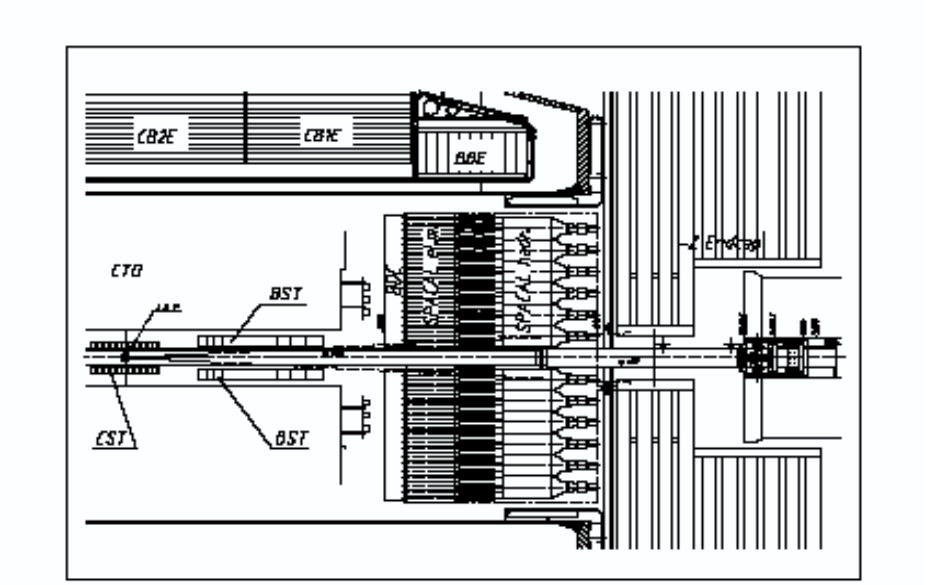

Figure 2.11: Cross section of the backward region of the H1 Detector showing the electromagnetic and hadronic sections of the SpaCal.

A further feature is the precise time-of-flight information it provides, which makes possible rejection of background from some sources, such as proton beam-gas and proton beam-wall interactions occurring to the rear of the H1 detector. The Q^2 region covered by the SpaCal implies that it is also the detector in which the electron is identified and measured in studies of DIS interactions at the lowest Bjorken-x ($x \leq 10^{-4}$).

The SpaCal is a non-compensating calorimeter and, like the LAr, consists of an electromagnetic and a hadronic section. Both sections are constructed of long thin scintillating fibres, aligned parallel to the beam direction and embedded in a lead matrix. The incident particles shower in the lead and the charged particles produced in these showers cause the fibres to scintillate. The light is collected at one end of the fibres by photomultiplier tubes. The system has a time resolution of better than 1 ns. Due to this fast response, the SpaCal is used to provide time-of-flight information and is used for trigger purposes.

The electromagnetic section of the SpaCal consists of 1992 cells which contain fibres of length 250 mm and diameter 0.5 mm embedded in lead blocks. The lead to fibre ratio is 2.3:1. The depth of the electromagnetic section of the SpaCal corresponds to 28 X_0. The

energy resolution of the EM section of the SpaCal the is $0.07/\sqrt{E(GeV)}$, determined in test beam measurements [10].

The hadronic section of the SpaCal consists of 136 cells with fibres of length 246 mm and diameter 1.0 mm in a lead matrix. The lead to fibre ratio for the hadronic part of the SpaCal is 3.4:1 and its depth corresponds to 1 λ. The total depth of the SpaCal thus corresponds to 2 λ. The hadronic energy resolution of the combined HAC and EM SpaCal is $0.5/\sqrt{E(GeV)}$. The acceptance of the hadronic SpaCal is increased to $\theta < 178.7^\circ$ by a backward plug section (consisting of 12 cells) located immediately around the beam-pipe.

2.5 The Luminosity System

A precise determination of the electron-proton luminosity is crucial for the accurate measurement of cross sections at H1. The luminosity measurement is based on the detection of the photon produced in the Bethe-Heitler process ($ep \rightarrow ep\gamma$) [11]. This process has a large cross section and is theoretically well understood. The main background is bremsstrahlung from the electron in the electromagnetic fields of any residual gas molecules in the beam-pipe. The rate of this background is about 10% of the rate for the Bethe-Heitler process. This background can be subtracted using information from the electron pilot bunches. The pilot bunches have no partner proton bunches with which to collide, so electrons in these bunches interact only with the residual gas. The luminosity is calculated as: $L = [R_{tot} - (I_{tot}/I_0) \times R_0]/\sigma_{vis}$, where R_{tot} is the total rate of the events registered in the luminosity detector, I_{tot} and I_0 are the currents in the colliding and pilot bunches, R_0 is the rate caused by the pilot bunches and σ_{vis} is the visible part of the Bethe-Heitler cross section, corrected for trigger efficiency and the acceptance of the luminosity detector. The precision of the luminosity measurement was 1.5% in the years when the data for this analysis were taken.

The luminosity system is situated in the accelerator tunnel in the backward or electron direction. In addition to providing luminosity measurement, the system detects and triggers on scattered electrons at very low Q^2 ($Q^2 < 1$ GeV^2), which corresponds to very

small scattering angles. The photons in these interactions are essentially real, so they can be considered to be photoproduction.

An overview of the luminosity system is shown in Figure 2.12.

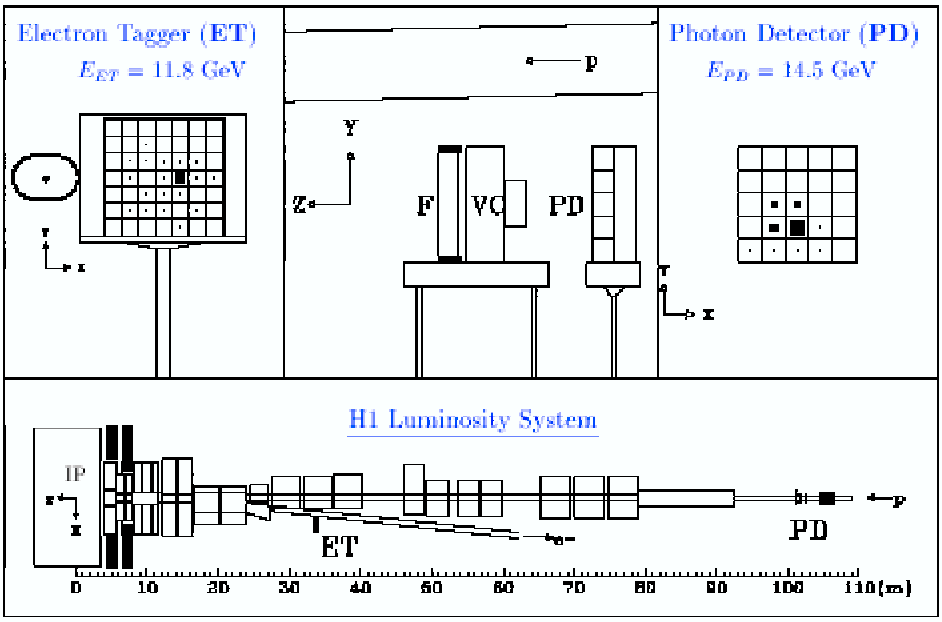

Figure 2.12: The H1 Luminosity System

The two main components of the luminosity system are the Electron Tagger (ET), which is located adjacent to the electron beam-pipe at z = −33.4 m and the Photon Detector (PD) which is adjacent to the proton beam-pipe at z = −102.9 m. Both the ET and the PD are Čerenkov crystal calorimeters a detailed description of these can be found in [2], [11].

After the upgrade of the detector the instantanenous luminosity was increased for HERA II by a factor of ~3. This factor of three increase in luminosity was achieved by installing new focusing magnets near the interaction points. Thus the new accumulated statistic from HERA II data taking period is approximately a factor of five higher compared to HERA I.

2.6 Trigger System and Data Acquisition

This section is divided into two subsections; first a general overview of the *H1 Trigger System and Data Acquisition* is presented and later on at the end of this section *Triggers of Special Interest* to this analysis are discussed.

The beam collision rate at HERA is 10.4 MHz. The rate of electron-proton collisions at low Q^2 is of the order of 10 Hz, whereas the combined rate of background processes[5] is about three orders of magnitude higher than the electron-proton event rate.

In order to sieve the true electron-proton events from the background, to account for the limited bandwidth for the data logging (data transfer to mass storage devices) and to avoid a high experimental dead-time (which occurs during the time the data are read out and new events cannot be recorded) a set of triggers are used, which function as a fast selector of interesting events.

The H1 trigger, shown schematically in Figure 2.13, consists of a pipelined four level system. The levels 1 (L1 for short) to 4 (L4) are designed to progressively reduce the event rate from a maximum of the beam collision rate of 10.4 MHz (the bunch crossing frequency at its input) to about 10 Hz, the rate at which data can be recorded.

L1 and L2 are online hardware triggers, while L4 is an online software trigger. Off line event classification is performed by L5.

[5] The background processes are; mainly beam-gas and beam-wall interactions (i.e. collision of the beam particles with residual gas atoms and collision of the particles with the beam pipe respectively) and background due to halo muons (generated by proton losses around the ring which interact producing pions which subsequently decay) and muons originated from cosmic rays (cf. Appendix D) .

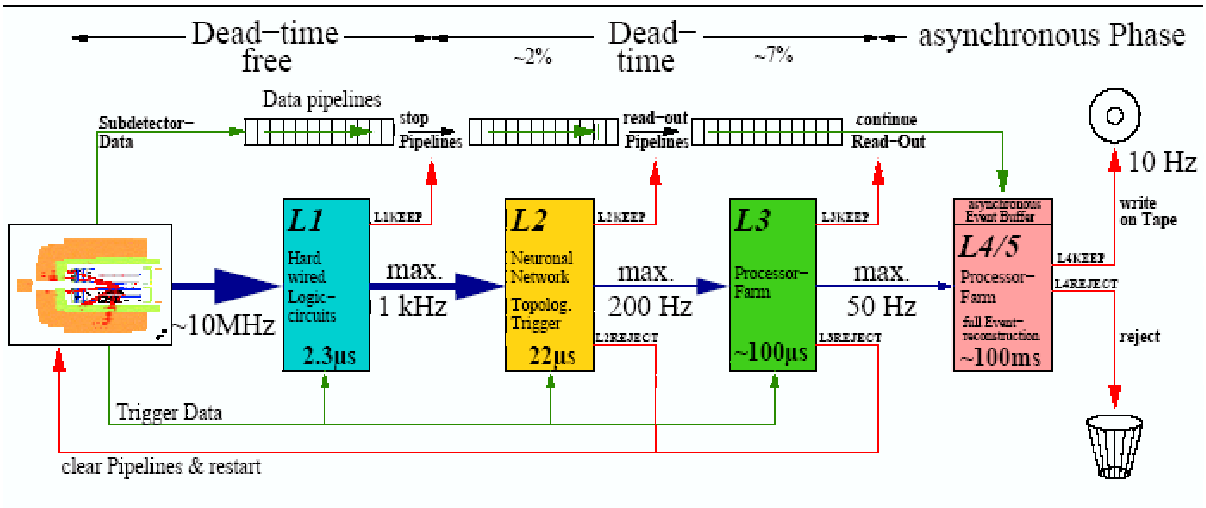

Figure 2.13: An overview of the event rates in the H1 Trigger System.

Level 1: The level one (L1) central trigger currently consists of 207 trigger elements (TE) from different detector subsystems. The trigger subsystems typically each provide 8 different trigger elements which are sent to the Central Trigger. The decision whether to accept or reject an event is made within 2.3 µs, the time taken for approximately 24 bunch crossings. Therefore, in order to avoid losing the subsequent information from other bunch crossings, the information is kept in a pipeline, ensuring new data is constantly taken. This process of pipelining the information and storing new events leads to no deadtime on L1.

The trigger elements from the different subsystems are combined by the Central Trigger logic [12] into 128 logical conditions, which referred to as L1 subtriggers s0…s127. If the conditions for one of these subtriggers are fulfilled, then the event is passed along the pipeline to be processed further and the decision to keep the event at this level is known as L1-Keep. If a subtrigger has a high rate, it can be scaled down (manually and/or automatically) by a factor of N, the prescale factor. This means that only every N^{th} positive decision of this subtrigger is taken into account, effectively reducing the integrated luminosity seen by this subtrigger by $1/N$. A pictorial view of the logic of the L1 and L4 systems is shown in Figure 2.14.

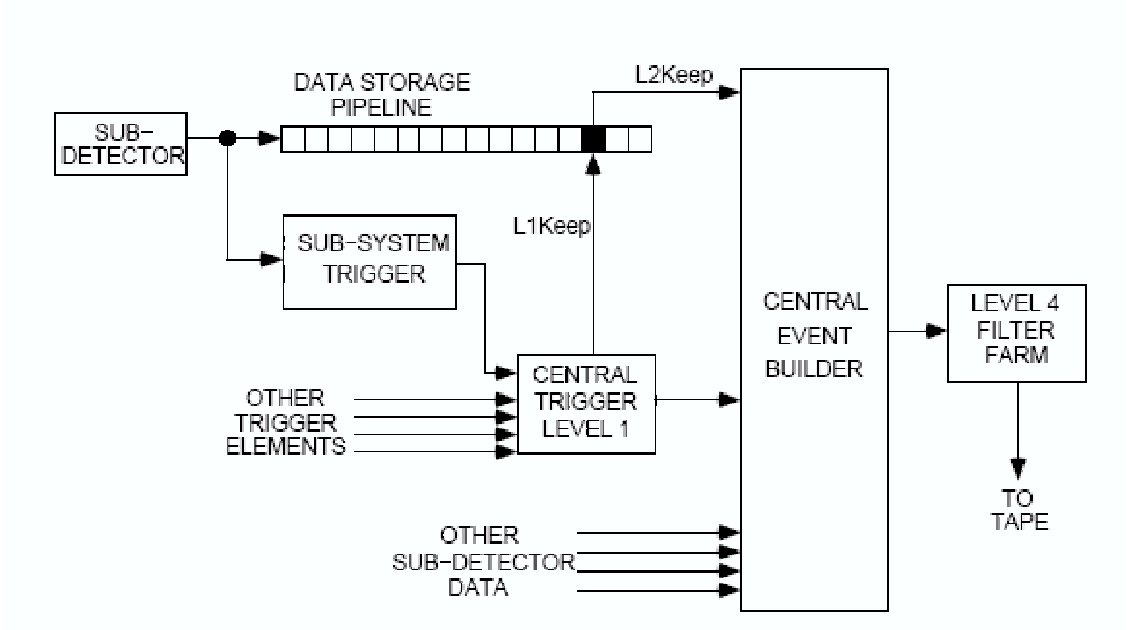

Figure 2.14: A schematic overview of the L1 and L4 trigger systems.

Level 2: The L2 trigger comprises a topological trigger (L2TT) [13] and a neural network trigger (L2NN) [14]. The time required to reach a decision at Level 2 is 20 μs. The L2TT decision is based upon the topological features of an event whereas L2NN facilitates the separation of distinctive physics channels from the background.
Level 2 sends a L2-Keep signal if it determines the event is of interest and causes the entire event to be read out to the Central Event Builder (CEB) and subsequently to L4. On average this process causes a deadtime of about 10%. At this stage, the event rate is reduced to approximately 50Hz (the input rate for L4).

Level 3: This level was not implemented during the HERA-I running period. It is a software trigger that includes a Fast Track Trigger (FTT) [83] and jet trigger. The FTT was commissioned as part of the H1 upgrade programme, FTT performs a fast reconstruction of CJC tracks. The FTT provides some trigger elements for L1 and L2 and designed to perform particle identification at L3. These upgrades are further discussed at the end of this section.

Level 4: The level four trigger performs a complete reconstruction and classification of the event. It is an asynchronous trigger, implemented as software algorithms running on a farm of about 30 personal computers. The L4 farm can process events at a rate of 50 Hz. Once the information has reached this level, most of the unwanted background is removed and, if accepted by L4, the raw data of an event is written to a Production Output Tape (POT) tape. This happens at an event rate of about 10Hz, with a typical decision time of 100 ms for the whole process. Data that are written to the tape at this level consist of the complete raw event information, about 100 kilo-bytes of data per event.

The information on the POT is then passed to a further dedicated computer farm, Level 5 (L5), which is an offline system. The reconstructed event information from this level, about 10 kilo-bytes per event, is permanently stored on a Data Summary Tape (DST).

After the detector upgrade, the trigger electronics described above were improved. The aim of the upgrade was to be able to improve the signal to background ratio and to collect useful physics events while suppressing the triggering of events that are not of interest or are beam-related background. The H1 Fast Track Trigger (FTT) [83] implements charged track finder and mass reconstruction algorithms in the first three levels of the H1 trigger scheme. For the charged particle track reconstruction at the first trigger level L1 ($2.3\mu m$) and second trigger level L2 ($23\mu m$), the FTT makes use of Field Programmable Gate Array (FPGA) and their embedded Count Addressable Memories (CAM). The track parameters are determined by comparing hit-patterns with predefined masks implemented in digital signal processor (DSP). The FTT can reconstruct up to 48 tracks which is sufficient for about 98% of the events of interest.

The FTT functionality is based on hit information in the central jet chambers CJC. In Figure 2.15 the geometrical cell structure of the both chambers is sketched.

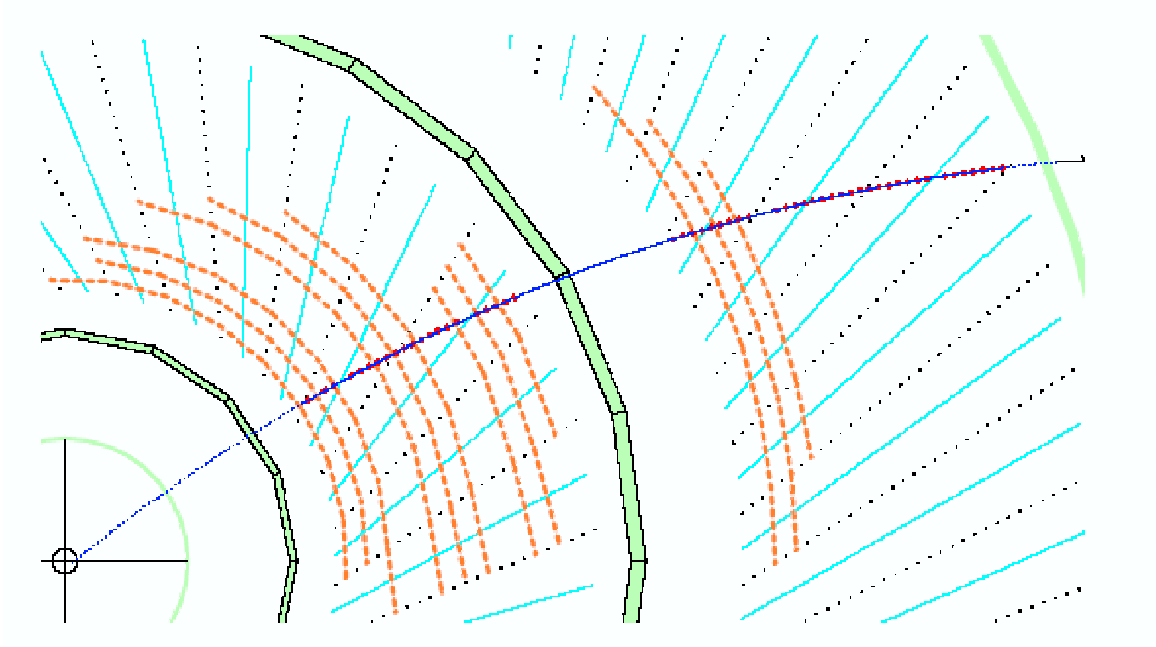

Figure 2.15: The $r\phi$ view of a charged particle track from the interaction point traversing the central drift chambers of the H1 detector. The sense and cathode wires of the chambers are indicated.

In the first step track segments are formed separately in four groups of three layers of wires each. A fast track segment linking, based on matches of track segments in $\kappa(\propto {}^{1}/_{P_T})$ and ϕ is completed within 2 μs to provide level 1 trigger decisions based on charged track multiplicities and charged particle topologies for coarse P_T cuts. The result is used by the second level FTT where the track segments are linked and re-fitted to better precision within 20 μs including the determination of event quantities like a refined track multiplicity, momentum sums and invariant masses for low multiplicity events.

The track parameters of the fitted tracks are sent to FTT level 3 where a farm of commercial processors boards is used to perform a full search for particle resonances within 100 μs. The L3 track information is either used directly or in combination with information from other trigger subsystems to generate a final L3 decision.

In addition to upgrading the drift chamber triggers, the H1 experiment has improved the robustness against severe background conditions by replacing its double layer central

inner multi-wire proportional chamber by a chamber with five layers of pads with geometry projective to the z-position of the ep interaction. The new upgraded detector has ten times more channels and, like the old proportional chamber, provides trigger decisions, based on a z-vertex histogramming technique, at level 1, within a latency of 2.3 μs.

Triggers of Special Interest

In this section, general overviews of the subsystems which produce the trigger elements used in this analysis are given.

2.6.1 The SpaCal Trigger

Two main functions are performed by the SpaCal trigger system: providing a trigger for electron candidates from DIS events, and vetoing events originating from beam-induced background. The trigger system consists of an Inclusive Electron Trigger (IET) for the electromagnetic section, ToF (Time of Flight) vetos for background rejection and total energy sums for both the electromagnetic and hadronic sections of the calorimeter.

The difference in the path length of particles originated from the interaction region and those that are originated from the background (beam-gas, and beam-wall) are exploited by the time-of-flight system in the SpaCal. The path length to SpaCal is shorter for the particles originated from proton beam related to the background than for particles from the ep interactions, such that two distinct peaks are visible in the time distribution of the ToF system. Figure 2.16 shows a typical time distribution as measured by the ToF system of the SpaCal. The separation of the two peaks is around 10 ns, which correspond to the time taken for the particles to travel the 1.5 m from the SpaCal to the interaction point and back again. The position of the interaction window is typically $\pm$ 5 ns around the central timing value of 15 ns for ep interactions.

The Inclusive Electron Trigger of the electromagnetic SpaCal is segmented into 320 arrays of 4×4 neighbouring SpaCal cells (IET windows). The IET windows overlap in

order to avoid efficiency gaps at the borders of the windows. In each window, an analogue sum of in-time energies of the 16 cells is formed [16]. Each sum is compared to three programmable thresholds adjustable in the range 100 MeV to 20 GeV.

These provide three trigger elements $SpaCal_{IET} > 0$, $SpaCal_{IET} > 1$, and $SpaCal_{IET} > 2$. Typical thresholds are 0.5, 2 and 6 GeV, respectively. Additionally, each IET threshold can be further divided into 2 regions; the inner and outer regions. The inner region is contained in a 24 cm by 24 cm box close to the beam-pipe in the approximate range $-17 < x < -9$ cm and $-9 < y < 17$ cm. The outer region encompasses the remainder of SpaCal. The two regions are distinguished from each other because the inner region of the SpaCal suffers from a large counting rate. This "hot spot" spot, is probably due to off-momentum electrons which are bent into the calorimeter by the beam magnets.

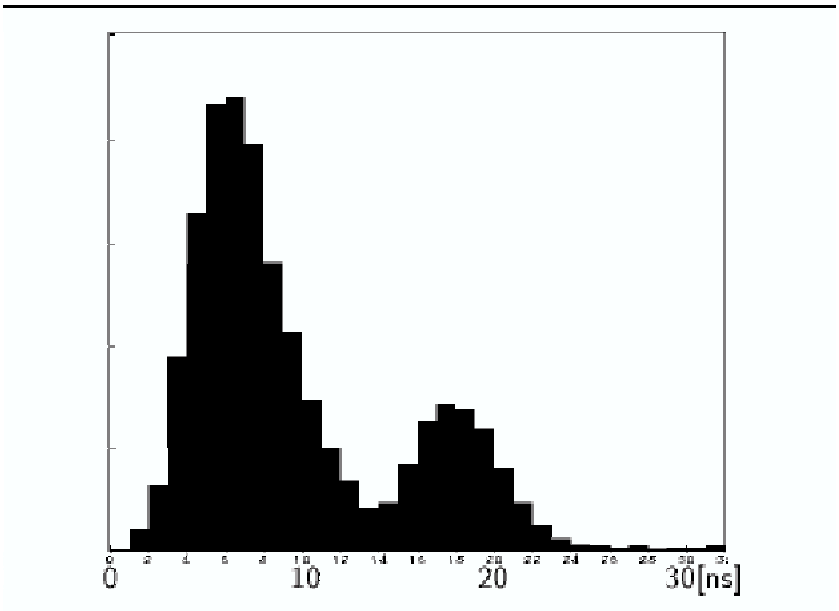

Figure 2.16: Typical time distribution of signals in the SpaCal as shown by the online histogram system. The left peak corresponds to proton beam related background, while the right peak shows the position in time of ep interactions.

2.7 The Detector Simulation

The sample of events generated for *uds* (*up*, *down* and *strange* quarks respectively), *c* (*charm* quark), and *b* (*beauty* quark) production are passed through a detailed simulation of the detector response using the H1SIM package, which models the H1 detector using GEANT3 [17] program, and through the reconstruction software as is used for the data.

Figure 2.17 shows an example of low Q^2 DIS event in the H1 detector with deposit of energy in the SpaCal (from the detected positron) visible.

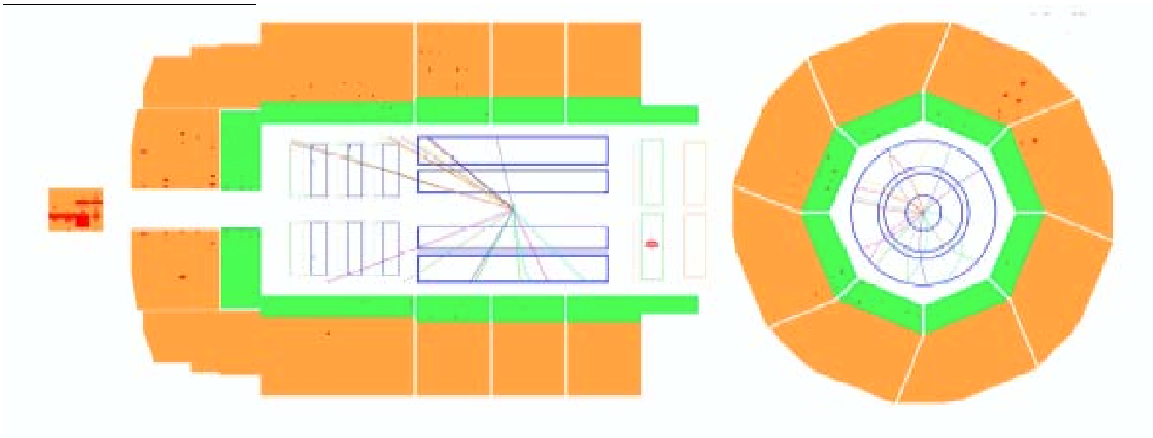

Figure 2.17: *Side view (left figure) and radial view (right figure) of low Q^2 DIS event in H1 detector. The scattered positron is detected in the SpaCal.*

Chapter 3

"It is the theory that decides what we can observe."
Albert Einstein

Theoretical Overview

It is an impressive demonstration of the unifying power of physics to realise that all the phenomena observed in the natural world can be attributed to the effects of just four fundamental forces; gravity, electromagnetism, weak, and strong force
In terms of their range (from the very small to the very large) and magnitude (from very large to very small), the forces can be summarise as follow;

- The *strong interaction* is very strong, but very short-ranged. It acts only over ranges of order 10^{-15} metres and is responsible for holding the nuclei of atoms together. It is basically attractive, but can be effectively repulsive in some circumstances.
- The *electromagnetic force* causes electric and magnetic effects such as the repulsion between like electrical charges or the interaction of bar magnets. It is long-ranged, but much weaker than the strong force. It can be attractive or repulsive, and acts only between pieces of matter carrying electrical charge.
- The *weak force* is responsible for radioactive decay and neutrino interactions. It has a very short range and, as its name indicates, it is very weak.
- The *gravitational force* is even weaker, but very long ranged. Furthermore, it is always attractive, and acts between any two pieces of matter in the Universe since mass is its source.

It was found that at the very high energies the electromagnetism and weak forces are the same manifestation of a unified force called the *electroweak* force.

This forms a central pillar to the physics and to the endeavours of physicists to unify all the known forces and show that all are different manifestations of the same primordial force upon which the edifice of our universe is formed.

This chapter deals with the theoretical frameworks that govern the world of particle physics in particular those relevant to this analysis. In explaining, predicting and modelling the behaviour of particles and their interactions at the subatomic level there have been resounding successes, models have been developed that can predict with astounding accuracy the outcome of an experiment.

The current theoretical frame work which successfully explains the forces involved in and the consequences of such interactions is the *Standard Model (SM)* of particle physics which describes three of the fundamental forces, not including *gravity* (as yet we await a theory that encompasses all four forces).

The Standard Model [19]- [21]is a Quantum Field Theory describing the elementary particles and the forces between them. According to this model the fundamental constituents of matter are 12 spin a half (1/2) fermions. The fermions are further subdivided into those which experience the strong force (*quarks*), and those which do not (*leptons*).

Furthermore the *SM* describes the interaction between particles via the exchange of spin one particles (*gauge bosons*): photon for electromagnetic interaction, the weak $W^{\pm}$ and Z^0 bosons for weak interactions, and gluons, g, for the strong interactions.

A complete description of the Standard Model is beyond the scope of this thesis; see [22]- [23]for a more in-depth discussion.

In order to probe small distances within the nucleus of an atom different techniques have been developed through the years to peer inside the minutiae of the subatomic realm and glean information about this majestic world within the building blocks of matter that make up our universe.

The quest to glimpse and unfold the secret held within an atom started with Rutherford's scattering experiment and continues today in the form of particle accelerators, which collide particles in order to study their constituents.

With each new generations of particle accelerators, as the realm of the experiments has been extended to higher and higher energies, a more precise map of the subatomic landscape has emerged. One type of experiment involving the collision of electrons and protons (*lepton-proton scattering*) has been instrumental in obtaining high-resolution images of the proton and has given fundamental insights into the nature of the forces binding the constituents of proton, the *quarks*, to one another.

At high energies, the wavelength associated with the electrons is smaller than the size of proton. Therefore one can use the electrons as probes to look at structure that is small compared with the proton, that is "*deep*" within the proton. However this high energy collision causes disruption to the structure of proton and culminates in production of several new particles (i.e. hadrons). This means that the scattering is *inelastic* as the target (i.e. proton) has been changed in the process and part of the kinetic energy of the incident particle is lost inside the target giving rise to some internal processes.

Deep Inelastic Scattering (DIS) processes, in which electrons are collided with protons, are used in HERA to study the structure of the protons. In this chapter the underlying theoretical aspects, crucial for the analysis, are discussed. The kinematic variables used to describe lepton-proton scattering are introduced in the next section, followed by a description of DIS and the production mechanism of heavy quarks in DIS.

3.1 The kinematics of *ep* Scattering

Deep Inelastic Scattering interactions are mediated by exchange of virtual bosons. Depending on the charge of this exchanged boson, the DIS events in HERA can be

classified as *Neutral Current (NC)* process ($ep \rightarrow eX$[1]) or *Charged Current (CC)* process ($ep \rightarrow \nu_e X$) , as illustrated in figure 3.1. The incident electron (e) and proton (p) have four-momenta $\kappa^\mu = (E_e, \boldsymbol{k})$ and $p^\mu = (E_p, \boldsymbol{p})$ respectively, whereas the four-momentum of the scattered electron(electron neutrinos,ν_e) is κ'^μ .

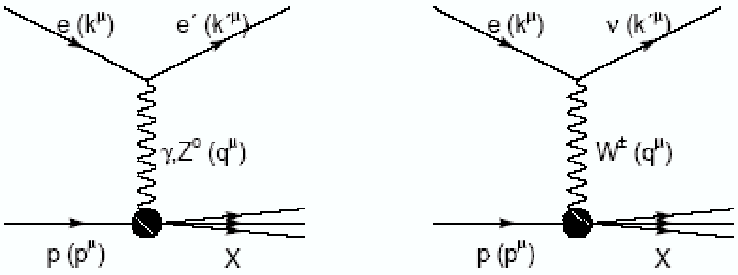

Figure 3.1: *Virtual boson exchange in ep scattering via NC (left) and CC (right) interactions.*

Neutral Current processes are mediated by the exchange of either a photon (γ) or a Z^0 boson, whereas in the charged current processes a $W^\pm$ boson is exchanged. In the following the Neutral Current reaction is discussed. At lowest order (QPM[2]) it is described by the Feynman diagram shown in Fig. 3.2, in which the four-momentum of the scattered lepton (proton) is denoted by $k'(P')$.

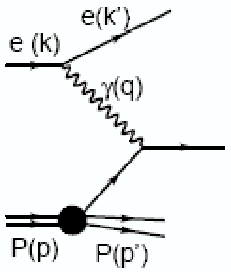

$$
\begin{aligned}
s_{ep} &= (p+k)^2 \\
Q^2 &= -q^2 = -(k-k')^2 \\
x_B &= \frac{Q^2}{2(p\cdot q)} \\
y &= \frac{p\cdot q}{p\cdot k} \\
W^2 &= (p+q)^2
\end{aligned}
$$

Figure 3.2: *Kinematics of ep scattering.*

[1] In here "X" includes all hadronic final states.

[2] *QPM* is an acronym for *Quark Parton Model*. In around 1968, electron scattering experiments at Stanford, California(SLAC), gave the first clear hints that pointlike particles existed inside the proton; these were named "Partons". Earlier, in 1964, Gell-Mann and Zweig had proposed that the proton and other elementary particles known at the time were in fact built from a more basic entities named "Quarks".When the Stanford electron scattering data were combined with the subsequent neutrino data from CERN, Geneva, it began to look as if the "partons" and "quarks" were the same entities [24].

At fixed centre of mass energy the kinematics is completely given by two variables. Usually these are selected from (the negative of) the four-momentum transfer, Q^2, the Bjorken[3] scaling variable x_B ,the inelasticity variable *y* and the invariant mass squared of the hadronic final state, W^2.

For convenience, the positive variable $Q^2 = -q^2$ which is a measure of the virtuality of the exchanged boson, is used instead of the squared four momentum itself;

$$q^2 \equiv (\kappa^\mu - \kappa'^\mu)^2 = \kappa^2 + \kappa'^2 - 2g_{\mu\nu}\kappa^\mu\kappa'^\nu = 2m_e^2 - 2E_eE_e'(1-\cos\theta_e) \tag{3.1}$$

Ignoring the mass terms (this is appropriate in HERA as the mass of the colliding particles are negligible compared to their momenta) then;

$$q^2 \approx -2E_eE'_e(1-cos\theta_e) \tag{3.2}$$

Hence;

$$\begin{aligned} Q^2 &= -q^2 \\ &\approx 2E_eE'_e(1-cos\theta_e) \end{aligned} \tag{3.3}$$

When the Q^2 of the exchanged boson is large compared to the mass of the proton, the proton is probed with high spatial resolution and the boson interacts with a constituent of the proton rather than the whole.

Bjorken [25] demonstrated that DIS can be described by two dimensionless scaling variables, the first of which, x_B , is given by

$$x_B = Q^2/2p.q \tag{3.4}$$

[3] After J.D. Bjorken

In a coordinate system in which the longitudinal momentum of the proton is very large compared with its mass ,x_B represents the fraction of the proton momentum carried by the struck quark. At HERA this so called *infinite momentum frame* can be represented to a reasonable approximation by the laboratory-frame. This interpretation can be extended to any other reference frame in which the proton has large momentum if the partons are assumed to be massless and have no momentum transverse to the proton direction. This is the basis of Quark Parton Model, where the quarks are considered to be independent point-like entities (i.e. partons), travelling co-linearly within the proton.

The second of these dimensionless Bjorken variables is the *inelasticity*, *y*, defined as

$$y = p.q/p.k \tag{3.5}$$

this is equivalent to, in the proton rest frame, the fractional energy loss of the lepton.

The squared invariant mass of the hadronic final state, which is the same as the squared mass of the photon-proton system, is given simply by

$$W^2 = (q + p)^2 \tag{3.6}$$

This can be compared with the square of the centre of mass energy in the *ep* system.

$$s_{ep} = (k + p)^2 \tag{3.7}$$

which, for the beam energies used in this analysis, has a value of 101761 GeV^2 .
If the masses of the colliding particles are neglected, then

$$\frac{Q^2}{xy} = \frac{Q^2}{Q^2/_{2p.q}\,{}^{p.q}/_{k.p}} = 2k.p = (k + p)^2 \equiv s_{ep} \tag{3.8}$$

Therefore the two dimensionless entities, Bjorken scaling variables and the Q^2 are related by

$$Q^2 = s_{ep}xy \tag{3.9}$$

Note that when $q^2 \lesssim 0$, the electron acts as a source of space-like[4] photons. For small momentum transfers, $Q^2 \ll 1$ GeV^2, the photon is 'almost real' and its behaviour tends to that of a real photon. Such low Q^2 interactions are referred to as *photoproduction* processes. As Q^2 increases, the wavelength of the virtual photon decreases until it becomes smaller than the size of the proton and then it is possible to resolve the internal structure of proton. This type of interaction is called Deep Inelastic Scattering (DIS).

The rate of an interaction is defined as the number of interactions in a fixed unit of time, so the rate R_I in ep-scattering of interaction ,I,is given by

$$R_I = \mathcal{L}\sigma_I \tag{3.10}$$

The cross section σ_I is a measure of the probability of interaction I occurring. The luminosity $\mathcal{L}$ is given by

$$\mathcal{L} = N_e N_p f / W_x W_y \tag{3.11}$$

where N_e and N_p are the number of particles in each colliding bunch. f is the frequency at which these bunches cross one another in the interaction region and W_x and W_y are parameters defined from the 2D profiles of each beam. If the particle densities in each beam are assumed to be Gaussian, along the same axis and the same in x and y then;

$$W_x W_y = 2\pi(V_e + V_p) \tag{3.12}$$

where V_e and V_p are the variance of the Gaussians of the electron and proton beams respectively. The luminosity measurement at H1 is described in section 2.5.

In the following sections only the DIS regime is discussed for a detailed discussion on photoproduction see [84] .

[4] Particles with $q^2 > 0$ are said to be time-like.

3.2 DIS: Probing the structure of the Proton

In experiments at the HERA collider, the substructure of the proton is probed in collisions with electrons down to length scales of the order of 10^{-18} m and with higher precision than any experiment before. For values of $Q^2 \geq 1$ GeV^2 the "virtual[5]" photon begins to be able to resolve the internal substructure of the proton. This is the transition from photoproduction to DIS regime, where the constituent partons are probed as depicted in figure 3.3. As Q^2 increases to the order of $M_{Z^0}^2, M_{W^\pm}^2$ (the squared masses of Z^0 and $W^\pm$ respectively), the heavier Z^0 and $W^\pm$ exchange bosons also contribute to the DIS, for the analysis in this thesis, photon exchange dominates and Z^0 and $W^\pm$ exchange can be ignored.

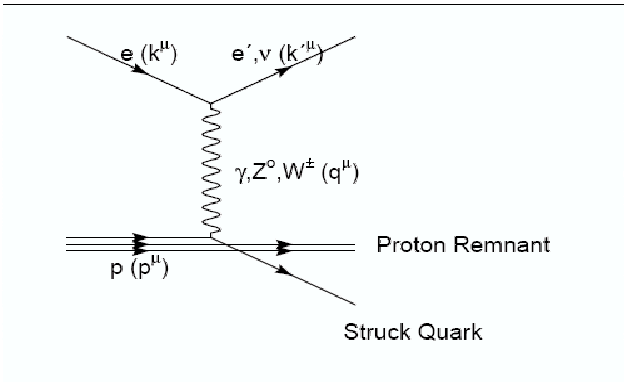

Figure 3.3:*Deep Inelastic Scattering. The incident electron, scattered lepton, exchange boson and proton have four-momenta* $\kappa^\mu, \kappa'^\mu, q^\mu$ *and* p^μ *respectively.*

In the Q^2 range of this analysis the proton substructure can be characterised by two structure functions F_1 and F_2, that describe the distribution of the electric charge and of the magnetic moment in the proton. These structure functions are generalisations of the nuclear *form factor* [26] . At high Q^2 , where the exchange of the Z^0 is significant, a third *parity violating structure function* namely xF_3 is required to describe full neutral current cross section.

The process of electron-proton scattering can be elastic($ep \longrightarrow ep$electron-proton scattering) where proton remains intact, or inelastic when the virtual boson interacts with a constituent of the proton and results in disintegration of the proton ($ep \longrightarrow eX$).

[5] The virtual photon is 'off-mass-shell', meaning that $E=pc$ is violated, and implying that it temporarily has a non-zero mass [27].

In low energy elastic scattering, the photon effectively perceives the nucleon as an extended object and the structure function essentially describes the spatial distribution of electrical charge on the proton. This leads to a dependence of the structure function on the momentum of the photon. Whereas in the very high energy deep inelastic scattering, the photon has resolved down to such an extent that the existence of the complete nucleon is really irrelevant to the interaction, the photon interacts with only a small part of the nucleon and does so independently of the rest of it.

The above phenomena can be expressed in terms of a cross-section for electron proton scattering in which the cross section for elastic electron-proton scattering processes is observed to be rapidly falling with increasing magnitude of the four-momentum transfer Q^2 as depicted in figure 3.4. Simultaneously, the *proportion* of inelastic scattering processes, increases.

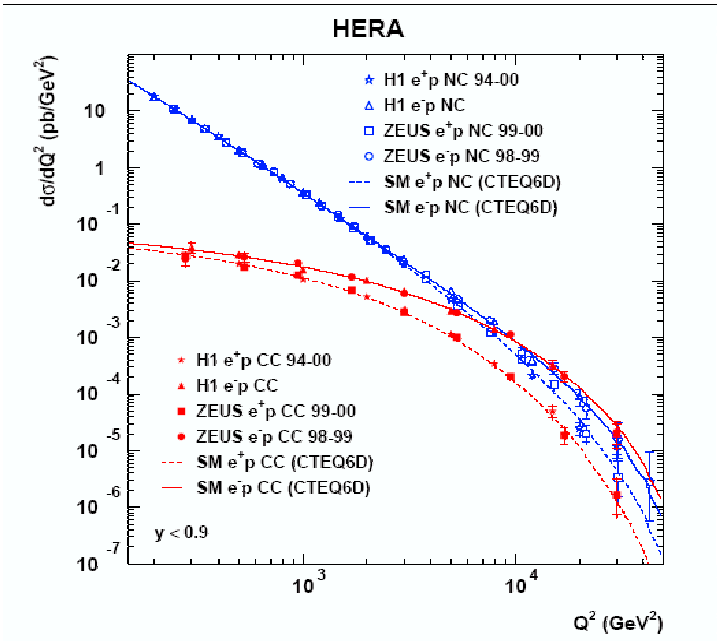

Figure 3.4: *Cross-section for Neutral Current (blue) and Charge Current (red) as a function of Q^2* [30].

Assuming that the electromagnetic interaction between electron and proton is dominated by the exchange of a single virtual photon then the mathematics used to describe the reaction becomes relatively simple.

The formula is made up of factors associated with the different parts of the diagram in figure 3.3. It consists of factor describing the progress of the electron through the

reaction (the lepton current), a factor describing the propagation of the virtual photon, and a factor describing the flow of the nucleon in the reaction including the complicated disintegration process (the hadron current). The inclusive differential cross section for inelastic electron-proton scattering in its lowest order in QED can be expressed as:

$$\frac{d^2\sigma_{ep\to eX}}{dxdQ^2} = \frac{\alpha_{em}^2 E\prime}{Q^2 E} L_{\mu\nu} W^{\mu\nu} \tag{3.13}$$

In the above equation E (E') is the energy of the incoming electron (scattered electron) in laboratory frame, and $L_{\mu\nu}$ and $W^{\mu\nu}$ are the lepton and proton currents respectively, whereas α_{em} is the electromagnetic coupling constant. The factors describing electron and photon are well known from QED, but the factor describing the hadron current is a complicated unknown describing the evolution of the nucleon structure during the interaction and can only be determined by the deep inelastic experiments. Using the constraint of Lorentz current conservation the unknown structure of the proton can be parameterised in terms of two[6] independent *Structure Functions*, $F_1(x,Q^2)$ and $F_2(x,Q^2)$, and one can rewrite equation (3.13) in term of proton structure functions as follows;

$$\frac{d^2\sigma_{ep\to eX}}{dxdQ^2} = \frac{4\pi\alpha_{em}^2}{xQ^4}[xy^2F_1(x,Q^2) + (1-y)F_2(x,Q^2)] \tag{3.14}$$

A minimum of two structure functions are required because the photo-absorption cross section has two independent contributions, σ_T and σ_L, which arises from transversal and longitudinal polarised photons respectively. It is found that $2xF_1$ is proportional to σ_T and that F_2 is proportional to $\sigma_T + \sigma_L$. A longitudinal structure function can be introduced which is proportional to σ_L alone. It is related to F_1 and F_2 by,

$$F_L = 2xF_1 - F_2 \tag{3.15}$$

Equation 3.14 can then be rewritten as,

$$\frac{d^2\sigma_{ep\to eX}}{dxdQ^2} = \frac{4\pi\alpha_{em}^2}{xQ^4}\left(1 - y + \frac{y^2}{2[1+R(x,Q^2)]}\right)F_2(x,Q^2) \tag{3.16}$$

Where the photo-absorption ratio, $R(x,Q^2)$, is defined by

[6] The presence of parity violation for W and Z^0 exchange leads to the introduction of a third structure function $F_3(x,Q^2)$.

$$R(x,Q^2) = \frac{\sigma_L(x,Q^2)}{\sigma_T(x,Q^2)} = \frac{F_L(x,Q^2)}{F_2(x,Q^2) - F_L(x,Q^2)} \quad (3.17)$$

The structure function $F_2(x,Q^2)$ is extracted from equation (3.16) by measuring the differential cross section $\frac{d^2\sigma_{ep\to eX}}{dxdQ^2}$, and estimating the contribution of F_L.

In figure (3.5) a recent measurement of the structure function F_2 of proton by H1 collaboration is depicted. F_2 is shown as a function of Q^2 for different values of x. For values of x between about 0.1 and 0.2, where the early fixed target measurements of the proton structure function were made, the proton structure function can be seen to be nearly independent of the four-momentum transfer Q^2 with which the proton substructure is probed. This behaviour is called *scaling*. However F_2 is seen to rise with Q^2 at low x and, to a lesser degree, to fall with Q^2 at high x, these deviations are known as *scaling violations*. This phenomenon is further discussed in detail in the next section.

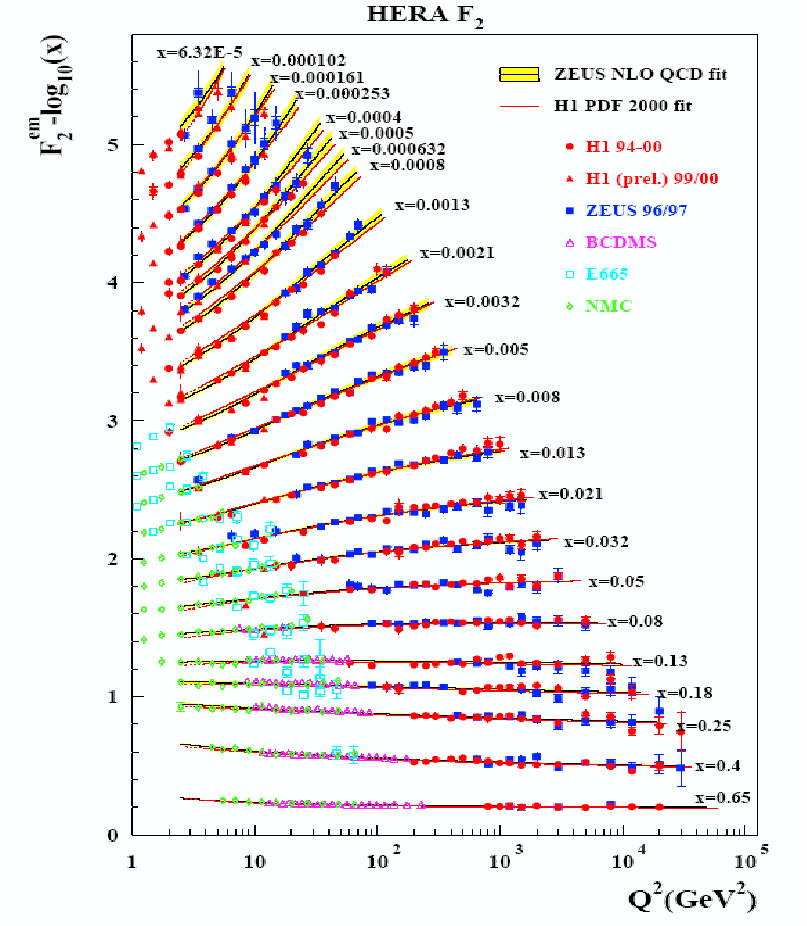

Figure 3.5: *Proton structure function $F_2(x,Q^2)$ as a function of Q^2 for a range of different x values.*

3.2.1 Scaling and the Quark-Parton Model.

Scaling is the name given to a phenomenon of the cross-section, which was first predicted by James Bjorken [27]. Stated simply the prediction is that when the momentum carried by the probe becomes large, then the dependence of the cross-section on the parameters such as the energy and the momentum squared,Q^2, transferred by the photon, becomes very simple. In particular, the structure function becomes independent of Q^2. This can be explained in the Quark-Parton Model, in which proton is viewed, as a collection of point-like, non-interacting constituents; the *partons* [7].

In the Quark-Parton model the complicated scattering of the probe off a proton of finite spatial extent has been replaced by scattering off a point-like parton. The photon ceases to scatter off a proton as a *coherent object* and instead, scatters off the individual point-like partons *incoherently*. The lack of length scale, due to the point-like nature of the partons, naturally explains the scale invariance observed experimentally.

For a detailed explanation of the *scaling violations* we need the help of *Quantum Chromo Dynamics* (QCD), of which the QPM is now known to be merely an approximation. In contrast of the QPM, *Quantum Chromo Dynamics* is a *dynamic* theory that includes interactions between the constituents of the proton. In QCD, the partons are identified as *quarks*, carrying a quantum number, the *colour charge*, and interacting by the exchange of *gluons*, which themselves carry combinations of colour and anti-colour charges. The gluons represent the *guage bosons* of QCD and bind the quarks inside the proton. In contrast to photons, the electrically neutral gauge bosons of QED, gluons can couple to other gluons due to their colour charge.

[7] The Parton Model was first put forward by R.Feynman, in which no initial assumptions about the partons are necessary. It is the purpose of the experiments to determine their nature [21].

This interaction of gluons with other gluons results in a specific dependence of the strong coupling constant α_s (see Appendix C) on the resolution parameter Q^2, which in leading order logarithm approximation is described by [23].

$$\alpha_S = \frac{12\pi}{(33-2N_f).\ln(Q^2/\Lambda^2_{QCD})} \tag{3.18}$$

Where $N_f = 6$ is the number of quark flavours and Λ_{QCD}[8] is a scale parameter, the value of which has been determined experimentally to be $\Lambda_{QCD} \approx 200\ MeV$ [28] .

For Q^2 values much larger than Λ^2 the effective coupling is small and a perturbative description in which the quarks and gluons interact only weakly (are 'quasi-free')makes sense. For Q^2 of order Λ^2, perturbative calculation cannot be used, since quarks and gluons will arrange themselves into strongly bound clusters, namely, hadrons and can no longer be treated as approximately independent. Thus Λ can be thought of as the line that separates the world of quasi-free quarks and gluons, and the world of bound states hadrons such as pions, protons, and so on[31].

This behaviour of the strong coupling constant is in contrast to the electromagnetic coupling strength α_{QED} that *increases* at short distances. The decrease of the strong coupling constant at short distances is a property known as *asymptotic freedom*. It is in the limit of asymptotic freedom, that the Quark-Parton Model can be derived from QCD.

The rise of the proton structure functions with increasing Q^2 at low x and the decease at high x are a feature of the gluon interactions in Quantum-Chromodynamics.

It is hypothesized within the QCD framework that the quarks inside the proton endlessly emit and re-absorb gluons, which may then fluctuate into virtual quark anti-quark pairs. These virtual quark anti-quark pairs are termed "*sea quarks*" to distinguish them from the original quark content of the proton in the static Quark-Parton Model, the "*valence quarks*". The extent to which the virtual quarks contribute to the electron-proton scattering cross-section depends on the resolution parameter Q^2 with which the proton is probed. With increasing Q^2, the photon emitted by the electron is more likely to find the proton in a state in which one of the valence quarks

[8] From equation (3.18) we see that at sufficiently low Q^2, effective coupling will become larger. It is customary to denote the Q^2 scale at which this happens by Λ^2 .

has radiated one or more gluons and is surrounded by a cloud of virtual quark anti-quark pairs (see figure 3.6 for illustration).

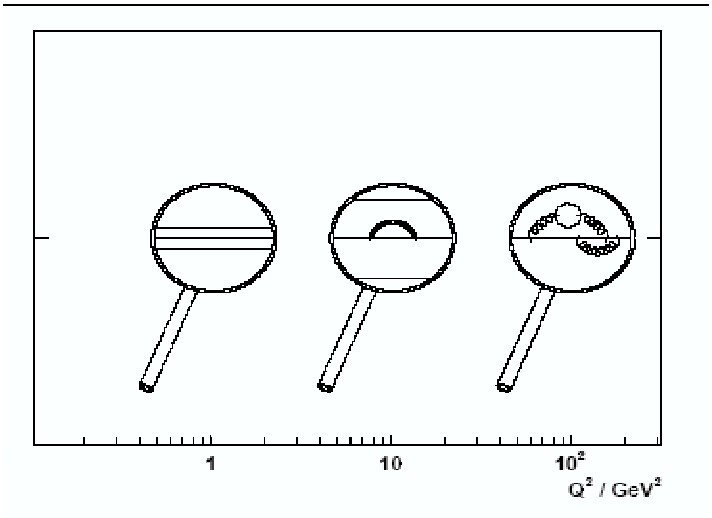

Figure 3.6: *Illustration of proton structure as observed at different Q^2 value.*

In this case, the photon may scatter off one of the sea quarks, which typically carry only a small fraction x of the proton's momentum, explaining the rise of the proton structure function at low x. On the other hand if the photon, scatters off a valence quark that has radiated gluons, the struck quark carries on average a smaller fraction x of the proton's momentum than it would, had it not emitted any gluons. That is with increasing resolution Q^2 the proton is more likely to be "seen" by the photon in a state in which the proton's momentum is distributed over a large number of "soft" partons, such that the probability to find a large fraction of the proton's momentum concentrated in a single "hard" parton decreases.

3.2.2 QCD evolution

As discussed earlier, it can be seen from Figure 3.5 that the scaling behaviour, expected in the naïve QPM, is observed only for values of Bjorken x about 0.13. In all other x-regions F_2 depends logarithmically on Q^2. Furthermore there is a strong dependence of F_2 on Bjorken x itself which is changing with Q^2, as shown in Figure 3.7

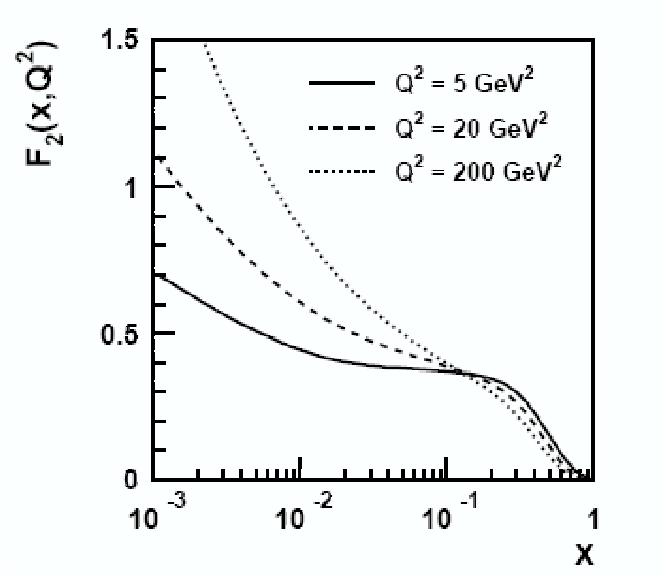

Figure 3.7: *The proton structure function $F_2(x, Q^2)$ as a function of Bjorken x.*

Although the *scaling violation* of the structure functions is expected in QCD, an exact calculation is not possible and it must be evaluated approximately. Perturbative QCD calculations can be performed in the formalism of *collinear factorization* in which evolution equations [32] [33] are used to describe the radiation of partons from the initial parton distribution in the proton and in the photon[9]. In the collinear factorisation the parton distributions in the proton (and the photon) are assumed to depend only on the scaling variable x and the energy scale μ, which is usually the photon virtuality Q^2. In particular, the initial partons in the proton are assumed to carry no transverse momentum. In the evolution, the partons are treated as massless on-shell particles. Factorization and renormalisation scale parameters are used to absorb divergent parts of the perturbation series into parton distributions and α_s.

Several models of the evolution of parton densities inside the proton have been established and will be briefly discussed in this and the next sections. The evolution equations are known as DGLAP [32], [33], BFKL [34], [35]and CCFM [29] [36]. DGLAP and BFKL model the evolution of $F_2(x, Q^2)$ with Q^2 and x, respectively, and

[9] Due to Heisenberg uncertainty principle which in natural units can be written as $\Delta E \Delta t > 1$, the photon is allowed to violate the rule of conservation of energy by an ammount of energy ΔE for a short period of timeΔt and fluctuate into a charged fermion anti-fermion system carrying the same quantum numbers as the photon. If during such a fluctuation, one of the fermions interacts via a gauge boson with another object, then the parton content of the photon is resolved and the photon reveals its structure. In such interactions the photon can be regarded as an extended object consisting of charged fermions and also gluons, the so-called resolved photon. This possibility for the photon to interact either directly or in a resolved manner is another dual nature of the photon.

CCFM scheme is a mixture of DGLAP and BFKL. An approximation lies in the fact that the models only use leading terms of the full QCD expansion. As a result, the models may work only in a limited part of the phase-space.

In the DGLAP parton evolution scheme, the gluon emissions are strongly ordered in their transverse momenta, from very small momenta for the initial emissions in the proton to larger momenta for emissions closer to the hard interaction with the photon.

In the BFKL scheme, the gluon emissions are strongly ordered in energy, from large energies for initial emissions in the proton to smaller energies closer to the hard interaction, while no strong ordering in the transverse momenta is predicted.

The CCFM approximation [36], attempts to combine features from both the DGLAP and BFKL approximations and provides a satisfactory description of many aspects of the data in the wide kinematic region. In this scheme the emissions are ordered in the angle with respect to the proton direction, from small angles for the initial emissions to the larger angles closer to the hard interaction.

The DGLAP, BFKL and CCFM evolutions describe the evolution of parton densities with Q^2 and/ or with x via quark-gluon and gluon-gluon splitting which generates increasingly rising densities at low x. However it is important to consider that at very high gluon densities, the gluons can recombine via the recombination process $gg \rightarrow g$ and thus damp the rise of $F_2(x, Q^2)$ towards low x.

3.2.3 DGLAP evolution

In the DGLAP (Dokshitzer, Gribov, Lipatov, Altarelli and Parisi) scheme [32], [33] only powers of $\alpha_s \ln(Q^2/Q_0^2)$ from the perturbative QCD expansion are considered in a *leading logarithm* approximation. Thus this approximation is valid only at large enough Q^2 where α_s is small and $\ln(1/x)$ terms are not important.

The evolution of the quark and gluon densities with Q^2 is given by the following coupled equations

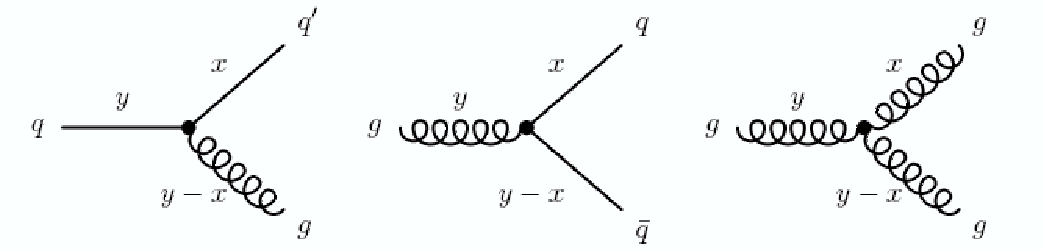

Figure 3.8: *Graphs of the leading order DGLAP splitting functions* $P_{ij}^{(0)}(x/y)$ *for* $P_{qq}(q \rightarrow qg)$, $P_{qg}(g \rightarrow q\bar{q})$, *and for* $P_{gg}(g \rightarrow gg)$ *splitting(from left).*

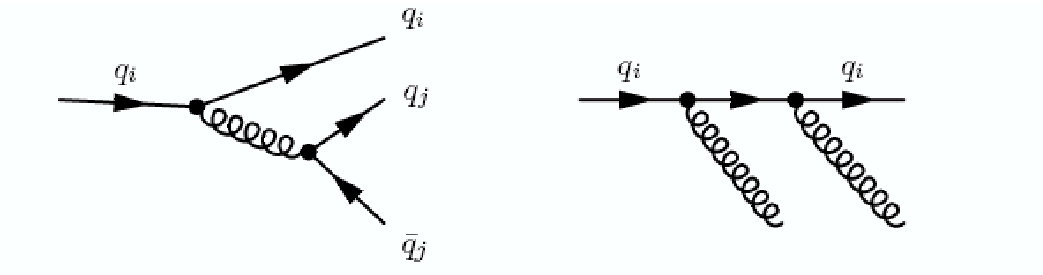

Figure 3.9: *Feynman diagrams contributing to the Next to Leading Order (NLO) splitting functions* $P_{qq}^{(1)}$ *and* $P_{q\bar{q}}^{(1)}$.

$$\frac{dq_i(x,Q^2)}{d\,lnQ^2} = \frac{\alpha_s}{2\pi}\int_x^1 \frac{dy}{y}\left[\sum_j q_j\,(y,Q^2)P_{q_iq_j}(x/y) + g(y,Q^2)P_{q_ig}(x/y)\right] \qquad (3.19)$$

$$\frac{dq_i(x,Q^2)}{d\,lnQ^2} = \frac{\alpha_s}{2\pi}\int_x^1 \frac{dy}{y}\left[\sum_j q_j\,(y,Q^2)P_{gq_j}(x/y) + g(y,Q^2)P_{gg}(x/y)\right] \qquad (3.20)$$

The functions $P_{ij}(x/y)$ are the splitting functions (see Figure 3.8) describing, in their leading order, the probability of finding a parton of species i with momentum fraction x within a parton species j with momentum y. For simplicity, q_i is used to denote quark densities as well as anti-quark densities.

The functions $P_{ij}(x/y)$ are calculable in perturbative QCD as a power series of $\alpha_s(Q^2)$

$$P_{ij}\big(z,\alpha_s,(Q^2)\big) = P_{ij}^{(0)}(z) + \frac{\alpha_s}{2\pi}P_{ij}^{(1)}(z) + \ \ldots \qquad (3.21)$$

The functions $P_{ij}^{(n)}$ are presently known up to order n=2, in the so called next-to-next-to-leading order approximation (NNLO). Examples of NLO Feynman diagrams are shown in Figure 3.9.

The evolution equations (3.20) and (3.21) look particularly simple when written in terms of moments. The *n*th-moment of a function *f(x)* is defined as

$$f(n) = \int_0^1 x^n \ f(x)dx. \tag{3.22}$$

The re-written evolution equations describing the convolution of a density and a splitting function lead to a simple multiplication in momentum space:

$$\frac{dq_i(n,Q^2)}{d\ lnQ^2} = \frac{\alpha_s}{2\pi}\left[\sum_j P_{q_i q_j}(n) q_i(n,Q^2) + P_{q_i g}(n) g(n,Q^2)\right] \tag{3.23}$$

$$\frac{dg(n,Q^2)}{d\ lnQ^2} = \frac{\alpha_s}{2\pi}\left[\sum_j P_{g_i q_j}(n) q_i(n,Q^2) + P_{g} g(n) g(n,Q^2)\right] \tag{3.24}$$

Due to the probabilistic interpretation of the leading order splitting functions $P_{ij}^{(0)}$ these are positive for $x < 1$ and satisfy the following sum rules

$$\int_0^1 P_{qq}^{(0)}(z)dz = 0, \tag{3.25}$$

$$\int_0^1 z\left[P_{qq}^{(0)}(z) + P_{gq}^{(0)}(z)\right] dz = 0, \tag{3.26}$$

$$\int_0^1 z\left[2n_f P_{qg}^{(0)}(z) + P_{gq}^{(0)}(z)\right] dz = 0, \tag{3.27}$$

which correspond to quark number and momentum conservation.
An important feature of the DGLAP evolution is the strong ordering in the momentum transfer squared and weak ordering in the longitudinal momenta

$$Q^2 \gg k_{T,n}^2 \gg k_{T,n-1}^2 \gg \cdots \gg Q_0^2, \tag{3.28}$$

$$x < x_n < x_{n-1} < \cdots < x_1\,, \tag{3.29}$$

where Q_0^2 is the starting scale, typically of order of few GeV^2.

For a schematic depiction of the areas of phase space relevant for the two evolution equations (DGLAP and BFKL) refer to Figure 3.10.

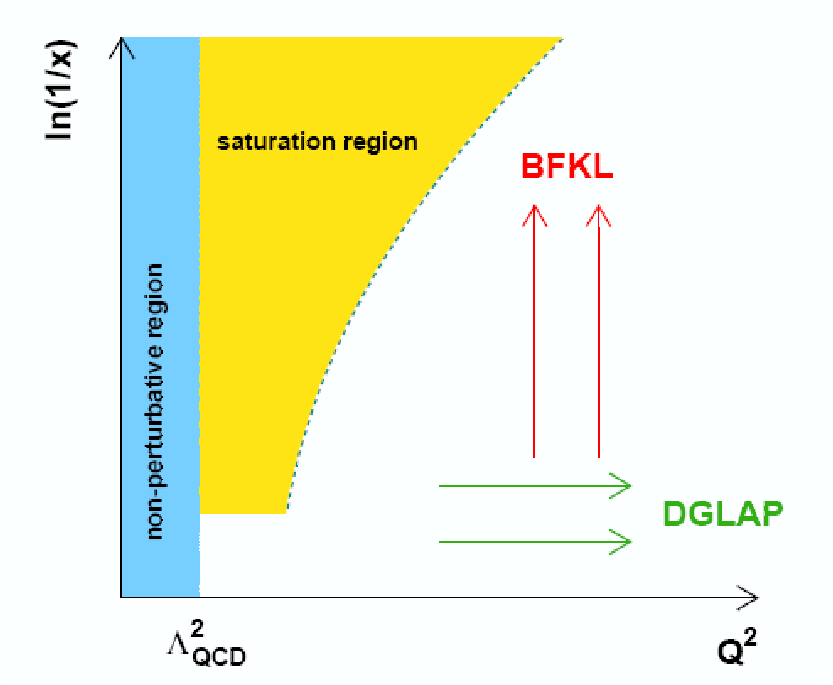

Figure 3.10: *Schematic phase space diagram for deep inelastic scattering. Directions of DGLAP and BFKL evolutions are marked by arrows. In the non-perturbative regions* $Q^2 < \Lambda^2_{QCD}$ *(blue rectangle) the coupling is large and not much is known here in terms of perturbative QCD. The saturation region (yellow area) an be understood by means of perturbative methods at low x.*

3.2.4 BFKL evolution

In the BFKL (Balitsky, Fadin, Kuraev, Lipatov) [34]- [35] approximation, only terms with powers of $\alpha_s \ln(1/x)$ are considered while terms involving $\alpha_s \ln(Q^2/Q_0^2)$ are neglected in the leading logarithm approximation. Thus BFKL is expected to be a good approximation in a different region than DGLAP, namely at very low x but at Q^2 large enough in order to work with reasonably small values of $\alpha_s(Q^2)$ see figure 3.10.

Unlike DGLAP, there is no strong ordering in Q^2 while strong ordering in x, corresponding to time-ordering in the proton rest frame, is required

$$x \ll x_n \ll x_{n-1} \ll \cdots \ll x_1 , \qquad (3.30)$$

An *unintegrated gluon distribution* $f(x,k_T^2)$ is defined for $k_T^2 \neq 0$ by

$$xg(x,Q^2) = \int_0^{Q^2} \frac{dk_T^2}{k_T^2} f(x,k_T^2), \tag{3.31}$$

for which the BFKL evolution equation reads

$$\frac{df(x,k_T^2)}{dln(1/x)} = \int d\acute{k}_T^2 k_L(k_T^2, \acute{k}_T^2) f\left(k_T^2, \acute{k}_T^2\right) = k_L \otimes f = \lambda f, \tag{3.32}$$

where $\otimes$ stands for convolution and k_L is the *Lipatov kernel* representing the sum over powers of $\alpha_s \ln(1/x)$ terms. From the last equality in equation (3.32) it is obvious that the function f follows a *power-law* behaviour in the variable x. The resulting gluon distribution can be expressed as

$$xg(x,Q^2) \sim f(Q^2) x^{-\lambda}. \tag{3.33}$$

Hence, the behaviour of the structure function is predicted to be proportional to $x^{-\lambda}$ (for a dominant gluon contribution) although the constant λ is not well constrained. It's value in the next-to-leading logarithm approximation (NLLA) is $\lambda \sim 0.17$ [[37]] while in the leading logarithm approximation (LLA) it is $\lambda = \frac{12 \ln 2}{\pi} \alpha_s \sim 0.5$ [34]-[35].

3.2.5 CCFM evolution

The CCFM (Ciafaloni, Catani, Fiorani & Machesini) equation is the application of angular ordering to the calculation of the gluon ladder.

QCD colour coherence implies angular ordering of emissions along the parton chain, so that it is necessary to work in terms of parton distributions $f_a(x,k_T^2,\mu^2)$, which are unintegrated over k_T. These distributions depend on two hard scales: k_T and the scale μ of the probe. They are described by the CCFM evolution equations [29], [36], which is valid both at large and small x, since it resums terms of both the form $(\alpha_s \ln(\frac{1}{x}))^n$ and $(\alpha_s \ln(\frac{1}{1-x}))^n$. This means that at large x the CCFM evolution behaves similar to DGLAP evolution, and at small x it will be BFKL-like, because

both DGLAP and BFKL evolutions are the two limits of the angular-ordered evolution. In the DGLAP collinear approximation, the angle increases due to the growth of k_T, while in the BFKL approach, the angle ($\theta \approx {k_T}/{k_L}$, where k_L is the longitudinal momentum) grows due to the decrease of the longitudinal momentum fraction, x, along the chain of parton emissions from proton. The angular ordering is a consequence of the interference of soft gluon radiation (or coherence), where strongly effects the hard parton scattering close to the kinematic boundaries $x \longrightarrow 0$ and 1.

The CCFM evolution includes angular ordering in the initial state cascade, which means that the emission angles of the partons with respect to the propagator increases as one moves towards the quark box,

$$\Xi \gg \xi_n \gg \cdots \gg \xi_1 \gg \xi_0\,, \tag{3.34}$$

where the maximum allowed angle Ξ is set by the hard quark box [85],

$$p_q + p_{\bar{q}} = \Upsilon\left(p_p + \Xi_{p_e}\right) + Q_T. \tag{3.35}$$

Q_T is the transverse momentum of the quark pair and Υ is its light cone momentum fraction. Equation (3.35) is written in terms of Sudakov variables [86], where $p_q, p_{\bar{q}}$ are the four momenta of the produced quarks and p_p and p_e are the proton and electron momenta. The momenta of the emitted gluons can be written as

$$p_i = \nu_i\left(p_e + \xi_i p_p\right) + p_{T_i},\quad \xi_i = \frac{p_{T_i}^2}{s\nu_i^2} \tag{3.36}$$

where $\nu_i = (x_{i-1} - x_i)$ is the momentum fraction of the emitted gluon, p_T is the tranverse momentum of the gluon, and $s = (p_e + p_p)^2$. It is assumed here, that all particles are massless.

The CCFM equation can be written as

$$\bar{q}^2 \frac{d}{d\bar{q}^2}\frac{xA(x,k_T^2,\bar{q}^2)}{\Delta_s(\bar{q}^2,\mu_0^2)} = \int dz \frac{d\phi}{2\pi}\frac{\tilde{P}\left(z,k_T^2,\left({\bar{q}}/{z}\right)^2\right)}{\Delta_s(\bar{q}^2,\mu_0^2)} x'A'(x', k'^2_T, (\bar{q}/z)^2) \tag{3.37}$$

where $A(x, k_T^2, \bar{q}^2)$ is the gluon density unintegrated in k_T. It depends also on x and evolution variables $\bar{q}_i^2$:

$$\bar{q}_i = \frac{p_{T_i}}{1-z_i} = x_{i-1}\sqrt{s\xi_i}\,, \tag{3.38}$$

which are the scaled transverse momenta of the emitted gluons and $z_i = \frac{x_i}{x_{i-1}}$. In this formalism, (3.34) bcomes

$$q_i > z_{i-1}q_{i-1}. \tag{3.39}$$

The Sudakov form factor Δ_s [115] describes the probability that there are no emissions from the starting scale μ_0^2 to the maximum rescaled transverse momentum $\bar{q}_{max}^2$.

$$\Delta_s(\bar{q}, Q_0) = \exp\left(-\int_{Q_0^2}^{\bar{q}^2} \frac{dq^2}{q^2} \int_0^{1-Q_{0/q}} dz \frac{\bar{\alpha}_s(q^2(1-z)^2)}{1-z}\right) \quad (3.40)$$

where $\bar{\alpha}_s = {C_A \alpha_s}/{\pi}$. For inclusive quantities at leading-logarithmic order the Sudakov form factor cancels the 1/(1-z) collinear singularity of the splitting function. The CCFM splitting function $\tilde{P}$ is defined as

$$\tilde{P}_g\left(z, k_T^2, (\bar{q}/z)^2\right) = \frac{\bar{\alpha}_s(q_i^2(1-z_i)^2)}{1-z_i} + \frac{\bar{\alpha}_s\left(k_{T_i}^2\right)}{z_i} \Delta_{ns}\left(z_i, k_{T_i}^2, q_i^2\right). \quad (3.41)$$

The difference between the CCFM and the DGLAP splitting functions is that the CCFM splitting functions include the singular parts of the DGLAP splitting functions. There is also one additional function Δ_{ns}, called the non-Sudakov form factor, which originated from the fact that, in CCFM and BFKL, all virtual corrections in the gluon vertex are automatically taken into account. This is called the Reggeisation of the gluon vertex.

As parton densities cannot be calculated from first principles. They have to be given at some reference scale and then they can be computed from any value of the scale. The determinations of the parton distributions are made with the evolution equations which fit $q, \bar{q}$ and g to data at a variety of Q^2. The determination of PDFs requires detailed treatments of the experimental and theoretical uncertainties.

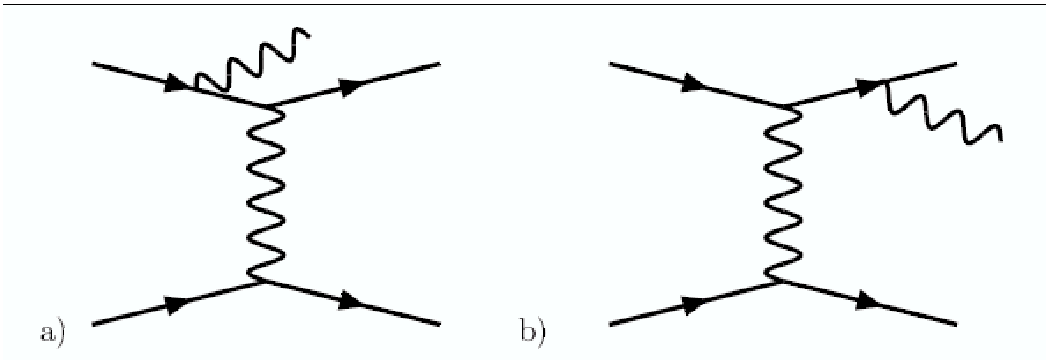

Figure 3.11: *Feynman diagrams of the first order QED corrections to the lepton-quark scattering corresponding to the initial (a) and final (b) state radiation of the photon from the interacting electron.*

3.2.6 Radiative QED Corrections

Radiative QED corrections to deep inelastic scattering are due to the emission of real photons, virtual loops or due to exchange of an additional photon. They are strongly suppressed by factors proportional to $\alpha_{QED} = 1/137$. However, in some regions of the phase-space within the detector acceptance these corrections become important or even dominant.

Three major sources can be distinguished in the leading logarithm approximation (LLA) of QED radiative corrections. When the photon is emitted from the incoming electron almost collinearly, see Figure 3.11 (a), the process is called initial state radiation (IRS). Final state radiation (FSR), Figure 3.11 (b), is analogous to ISR but the photon is emitted from the scattered electron. A third process is called QED Compton scattering where the photon is emitted from the interacting electron, as in the case of ISR or FSR, but at large angles while the electron undergoes only a small variation in its direction due to the exchange of the virtual photon in the interaction with the proton. These events have a clear signature since the outgoing electron and the radiated photon occur back to back in the polar angle ϕ .

ISR events may be employed to measure deep inelastic scattering at low values of Q^2. They are basically regular DIS events with the centre of mass energy s decreased by the photon radiation. Hence the kinematics of such events must be reconstructed with a method insensitive to the incoming electron energy and account for a different centre of mass energy s . Such a method could be, e.g., the so called *sigma method* which will be discussed in the Analysis section of this thesis.

3.3 Production Mechanism of Heavy Quarks in DIS

The heavy quarks, *charm* and *beauty*, do not exist as stable particles in nature, since they decay into lighter quarks. They were discovered with modern particle accelerators which provide enough energy to produce them. They form bound states with other quarks which then decay in an extremely short time, of the order of a picosecond (10^{-12} sec). Since the discovery of charm in 1974 and beauty in 1977 there have been detailed experimental investigations to understand the interactions of these particles. Their large masses make them especially interesting for study of the strong interactions, since the strong force is weaker for harder scales and thus better

calculable. However the accurate understanding of how charm and beauty quarks are produced in hadronic environments is still an open issue.

At the HERA storage ring at DESY, electrons of 27.6 *GeV* of energy are collided with 920 GeV protons, providing an *ep* center-of-mass energy of 318 GeV. This offers great opportunities to study the production mechanisms of heavy quarks and to test all aspects of QCD, in both perturbative and non-perturbative regimes.

The main reason and interest in the production of *charm* and *beauty* quarks at HERA can be related to the fact that these quarks with masses $m_c \approx 1.5$ GeV and $m_b \approx 4.75$ GeV, *charm* and *beauty* respectively, are too heavy to be stable constituents of the proton which has a mass of $m_p \approx 0.935$ GeV, therefore special production mechanisms are needed to explain the phenomenon.

. The most important mechanism for heavy quark production in DIS is through photon-gluon fusion (*PGF*) which is directly sensitive to the gluon momentum density (*PGF* is shown in the left plot of figure 3.12.) on the same figure on the right, for comparison, a Born level diagram of light quark scattering is shown also. Besides direct photon interactions, as shown in the figure3.12, there exist also resolved photon processes, where the photon fluctuates hadronically before the hard interaction, as illustrated in the left hand part of figure 3.13. At HERA resolved photon processes play an important role in photoproduction, where $Q^2 \sim 0$ GeV^2, and are suppressed in the deep inelastic scattering (DIS) regime $Q^2 > 1$ GeV^2.

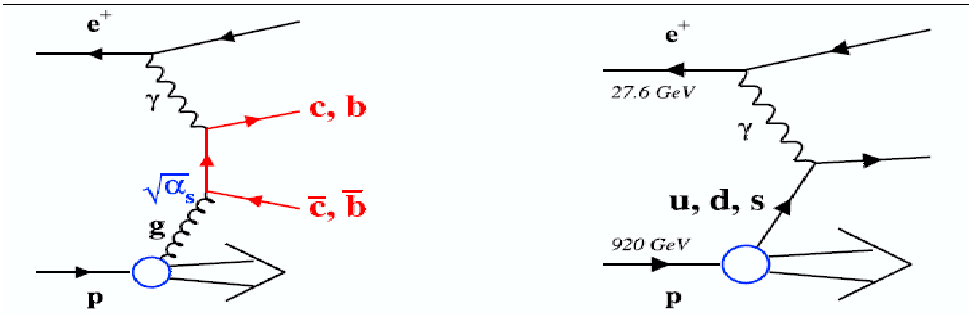

Figure 3.12: *The left plot illustrate the dominant production process for charm and beauty quarks in ep collision at HERA, the photon gluon fusion (PGF) reaction. The right plot depicts for comparison the simplest diagram for light quark scattering.*

In contrast, the light valence or sea quarks in the proton can scatter directly off the electron with only the electromagnetic force (photon exchange) involved as depicted in the right plot of figure (3.12).

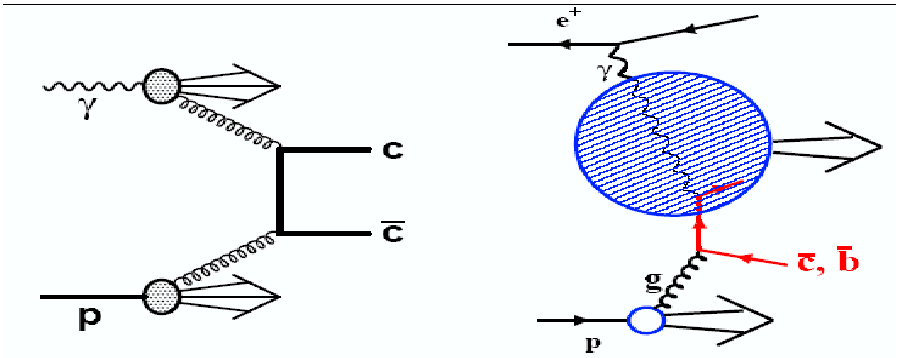

Figure 3.13: *Leading order resolved photon diagrams for charm and beauty production in the massive scheme (left) and in the massless scheme (right).*

At the x and Q^2 values probed at H1 heavy quarks may contribute up to 30% of the structure function F_2 [29]. In the framework of QCD the cross section of a process may be calculated using a perturbative expansion in the coupling constant. Perturbative calculations can be applied if there is a large scale compared to the QCD parameter $\Lambda_{QCD} = 0.26$ GeV so that the coupling constant is small.The heavy quarks, i.e. *charm, beauty* and *top*, which have masses $m \gg \Lambda_{QCD}$, provide such a scale.

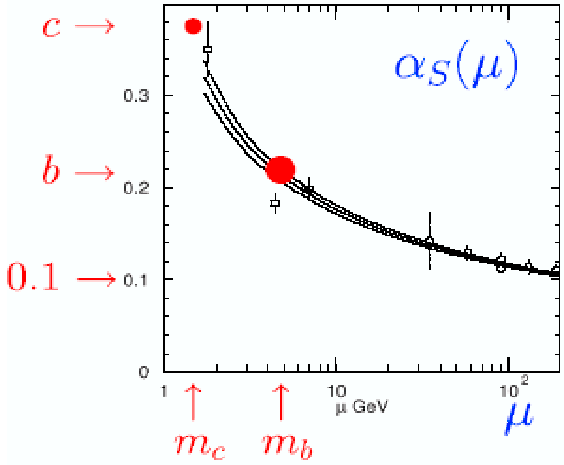

.

Figure 3.14: *Running coupling constant α_s of the strong force as a function of hard scale μ .*

The heavy quark masses can set the hard scale even if there are no other hard scales available. This is illustrated in figure 3.14, which shows the running coupling constant α_s as a function of the hard scale μ. At the scales of heavy quark masses, $\alpha_s(m_c)$ and even more $\alpha_s(m_b)$ is small enough that higher order processes, i.e. with further gluons involved, are expected to be suppressed.

The QCD hard scattering factorisation theorem [38] can be applied to the process.

This states that the proton gluon density, determined indirectly from the variation of the inclusive structure function F_2 with changing photon virtuality Q^2(see figure 3.15), is universal and can be used to predict exclusive hard processes, such as heavy flavour production. Note that the relevant range of the proton momentum fraction x carried by gluon, which can be probed with the photon-gluon-fusion (PGF) process at HERA is $\sim\mathbf{10^{-4} - 10^{-1}}$ for charm and $\sim\mathbf{10^{-3} - 10^{-1}}$ for beauty production.

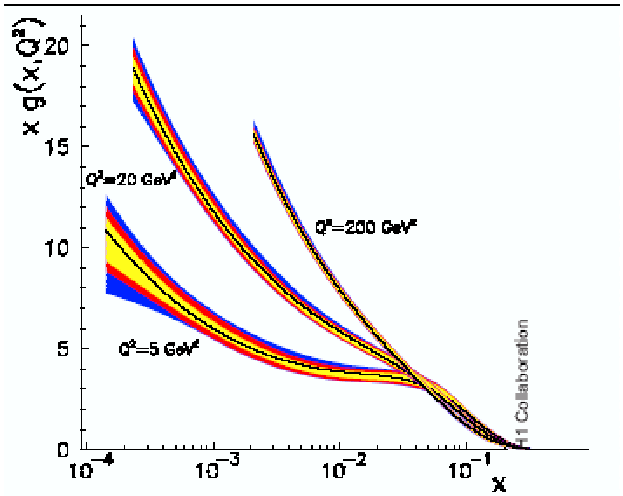

Figure 3.15: *Gluon density in the proton as a function of the proton momentum fraction x carried by the gluon for three different values of the photon virtuality Q2, as determined from the scaling violations of the inclusive structure function F_2.*

Perturbative QCD calculations of heavy flavour hadron production cross sections factorise the process into four pieces as depicted in figure (3.16) and expressed by the following convolution:

$$\boldsymbol{\sigma} = \boldsymbol{p}Structure \otimes \boldsymbol{\gamma}^{*}Structure \otimes hardME \otimes Fragmentation$$

Here 'p Structure' denotes the parton densities in the proton, 'γ^* Structure the parton densities in the resolved photon, 'hard ME' the calculable hard scattering cross section and 'Fragmentation' the fragmentation of the quarks into observable hadrons. For the direct photon gluon fusion process shown in figure 3.12(left plot), there is no photon structure term and the heavy quark cross section (before fragmentation) can be written in the form

$$\sigma_{dir}^{\gamma P}(P_\gamma, P_P) = \int dx f_g^p\,(x, \mu_F)\hat{\sigma}_{\gamma j}(P_\gamma, P_p, \alpha_s(\mu_R), \mu_R, \mu_F)\,. \qquad (3.42)$$

Here $f_g^p(x, \mu_F)$ denotes the proton gluon density as a function of the proton momentum fraction x and the factorisation scale μ_F. Gluon radiations with kinematic scales below μ_F are absorbed in the proton gluon density, while those with harder scales are attributed to the hard scattering (see figure 3.16).

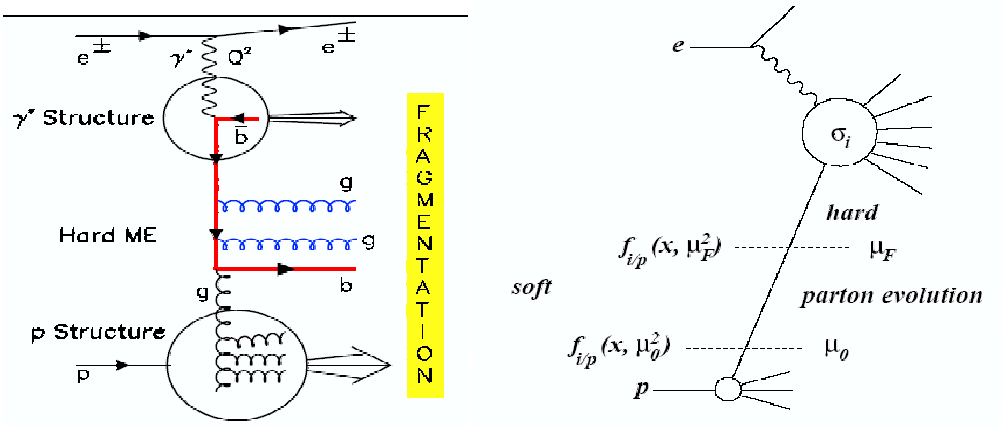

Figure 3.16: *Factorisation of heavy flavour production in QCD in proton structure, photon structure, hard matrix element and fragmentation (left).Illustration of factorisation principle (right).*

The dependence of the gluon density on the factorisation scale can be calculated using the DGLAP [32] [33] evolution equations.

$\hat{\sigma}_{\gamma j}(P_\gamma, P_p, \alpha_s(\mu_R), \mu_R, \mu_F)$ is the hard partonic cross section of a photon and a gluon that depends on their momenta, on the strong coupling constant α_s, on the renormalisation scale μ_r[10] at which α_s is evaluated and on the factorisation scale, μ_F. Figure (3.17 a) shows a leading order $\mathcal{O}(\alpha_s)$ process and 3.17b,c,d, higher order

[10] μ_r, the renormalisation scale is introduced to remove the ultra violet divergences which occur when virtual corrections are taken into account in the calculation of the matrix element. These divergences are absorbed into the running of the strong coupling constant $\alpha_s(\mu_r^2)$ (see Appendix C).

$\mathcal{O}(\alpha_s^3)$ processes. Beyond leading order the separation into direct and resolved photon processes is ambiguous.

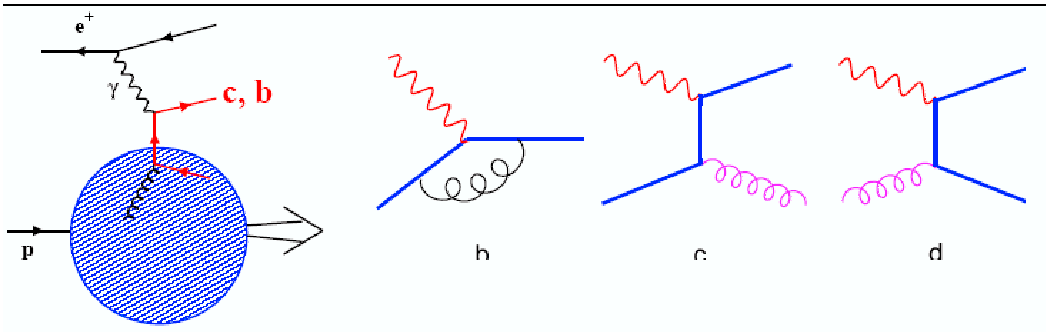

Figure 3.17: *Leading diagrams for heavy quark production in the massless scheme at leading order (a) and next-to-leading order (b-d).*

Besides the heavy quark masses, there can be two other relevant hard scales available in the heavy quark production process, the virtuality Q^2 of the exchanged photon and the transverse momenta P_T of the outgoing heavy quarks, as depicted in figure 3.18. This leads to the so called multi-hard scale problem in QCD, which is related to terms in the perturbative series of the form

$$\sim[\alpha_s \ln (P_t^2/m_h^2)]^n \qquad \text{or} \qquad \sim[\alpha_s \ln (Q^2/m_h^2)]^n \tag{3.43}$$

with h=c,b. Such terms appear at all orders n and represent collinear gluon radiations from the heavy quark lines. The terms can be large for $Q^2 \gg m_h$ or $P_T^2 \gg m_h$ and hence can spoil the convergence of the perturbative series.

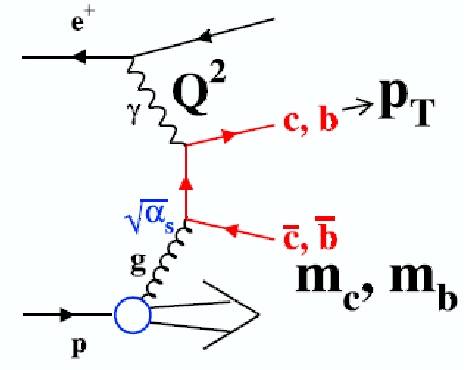

Figure 3.18: *Possible hard scales in the photon gluon fusion process.*

Different schemes to calculate heavy quark production processes have been developed in the framework of collinear factorisation that are expected to be valid in different kinematic regimes:

- Massless Scheme: In calculations for processes with light quarks, the mass of the light quarks is assumed to be zero. The quarks are treated as active partons in the proton, i.e. a density distribution for the quarks in the proton is used to describe the non-perturbative part of the calculation. The perturbative series is expanded using a scale-parameter μ as given by the photon virtuality Q^2 or jet momentum P_T. Perturbative calculations are expected to converge for $\mu \gtrsim \Lambda_{QCD}$. Due to the heaviness of the quark mass m_q, this approach does not work for heavy quarks except in the extreme limit $\mu \gg m_q$, in which the heavy quarks can be treated as massless. In this 'massless' scheme, at the leading order (LO), the quark parton model (QPM, see figure 3.17a) process is dominant contribution.

  At the next-to-leading order (NLO), virtual corrections are included (figure 3.17b) and the QCD Compton ($\gamma q \rightarrow qg$, figure 3.17c) and photon gluon fusion (figure 3.17d) processes also contribute. The massless approach is often referred to as the Zero Mass Variable Flavour Number Scheme (ZM-VFNS) [39] [40]. In this approach the heavy quarks are treated as infinitely massive below some scale $\mu^2 \sim m_q$ and massless above this threshold.

  In this scheme the heavy quarks can also be absorbed into the proton structure and treated as massless sea quarks like the light quarks (u, d and s). This treatment allows resummation of the terms in equation 3.43 to all orders, i.e. the collinear radiations are absorbed into the 'heavy quark' proton density function, using the DGLAP equations just as is usually done for the light quarks. This scheme is expected to work well for $Q^2, P_T^2 \gg m_h^2$.

- Massive Scheme: At values of $\mu^2 \sim M^2$, the 'massive' scheme [41]- [43], in which the heavy flavour partons are treated as massive quarks is more appropriate. The heavy quarks are only produced perturbatively as shown in the diagrams in figure 3.19. The higher order terms in equation 3.43 beyond

NLO are simply ignored. This scheme is expected to work well for the kinematic region $Q^2, P_T^2 \sim m_h^2$. In the massive scheme the dominant leading order (LO) process is photon gluon fusion (PGF, figure 3.19 a) and NLO diagrams are of order α_s^2(figure 3.19 b-c). The scheme is often referred to as the Fixed Flavour Number Scheme (FFNS). As μ^2 becomes large compared to M^2, the FFNS approach is unreliable due to large logarithms in $ln\,(\mu^2/M^2)$ in the perturbative series. Generator programs in this scheme which are applicable to HERA physics (FMNR [44] , HVQDIS [45]) are available to next-to-leading order [44] [45]. The fixed order massive scheme is also used in various Monte Carlo event generator programs which implement leading order matrix elements and parton showers to simulate higher order effects. A brief description of these programs is given at the end of this chapter.

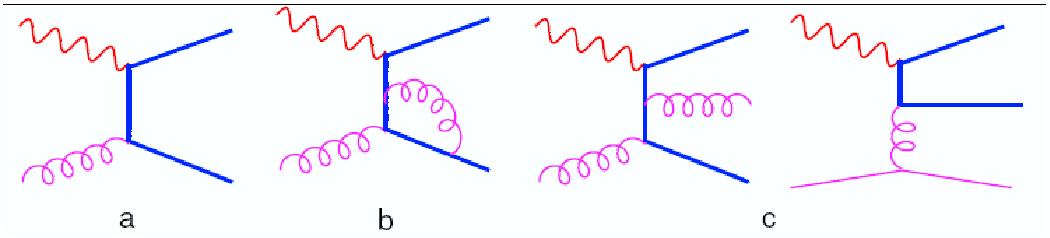

Figure 3.19:*Leading diagrams for heavy quark production in the massive scheme at leading order (a) and next-to-leading order (b-d).*

- Mixed Schemes: In order to provide reliable pQCD predictions for the description of heavy quark production over the whole range in μ^2, composite schemes which provide a smooth transition from the massive description at $\mu^2 \sim M^2$ to massless behaviour at $\mu^2 \gg M^2$ have been developed. These composite schemes are commonly referred to as variable flavour number schemes (VFNS). The schemes (i.e. VFNS) converge at small (large) photon virtualities Q^2 to the massive (massless) scheme. For intermediate Q^2 an interpolation is performed. The general idea is embodied in the structure:

$$[\text{QPM term}] - [\text{asymptotic subtraction term}] + [\text{PGF term}] \qquad (3.44)$$

An illustration is shown in figure 3.20 for the case of charm production. The subtraction term is the key to the understanding of the interpolation procedure. In this term the charm quark is close to mass-shell and collinear to the gluon and hadron

momenta. For $Q^2 \ll m_c^2$ the subtraction term becomes equal to the QPM term and the remaining contribution is from the PGF diagram. On the contrary for $Q^2 \gg m_c^2$ the subtraction term cancels the PGF term and QPM term is recovered. There are various approaches on how to deal in detail with the subtraction in the intermediate Q^2 region. For a full discussion see [46] [47].

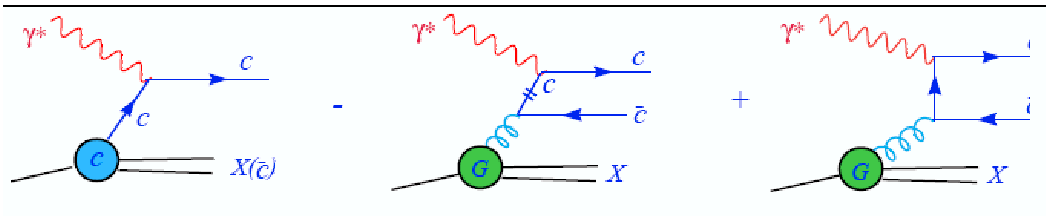

Figure 3.20: *Leading order diagrams for charm production in DIS in the variable flavour number scheme: On the left the QPM diagram is shown, on the right the PGF diagram and the middle the 'subtraction diagram'.*

3.4 Hadronisation

The life-time of charm and beauty quarks is long enough to allow them to form hadrons which can be experimentally observed. The transition from partons to colourless hadrons is called hadronisation. The hadronisation process cannot be described using perturbative QCD but phenomenological models have to be applied. Fragmentation functions are used to parameterise the transfer of a quark's energy to a given meson.The starting point is the partons from the perturbatively calculable final state, e.g. the parton configuration after the final state parton showering in the leading order calculations. It is assumed that the full process can be factorised into a hard, perturbatively calculable and soft, non-perturbative part (cf. figure 3.16-right) and that the hadronisation is independent of the hard scattering process, i.e. the models and their parameters measured at one experiment, e.g. at the e^+e^- collider LEP, can be used at any other experiment.

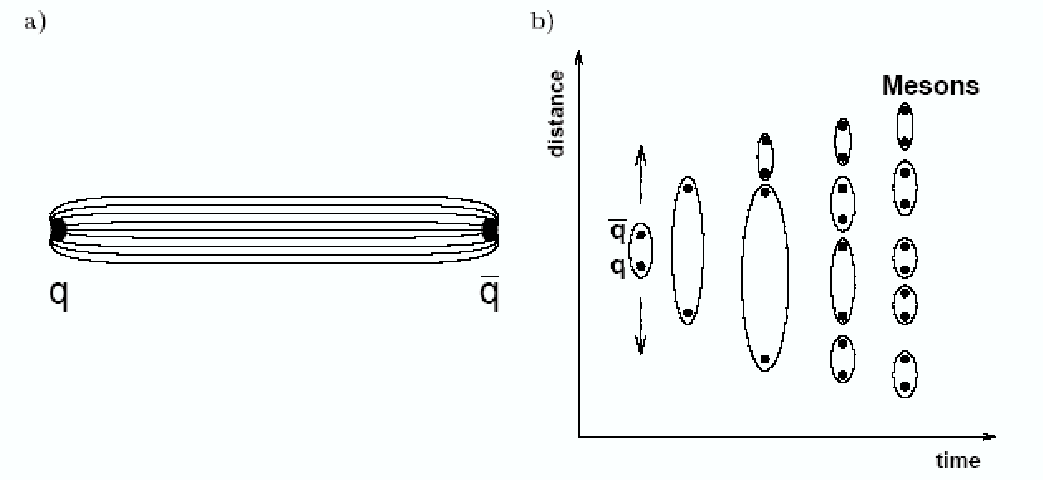

Figure 3.21: *Illustration of the Lund string hadronisation model. a) The tube-like colour field between a quark and an anti-quark according to the QCD potential(cf. equation 3.44). b) Formation of colourless hadrons according to the Lund fragmentation model.*

One of the most successful hadronisation models is the Lund string model [48]. The colour field between two quarks is squeezed into a tube-like region, a colour string, as depicted in figure 3.21 a). The colour field is given by the QCD potential

$$V(r) = -\frac{4\alpha_s}{3r} + \kappa r \,. \tag{3.45}$$

Here the second term κr accounts for the QCD colour confinement which causes the colour interaction to become stronger when the quarks separate. Since κ is of the order 1 GeV/fm, the second term dominates at large distances r, leading to the tube-like shape of the colour field. The string breaks up if the energy is large enough to produce a $q\bar{q}$ pair which then may produce a cascade of additional quark pairs until the energy is exhausted and bound quark states are produced. This process is illustrated in figure 3.21 b). Within this model baryons are created via the production of diquark pairs $qq\bar{q}\bar{q}$.

While the transverse momentum spectrum of the produced hadrons is assumed to be Gaussian, the longitudinal momentum is derived from fragmentation functions *f (z)*. The fragmentation functions describe the probability for a Hadron *H*, which originates from a quark *Q*, to carry the fraction $z = (E + p_{\parallel})_H/(E + p)_Q$ of the quark's longitudinal momentum. Different fragmentation functions can be used within the Lund string model. In the following, two of the fragmentation functions are discussed.

The Lund fragmentation function is defined as follows:

$$D_Q^H(z) = N\frac{(1-z)^a}{z}\exp\left[\frac{-bm_\perp^2}{z}\right] \tag{3.46}$$

Where $m_\perp^2 = E^2 - p_z^2$ is the transverse mass of the hadron H and a and b are parameters which have to be adjusted to data.

For heavy flavour production the Peterson fragmentation function $D_Q^H(z)$ [49] is preferentially used, since it provides a harder fragmentation which is needed to describe charm and beauty data:

$$D_Q^H(z) = \frac{N}{z}\left(1 - \frac{1}{z} - \frac{\epsilon_Q}{1-z}\right)^{-2} \tag{3.47}$$

The Peterson parameter ϵ_Q has to be adjusted to the data. It scales between flavours like $\epsilon_Q \propto \frac{1}{m_Q}$. At leading order a common choice for the parameterϵ_Q is $\epsilon_c \approx 0.058$ for charm and $\epsilon_b \approx 0.0069$ for beauty hadrons. According to [50] the common choice at next-to-leading order is $\epsilon_c \approx 0.035$ and $\epsilon_b \approx 0.0033$. In figure 3.22 the Peterson fragmentation functions for the latter case are depicted. The fragmentation is harder for beauty quarks due to their larger mass. At next-to-leading order the fragmentation parameters are smaller because the possibility of gluon radiation is already included in the matrix element.

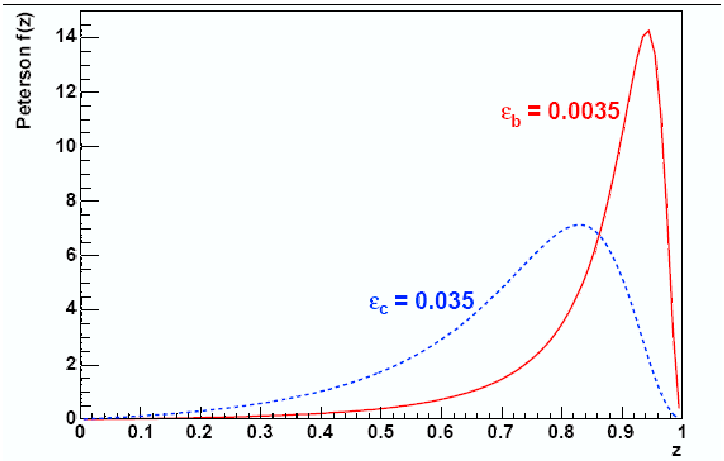

Figure 3.22: *Peterson fragmentation functions for charm and beauty (next-to-leading order parameters ϵ_c and ϵ_b are used).*

3.5 Monte Carlo Event Generators

Monte Carlo event generators are used in high energy physics to model events as they would be observed by a perfect detector. For this purpose a reasonable modelling of the underlying physics is needed at the generator level, i.e. before the detector simulation. In the available programs the parton level is generated using leading order pQCD matrix elements. Higher orders are approximated using parton showers (PS) radiated from the initial and final state partons. These parton showers are generated in most programs according to the DGLAP parton evolution scheme. Since the process of event generation is too complex to be performed in one go, it is instead subdivided into several parts. This is illustrated in figure 3.23 for the example of a photon-gluon fusion event at HERA and a leading order plus parton shower event generator. The emission of virtual photons by the electron can be described using QED. In the photoproduction regime the photon flux $f_{\gamma/e}(y, Q^2)$ is given by the Weizsäcker-Williams approximation [51]. The proton parton density function defines the flavour and the energy of the particle which takes part in the interaction from the proton side. To obtain the parton density function at the appropriate scale, parton evolution schemes, e.g. DGLAP or CCFM, are used. The parton from the proton starts off a sequence of branching, such as, $g \longrightarrow gg$, leading to an initial state parton shower. The photon and a parton from the initial state parton shower enter the $2 \rightarrow 2$ hard process. The matrix element (ME) for the process is calculated in leading order. The outgoing partons from the hard process are subject to final state parton showers. The main properties of an event are determined by the LO matrix element and the parton showers effectively approximate higher order effects. The outgoing partons from the parton showers enter the hadronisation step, which is based on phenomenological models.

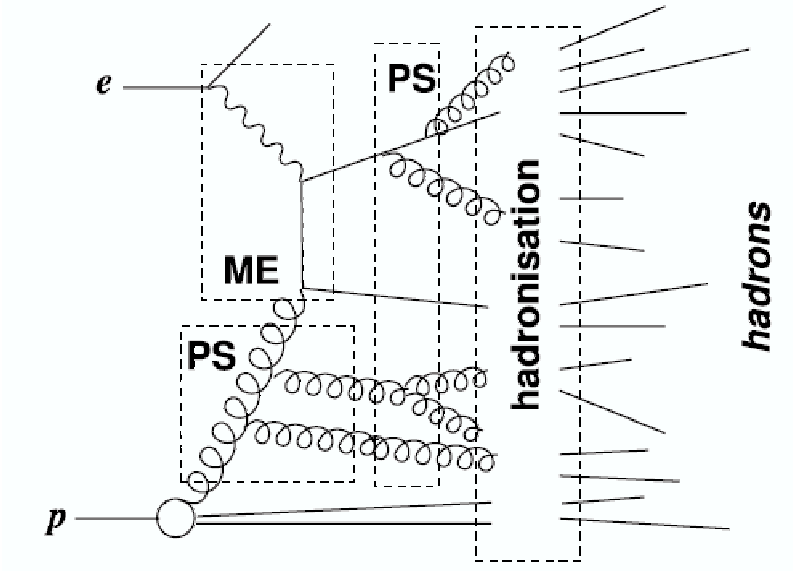

Figure 3.23: *Principle layout of an event generator with initial and final state parton shower (PS), leading order matrix element (ME) and hadronisation.*

In this analysis Monte Carlo program RAPGAP [51] is used to generate DIS events for the processes $ep \longrightarrow eb\bar{b}X$, $ep \longrightarrow ec\bar{c}X$ and $ep \longrightarrow eqX$ where q is a light quark of flavour u, d or s. The Monte Carlo program CASCADE [52] is also used to produce b and c events. RAPGAP combines $O(\alpha_s)$ matrix elements with higher order QCD effects modelled by the emission of parton showers. The heavy flavour event samples are generated according to the massive photon gluon fusion (PGF) matrix element with the mass of the c and b quarks set to $m_c = 1.5$ GeV and $m_b = 4.75$ GeV respectively. The DIS cross section is calculated using the leading order (LO) 3-flavour parton distribution functions (PDFs) from [39]. CASCADE is an implementation of the CCFM [36] evolution equation and uses off-shell matrix elements convoluted with k_T unintegrated proton parton distributions.

The partonic system from *uds*, c and b processes is then fragmented according to the LUND string model implemented within the PYTHIA program [53]. The c and b quarks are hadronised according to Bowler fragmentation function [80]. The HERACLES program [54] calculates single photon radiative emissions off the lepton line to provide virtual and electroweak corrections.

The samples of events generated for *uds*, *c* and *b* processes are passed through a detailed simulation of the detector response based on the GEANT3 program [55], and through the same reconstruction software as is used for the data.

Chapter 4

"He that would perfect his work
must first sharpen his tools."
Confucius

Event Selection

In this chapter the inclusive DIS jet sample is presented which is the basis for the measurement of the charm and beauty cross sections. The chapter starts with the data sample used and the selection criteria applied. The DIS event selections are discussed which continues with trigger selection, DIS control plots and track reconstruction, the chapter concludes with a discussion on calibration.

4.1 Data set

The data used in this thesis were recorded with the H1 detector in 2006 and 2007 when the CST was fully operational and corresponds to an integrated luminosity of 188.6 pb^{-1}.The data chosen for this analysis are composed of electron-proton collisions (53.4 pb^{-1}) and the positron-proton collisions (135.2 pb^{-1}) .

Each HERA fill of colliding protons and electrons is recorded by H1 in a series of data taking runs. Background conditions and other experimental factors are not constant throughout each run and so only runs that occur under acceptable conditions are analysed in this thesis. Since the detector conditions may vary during runs and luminosity fills, therefore, a *good run* selection is performed on all the recorded data

used in this analysis. This selection is based mainly on high voltage (HV) conditions of certain detectors essential for this analysis. The central tracker HV must be on, namely the central jet chambers CJC1/2, and central proportional chambers COP/CIP, the LAr, CST must also be on, as well as the ToF system and the Lumi system.

4.2 Kinematics

The kinematics of an event may be defined using information from the scattered electron, the hadronic system, or a combination of the two. These methods of reconstruction of the kinematic variables that define an event differ in resolutions for each variable due to different precision with which each component quantity can be measured.

Different methods that are used to reconstruct the kinematic variables are (for detail refer to Appendix B): the Electron Method ([56]); the Double Angle Method; the Sigma Method and the Electron Sigma Method ([57]) .The Electron Sigma Method is employed in this analysis to reconstruct the kinematic variables[1] of the events. The Electron Sigma Method combines the excellent Q^2 resolution of the Electron Method with the precision x determination from the Sigma Method. It is defined as follows:

$$Q^2_{e\Sigma} = Q^2_e \qquad x_{e\Sigma} = x_\Sigma \qquad y_{e\Sigma} = \frac{Q^2}{s x_{e\Sigma}} \tag{4.1}$$

The event kinematics Q^2, and inelasticity variable y, are reconstructed using the above method whereas the Bjorken scaling variable x is obtained from $x = {Q^2}/{sy}$.

4.3 DIS and Jet Event Selection

- The events are selected by requiring a compact electromagnetic cluster in either the LAr or SPACAL calorimeters.

[1] For a detailed description of the kinematic variables, Q^2, y and x, see section 3.1 `Kinematics of *ep* Scattering` of the Theory chapter in this thesis.

- The Electron Cluster Radius (ECRA) was required to be less than 4 cm. An electron will produce a cluster in electromagnetic calorimeter over a localised region, unlike hadrons for which the cluster is generally more spread out. Thus requiring an ECRA to be less than 4 cm,is minimising the probability that a hadron from other processes (mainly photoproduction) fakes an electron.

- The z position of the interaction vertex was reconstructed by one or more charged tracks in the tracking detector and it was required to be within $\pm\, 20\ cm$ of the centre of the detector to match the acceptance of the CST.

- In order to suppress the photoproduction events, $\sum_i E_i - P_{z,i}$ was required to be greater than $35\ \mathrm{GeV}$. Here E_i and $P_{z,i}$ denote the energy and longitudinal momentum components of a particle and the sum is over all final state particles including the scattered electron and the hadronic final state (HFS). The HFS particles are reconstructed using a combination of tracks and calorimeter deposits in an energy flow algorithm that avoids double counting ([58]).

- To ensure sound event reconstruction, apart from HV sub-detector components (i.e. CJC1/2, CIP, COP) and ToF, LAr, SPACAL and Lumi system which were required to be fully operational, the CST (Central Silicon Tracker) was also required to be operational during the data taking run.

- In order to have good acceptance in the SPACAL and to ensure that HFS has a significant transverse momentum, events are selected in the range $4.5 < Q^2 < 1585\ \mathrm{GeV}^2$. The analysis is restricted to $0.07 < y_e < 0.625$. The range of *y* was chosen to ensure that the direction of the quark which is struck by the virtual exchanged photon is mostly in the CST angular range (the lower *y* cut) and to reduce photoproduction background (the upper *y* cut).

- Fiducial cuts were made to avoid cracks in the detector acceptance (in the ϕ_e and Z_e directions) where the efficiency of both the trigger and the electron

finder is significantly less than 100%. These regions occur when ϕ_e is within 2° of the LAr octant edges and at $15.0 < Z_e < 25.0$ cm. Due to high rates an inner SPACAL `s2 box` cut has been applied as follows $(-20 < x_e < 19 \;\&\&\; -10 < y_e < 19) \parallel (-8 < x_e < 9 \;\&\&\; -19 < y_e < -11) \parallel (10 < x_e < 16 \;\&\& -10 < y_e < 9)$ cm. Here ϕ_e, Ze, x_e and y_e denote the impact position of the electron on the surface of the calorimeter.

- Jets with minimum P_T of 1.5 GeV, in the angular range $15° < \theta < 155°$ are reconstructed using the invariant K_T algorithm [62] in the laboratory frame using all reconstructed HFS particles.

4.4 Trigger Selection

The main objective of the trigger system is to give a fast decision for the acquisition of the interesting *ep* events while sorting out the background events. More information on triggers can be found in section 2.6 of the detector chapter of this thesis.

At the first level of the H1 trigger system a classification of events into physical classes is done by combining different trigger elements into conditions called subtriggers. An optimal use of the available band width of the read-out is achieved by an autoprescale scheme [74].

The prescale strategy sets priorities to the different physics classes. According to these priorities events are rejected by the Level 1 trigger system. The rejection is steered by prescale factors assigned to the different subtriggers. A prescale factor *N* means that only one out of *N* triggered events is preserved. The production rates of all processes decrease together with the luminosity during a HERA fill. Therefore more band width becomes available for physical classes with low priorities and their prescale factors are successively reduced.

The autoprescale scheme has the consequence that the effectively taken luminosity depends on the subtrigger and its mean prescale factor. The integrated luminosity is needed for the cross section measurement and therefore the analysis is constrained to events accepted by specific subtrigger.

The triggers used in the analysis require a SPACAL energy deposit in association with a loose track requirement. Although these triggers are ≈100% efficient which

reduces systematic uncertainty on tracking efficiency, albeit not all events could be recorded, due to the large rate for low Q^2 events.

In this analysis subtrigger **S**3 (an inclusive trigger) which requires an energy deposit in the electromagnetic SPACAL, in conjunction with subtrigger **S**61(non-inclusive trigger), which requires a loose track association, are used.

The subtrigger 61 (ST 61) is designed for selecting possible heavy flavour events in the analysed Q^2 range. The Level 1 condition of ST61 is given in table 4.1.

ST 61 =	(SCPLe_IET>2 || SCPLe_IET_Cent_3) && DCRPh_THig && zVtx_sig && (d:0) && (v:8) && (f:0)
(d:0) =	DCRPh_NL_many && DCRPh_NH_many && DCRPh_PL_many && DCRPh_PH_many
(v:8) =	! SPCLh_AToF_E_1 && ! SPCLh_ToF_E_2 && ! VETO_inner_BG && ! VETO_Outer_BG && ! VLQToF_BG
(f:0) =	(FToF_IA || FIT_IA) || (! FToF_BG && ! FIT_BG)

Table 4.1: *The trigger element composition of ST 61. The logical operators used in the definition are "&&" for "and", "||" for "or" and "!" for a logical "not".*

The main trigger elements of ST 61 are

- (SCPLe_IET>2 | | SCPLe_IET_Cent_3) requires a cluster with more than 6 GeV energy deposition in the SpaCal setting off the Inclusive Electron Trigger(IET),
- DCRP_THig demands a track with transverse momentum above 900 MeV identified by the DCRhi drift chamber trigger and
- zVtx_sig ask for a significant entry in the *zVtx* histogram of the proportional chambers.

The global options (d:0), (v:8) and (f:0) are included in several subtriggers and are designed to suppress noisy CJC events and to reject background events from outside the interaction time window which are identified by time of flight (ToF) and VETO systems.

The subtrigger S3 requires only a certain energy deposit in the electromagnetic SpaCal. The requirement for the subtrigger S3 can be summaries as;

- SPCLe_IET >2 which requires a cluster with more than 10 GeV energy deposition in the SpaCal outer region, with no track requirement but with Level 2 requirement radius of >30cm.

All events that are triggered by the unprescaled subtriggers S3‖S61 (i.e. S3 OR S61), are taken and then these are assigned a weight of 1. Events are also taken that fail both these subtriggers but pass one of the inclusive subtriggers S0‖S1‖ S2 , which are weighted according to

$$\mathcal{W} = \frac{\sum_{i=1}^{Nrun} \mathcal{L}_i \mathcal{W}_i}{\sum_{i=1}^{Nrun} \mathcal{L}_i}, \qquad (4.1)$$

$$\frac{1}{\mathcal{W}_i} = 1 - \prod_{j=1}^{Ntrig} (1 - \frac{1}{P_j})$$

where *Nrun* is the number of runs each with integrated luminosity $\mathcal{L}_i$ and P_j is the prescale of the j^{th} trigger for run i. A value of $\mathcal{W} = 1.33$ ($\mathcal{W} = 1.17$) for the $e^- p$ ($e^+ p$) data was obtained. This method means that a trigger efficiency of $\approx 100\%$ is kept, albeit with a slightly increase in statistical error on the data, in fact the average weight for all events is smaller than 1.02.

4.5 DIS Control Plots

The following distributions demonstrate the effectiveness of the DIS selection criteria described above. All distributions are well described by the model RAPGAP. This indicates that both the physics and the geometry of the H1 detector are understood and well described by Monte Carlo. Figure 4.1 shows the kinematic variables Q^2 and *y*, which represent the virtuality of the exchanged vector boson in the DIS events and the relative energy of the electron transferred to the proton respectively. This work is concerned with the values of Q^2 greater than 4.5 GeV^2. The accurate reconstruction of the neutral current event topology requires the presence of a high energy electron in the final state. For this reason, and because a photoproduction event can be misidentified as a NC DIS event due to a hadronic energy deposit near the forward beam pipe and being incorrectly flagged as an electron, events like these will have a high value of *y*, therefore, events with values of *y* above 0.625 are not considered.

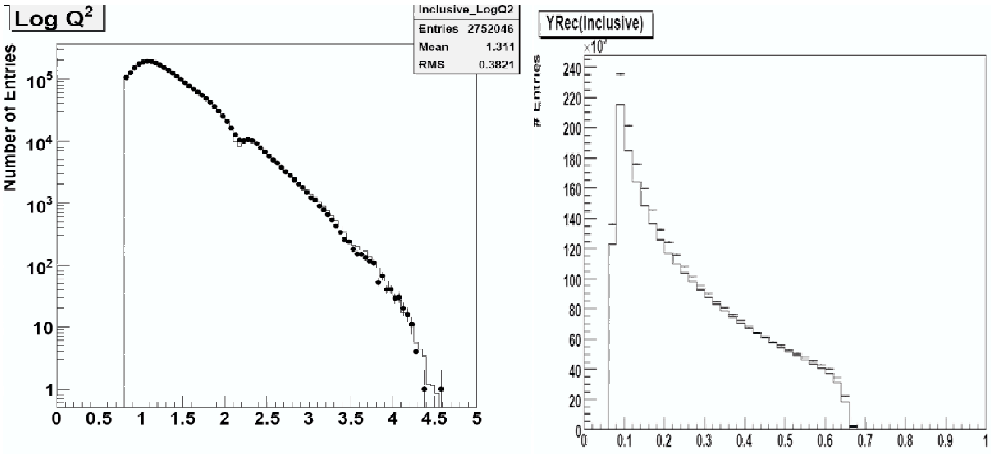

Figure 4.1: *Control distributions after selection cuts and trigger selection for the values of* o*f* $log_{10}Q^2$ *(left) and inelasticity*, y*(right).*

Figure 4.2 shows the energy spectrum and polar angle for the scattered electron, E′, in the DIS event sample. The energy spectrum demonstrates the inelastic nature of the collisions concerned. The spectrum of an elastic collision is expected to be a Gaussian distributed around the initial energy of the projectile (in this case a 27.6 GeV electron). The θ distribution shows a peak due to the kinematic range considered in this work and also because of limitations in detector acceptance. The virtuality requirement for events considered in this work ensures that the electron is scattered through an angle smaller than 90°-towards its incident direction so that it can be detected in LAr or SPACAL.

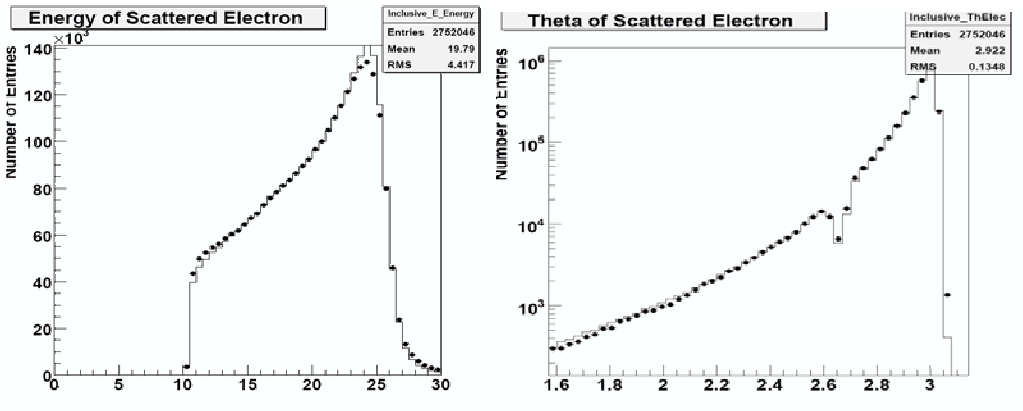

Figure 4.2: *The scattered electron energy spectrum (left) and polar angle θ.(right) for the DIS event sample.*

Figure 4.3 show the nominal z position of the primary interaction vertex and the Björken x distribution. The z vertex distribution is as expected for inelastic ep colloions- that is, a Gaussian distribution about the nominal interaction point. The model used is reweighted in this distribution so that a good description is assured.

The Björken x distribution shows the kinematic reach of this work, with values as low as low as 10^{-4} being observed. Almost the whole distribution occurs below the valence region ($\log(x_{Bj})\sim -0.48$) indicating that, in this work, the incident electron interacts with either a sea quark or gluon (via boson-gluon fusion) within the target proton more than 99% of the time.

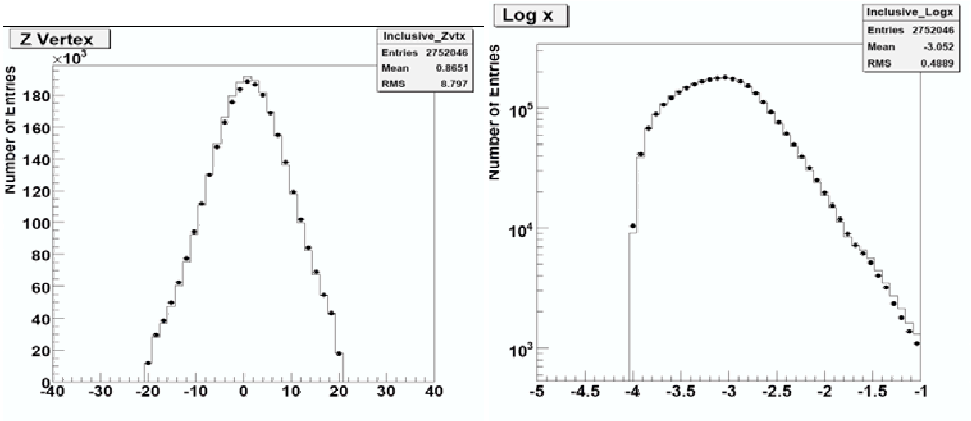

Figure 4.3: *The Z position of the primary interaction vertex (left) and* x_{Bj}*.(right) for the DIS event sample.*

Figure 4.4 shows the variable $E - P_z$. For a DIS collision, the sum of all $E - P_z$ is expected to peak at $2E_e$, assuming that all energy is correctly measured, as the beam proton remnant can be neglected due to its small forward angle. Deviations from this value occur due to particles escaping down the backward beampipe, photons radiated collinearly to the initial state electron and measurement inaccuracies. The sum of $E - P_z$ is reduced by twice the energy lost in the backward direction. This means that the cut imposed ($E - P_z > 35\ GeV$) causes the total effect of such losses to be no greater than 10GeV per events. The distribution can be seen to peak at 55GeV as expected, with no more than 2% of events having the maximum allowed backward energy losses. This cut also helps remove photoproduction events because, for an event in which the scattered electron escapes undetected, the value of $E - P_z$ is reduced by twice the energy of the scattered electron, E′.

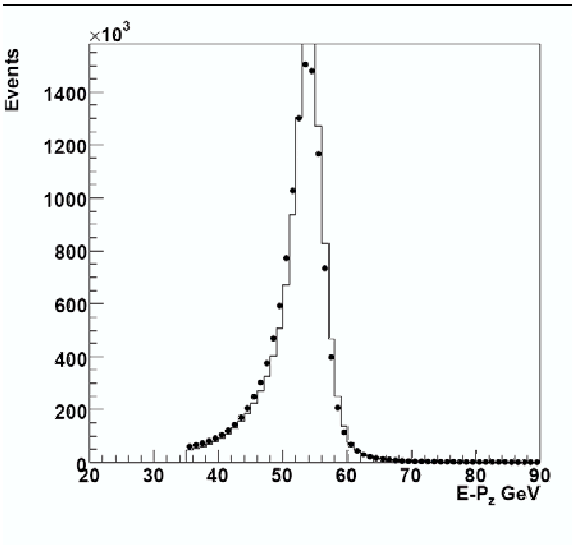

Figure 4.4: *The distribution of the variable $E - P_z$ for the DIS event sample.*

Figure 4.5 shows the influence of some of the geometric features of the H1 detector. The azimuthal angular distribution for the scattered electron shows the effect caused by SPACAL box cut and the cell structure of the SPACAL.

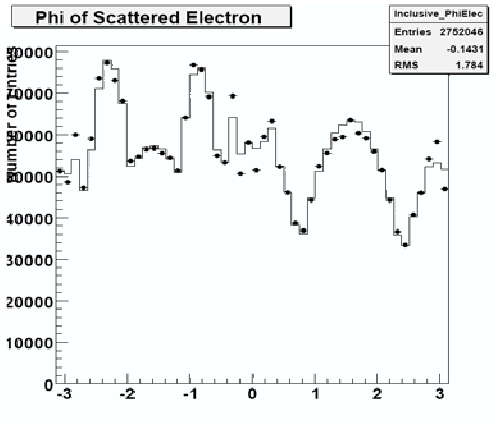

Figure 4.5: *The distribution of ϕ for the DIS event sample*

Figure 4.6 shows similar plots as figures4.1-4.5 for positron.

In these plots the black curve represents the sum of Monte Carlo events (i.e. RAPGAP), that is the sum of light and heavy flavour events, and the black solid dots are the data. As it can be seen from the control plots the data are very well described by the RAPGAP Monte Carlo program. After applying the DIS cuts detailed above the total number of events were 2.5 million (2.7 million) for e^- (e^+).

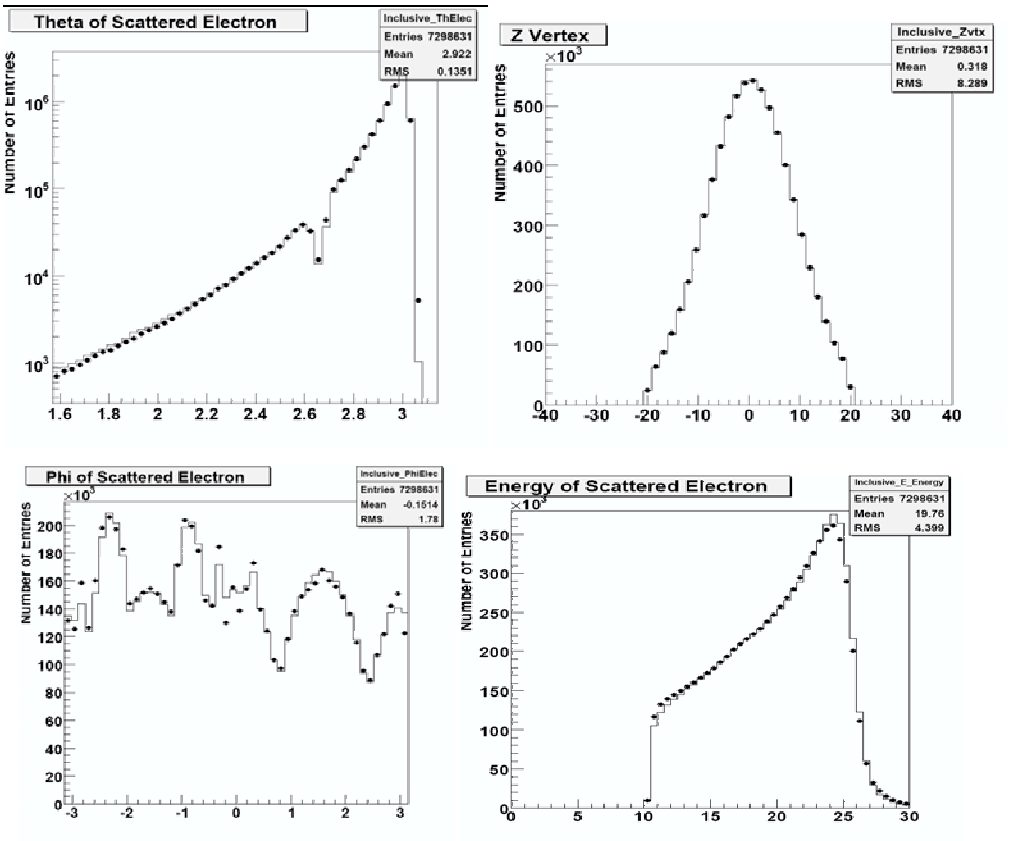

Figure 4.6: *Control distributions after selection cuts and trigger selection for the values of* of $log_{10}Q^2$, $log_{10}x$, *energy of the scattered positron E,* θ *and* ϕ *angles of the scattered positron and the z coordinate of the vertex position.*

4.6 Track Selection

The association of CST hits to the CJC tracks to determine the combined CJC-CST track parameters is crucial for determination of the decay time, 'the lifetime tag'. First, the CJC tracks are reconstructed. The reconstruction algorithm determines the track parameters $\bar{T} = (\kappa, \phi_0, d_{ca})$ (for details refer to the section 5.2, Track Reconstruction).For the track fit a circular trajectory is assumed.

The impact parameter of the track is defined as the transverse distance of closest approach (DCA) of the track to the primary vertex point. The primary event vertex in $r\phi$ is reconstructed from all tracks (with or without CST hits) and the position and spread of the beam interaction region [60]. The DCA is only determined for tracks which fulfil the following conditions:

- Tracks are measured in the CTD and have at least two CST hits linked (referred to as *CST tracks*).
- The link probability of the CST hits with the CST tracks should be > 0.001.
- Only CST tracks with transverse momentum $P_T > 0.3\text{GeV}$ are included in the DCA and related distributions that are used to separate the different quark flavours.
- The radius of the initial track point in the CJC is required to be $R_{start} < 50cm$.
- The length of the track in the CJC should be more than 10cm.
- The CST hits should be within a z region of $-18 < z_{CST} < 18cm$, where z_{CST} is measured at the outer surface of the CST.

The distributions of P_T and θ of all CST tracks are shown in Fig (4.7). The data are well described by Monte Carlo.

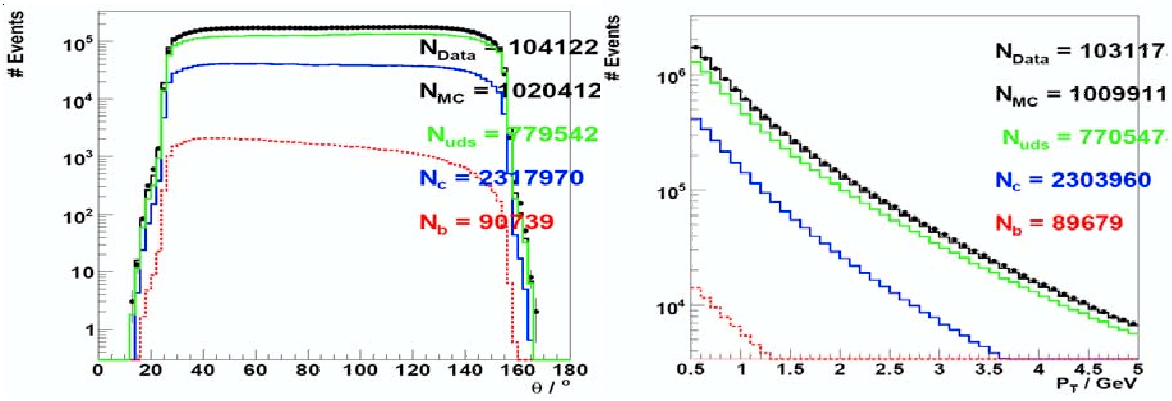

Figure 4.7: *The transverse momentum P_T (right figure) and the angle θ (left figure) of all CST tracks. The contributions from various quark flavours are shown after applying the scale factors obtained from the fit to the subtracted significance distributions of the data (cf. Chapter 6).*

4.7 Calibration

The calibration of the electromagnetic and hadronic energy scales of the the LAr is performed as described in [61], an overview of which is presented here. The scattered electron energy, E', from NC DIS events is measured by the LAr and SPACAL and also reconstructed using the Double Angle method (see Appendix B), which is independent of the energy of the electron or the HFS.

The fraction $E':E_{DA}$ was taken and calibration constants introduced to bring this value into unity for both data and simulated events. These calibration constants are a function of z and Φ, in the LAr and for each cell in the SpaCal. The areas of low efficiency mentioned above (Fiducial cuts) were excluded from the study. The final calibration constants are such that the double ratio of $E':E_{DA}$ to the value in simulated events is unity within 0.7%-3%, depending upon the z position.

The difference between data and Monte Carlo plot, which is conservatively estimated at 4% is the error taken for the HFS and the jets.

Figure 4.8 shows the ratio of the transverse momentum, P_T, as measured from the hadronic final state and from the electron. The P_T balance is peaked around one and demonstrates that the overall hadronic calibration is sound.

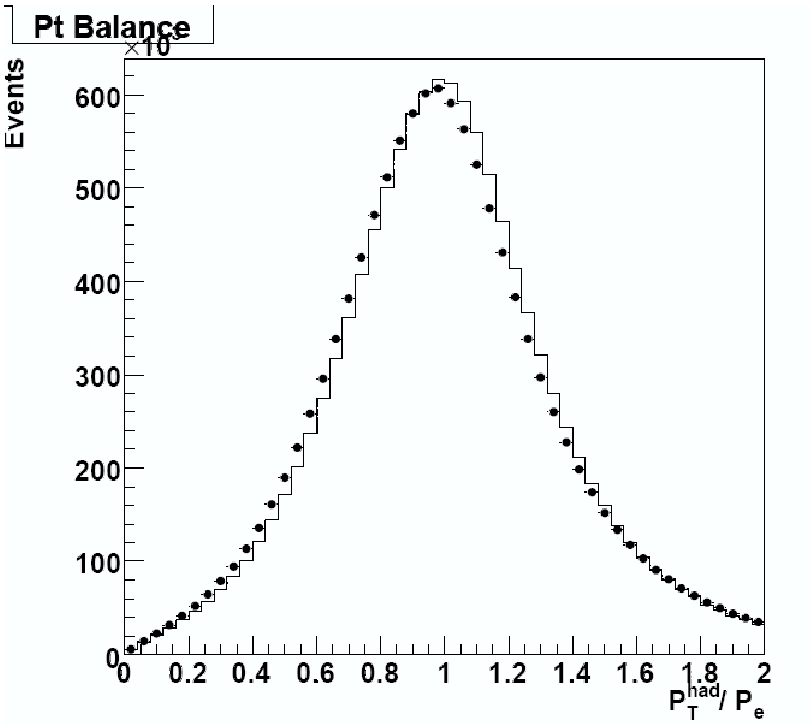

Figure 4.8: *The distribution of the P_T balance.*

4.8 Rejection of Non-*ep* Background

Non-ep background may arise from a number of sources, the largest contributions being cosmic ray and beam-halo events, which produce muons. In order to minimise this background additional measures are required. The requirement of a primary vertex within 20 cm of the nominal interaction point reduces this background significantly, as most muons

from background sources will not have passed through the nominal interaction point. Background is further reduced by requiring the time of the event, measured by CJC, to be consistent with the time of the bunch-crossings. Finally a set of topological background filters [87] is used, reducing the background to a negligible rate.

‘

Chapter 5

We shall not cease from exploration
And the end of all our exploring
Will be to arrive where we started
And know the place for the first time.
-T.S.Eliot

Event Reconstruction

The main goal of this analysis is to measure the cross section of charm and beauty jets. The techniques and methods that have been used in order to extract the results are discussed in this chapter. The chapter starts by describing the exploitation of the long life-time of the charm and beauty mesons to separate different flavours using impact parameters and decay lengths. The different reconstruction techniques used i.e. CJC and CST track reconstruction and their linking, determination of the impact parameter and its resolution, hadronic final state and jet reconstruction are then described in detail.

5.1 Analysis Strategy

The distributions used for the heavy flavour signal extraction exploit the long lifetime of heavy hadrons. They are derived from the reconstructed impact parameter or decay length spectra. In the present analysis the displacement of the tracks from the primary vertex is used to measure the fractions of charm and beauty events in DIS jet samples.

The two tracking detectors measuring charged particles' flight trajectories in the central region of the detector i.e. CJC is the backbone of the track measurement here, but the desired accurate track resolution for an efficient lifetime tagging can only be achieved in combination with information from the central silicon detector, the CST. For a more detailed description of the CJC and CST refer to Chapter 2 of this thesis. Association of CST hits and the combined CJC-CST track fit improve the CST track reconstruction.

5.1.1 Experimental Signatures of Heavy Quarks

Due to the confinement principle, quarks cannot be detected "freely". They hadronise and are detected using the products of hadronisation. A large fraction of the particles produced by fragmentation are unstable and decay into stable or almost stable ones, which can be observed. In the following, the description will concentrate on charm and beauty hadron production in *ep* collisions (top quark production is kinematically not accessible at HERA). The fragmentation fractions of *c* and *b* quarks to charm and beauty hadrons are given in Table 5.1.

	fragm. fraction
$c \to D^0$	0.55
$c \to D^+$	0.23
$c \to D_s^+$	0.10
$c \to \Lambda_c^+$	0.08

	fragm. fraction
$b \to B^0$	0.40
$b \to B^+$	0.40
$b \to B_s^0$	0.10
$b \to \Lambda_b^0$	0.10

Table 5.1: *Fragmentation fractions of c quarks to charm hadrons* [63] *(left table) and of b quarks to beauty hadrons* [64] *(right table).*

The properties of charm and beauty hadrons, like masses and lifetimes are summarised in Table 5.2. Hadrons coming from heavy quarks, have large masses in comparison to hadrons coming from light quarks. Moreover, the masses of beauty hadrons are more than twice larger on average, than those of charm hadrons. The other property of beauty hadrons which differs from that of charm hadrons is their longer lifetime leading to typical decay lengths of $\approx 150 - 500\mu m$ compared to the $\approx 100 - 300\mu m$ of charm hadrons. These two properties (mass and lifetime) of

heavy hadrons are used to separate them from light quarks and from each other. The details are discussed in the following sections.

hadron	quark content	mass [MeV]	lifetime τ [ps]	decay length $c\tau$ [μm]
D^0	$c\bar{u}$ $(\bar{c}u)$	1864.6 ± 0.5	0.4103 ± 0.0015	123
$D^\pm$	$c\bar{d}$ $(\bar{c}d)$	1869.4 ± 0.5	1.040 ± 0.007	312
$D_s^\pm$	$c\bar{s}$ $(\bar{c}s)$	1968.3 ± 0.5	0.490 ± 0.009	147
Λ_c^+	udc	2284.9 ± 0.6	0.2 ± 0.006	59.9
B^0	$d\bar{b}$ $(\bar{d}b)$	5279.4 ± 0.5	1.536 ± 0.014	460
$B^\pm$	$u\bar{b}$ $(\bar{u}b)$	5279.0 ± 0.5	1.671 ± 0.018	501
B_s^0	$s\bar{b}$ $(\bar{s}b)$	5369.6 ± 2.4	1.461 ± 0.057	438
$B_c^\pm$	$c\bar{b}$ $(\bar{c}b)$	6400 ± 400	$0.46^{+0.18}_{-0.16}$	138
Λ_b^0	udb	5624 ± 9	1.229 ± 0.080	368

Table 5.2: *Properties of some charm and beauty hadrons* [65].

5.1.2 Impact Parameter

Events containing heavy flavour quarks are distinguished from light quark events by the long lifetime of charm and beauty flavoured hadrons, which leads to displacements of tracks from the primary vertex. These displacements can be quantified by the *impact parameter*. The idea of the method was first used by ALEPH [66]. At HERA, this method has already been used in measurements of the charm and beauty contributions to the inclusive proton structure function F_2 in deep inelastic scattering [67].The impact parameter is defined as the distance of the closest approach of the track to the primary vertex and is illustrated in figure 5.1. Due to the limited z-resolution of the detector, the measurement and all following considerations are made from the $r\phi$-plane only.

A heavy hadron is produced at the primary vertex inside the beam spot which is the transverse profile of the interaction region. It travels typically for a few 100 micrometers (the characteristic decay length, λ, cf. table 5,2) through the detector and decays at the secondary vertex.

The characteristic decay length is defined as $\lambda = c\tau$ where τ is the mean lifetime of the decaying particle at rest. In the experiment, the decaying particles are not at rest

however so there is a boost factor, $\beta\gamma$, which stretches this distance. $\beta\gamma$ can be calculated from the particle kinematics: $\beta\gamma = {}^{P_Q}/_{m_Q}$, where P_Q and m_Q are momentum and mass of the heavy flavour quarks, respectively. The mean decay length for such a boosted decaying particle is then given by $\lambda' = \beta\gamma c\tau$.

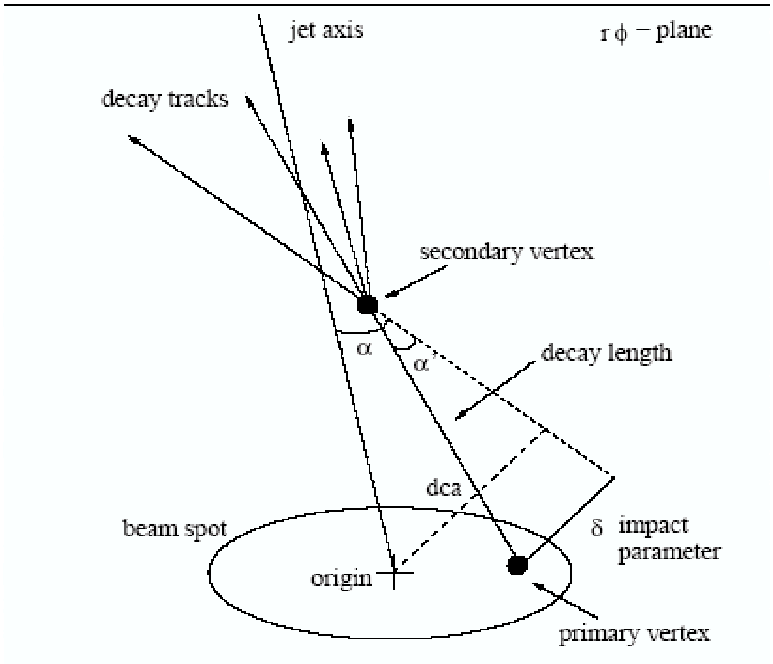

Figure 5.1: *Schematic illustration of impact parameter in the $r\phi$-plane.*

Taking into account the production branching fraction $f(c \longrightarrow C, \Lambda_c)$ and $f(b \longrightarrow B, \Lambda_b)$ the mean weighted decay lengths of charm and beauty hadrons are $155\,\mu m$ and $466\,\mu m$ respectively. Therefore given the contribution of the boost $\beta\gamma$ to the decay length at different values of Q^2 at HERA[1], a lifetime based tag of c- or b-flavoured hadrons and their separation from the light quark background should be feasible if the production and decay vertices are known with a precision$\sim 100\mu m$. This is just on average. The actual decay times and lengths are exponentially distributed with the above means. The probability for the particle to travel a distance L is then:

[1] Since the average boost $\beta\gamma$ at HERA is about 0.7 at low Q^2, the averaged decay length is only $108\mu m$ and $326\ \mu m$ for charm and beauty respectively.

$$P(L) = \exp\left(-L/\lambda'\right) \quad (5.1)$$

The decay length L is related to the lifetime T via

$$L = \beta\gamma . cT = \frac{P_Q}{m_Q} . cT, \quad (5.2)$$

where P_Q, m_Q and $\beta\gamma$ are the heavy particle's momentum, mass and boost factor respectively.

. Equation (5.1) and (5.2) shows the exponential dependence of a particle's real traversed distance L in the laboratory frame between production and decay vertex. Since the analysis is carried out in the $r\phi$-plane, only the transverse part of L

$$L_T = L . sin\theta \quad (5.3)$$

is relevant here with θ being the polar angle of the decaying particle. The real impact parameter δ_{true} of a particle originating from a hadron decay is then defined as

$$\delta_{true} = L_T . \sin\alpha\ , \quad (5.4)$$

where α is the angle between the hadron direction and the direction of the decay particle in the transverse plane (see Figure 5.1) The boost dependence of L_T is approximately compensated for by the factor sin α because sin $\alpha \sim 1/\beta\gamma$.

The lifetime difference between charm and beauty flavoured hadrons leads to significantly different spectra for δ_{true}. For central tracks with $P_T > 0.3\ GeV$ the mean of the true impact parameter distribution is predicted to be about $63\mu m$ and $148\mu m$ for charm and beauty decays, respectively.

The flight direction of the decaying hadron can be approximated by the axis of the highest p_t jet in the event or, when no jets are available by choosing hadronic axis to be 180° away from the direction of the scattered electron in the r-ϕ plane. A *sign* can then be associated to the impact parameter δ, which reflects the relative orientation of a given track with respect to this axis. A positive sign is ascribed if the angle β between the axis of the associated jet and the line joining the primary vertex to the

point of the closest approach of the track is less than 90°, and is defined as negative otherwise. This is illustrated schematically in figure 5.2, which shows the sign convention for impact parameter.

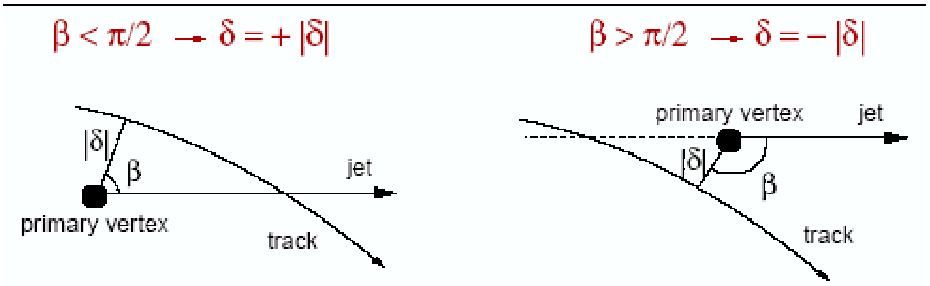

Figure 5.2: *Sign convention of the impact parameter* δ.

It can be seen from the figure that if the hadron comes from a displaced vertex, the sign of the true impact parameter will be positive. Events originated from light quarks tend to have no lifetime information, as they will decay approximately instantaneously to hadrons, therefore the primary and secondary vertices for these event coincide, at least within the spatial resolution probed by H1. Therefore events without lifetime information have a true impact parameter of $\delta_{true} = 0$. Their reconstructed spectrum of δ will therefore be symmetric around zero as shown in figure 5.3, the width of the distribution reflecting the finite track and vertex reconstruction resolutions. Events with decays of long-lived particles are expected to have an excess at positive δ values, resulting in an asymmetric δ distribution.

To use an impact parameter based observable to determine the charm and beauty content of a selected jet event sample, all quantities entering the calculation of impact parameter need to be reconstructed with sufficient precision. According to the expected δ_{true} values an impact parameter resolution of the order of $100\mu m$ coupled with a good knowledge of the jet reference axis, are needed. Otherwise, too many signal events with large δ_{true} will be reconstructed with negative sign, making long lifetime affect inseparable from insufficiently modelled resolution.

With the impact parameter method an event-by-event separation of beauty, charm and light quark events is not possible. For this reason, the contributions from the various quark flavours are determined on a statistical basis. The Monte Carlo simulation

program, RAPGAP, is used to model the contributing processes. The relative fractions of beauty, charm and light quark events are obtained from a least squares fit to observables based on the definition of δ. The variables and the fit procedure are introduced and discussed in *Quark Flavour Separation,* chapter 6 of this thesis.

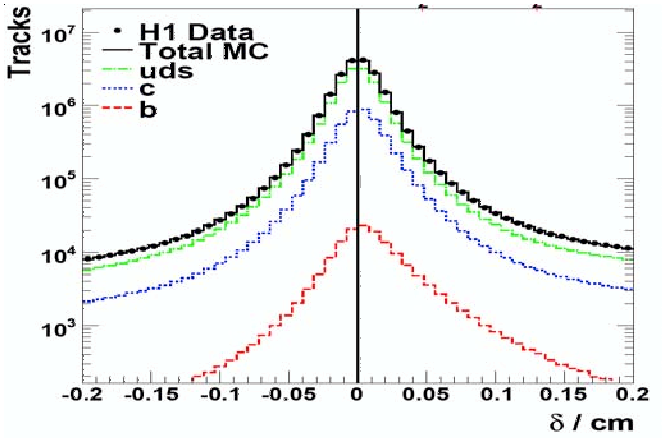

Figure 5.3: *The signed impact parameter δ of a track, shows symmetric (asymmetric) distribution of light flavour shown in green (heavy flavour, shown in blue and red) events around zero,*

5.1.3 Decay Length

A complementary method, not used in this analysis, is to distinguish events with long lived hadrons from events with zero lifetime, i.e. light quarks, by explicitly reconstructed a secondary vertex. In contrast to the impact parameter based method, the reconstruction of the hadron decay vertex requires at least two well measured tracks and is therefore less efficient. Also, the impact parameter depends only weakly on the boost of the decaying particle, whereas the decay length directly depends on it (cf. equation 5.2).

5.2 Track and Vertex Reconstruction determination.

The impact parameter measurements depend on accurate reconstruction of individual tracks, measurement of the main event vertex and, in order to enhance the discrimination against background. In this subsection, the methods used to reconstruct these components are described.

5.2.1 Track Reconstruction.

Reconstruction of the track parameters is based on hits in the central tracking detectors. Due to the presence of a homogeneous magnetic field parallel to the z-direction, charged particles are bent in the $r\phi$-plane. The bending radius r depends on the transverse momentum P_T of the particle and the strength of the magnetic field. The flight path can be described by a helix and its parameterization in H1 coordinates as a function of arc length s is given by

$$x(s) = +(dca - \frac{1}{\kappa}\sin(\phi_0) + \frac{1}{\kappa}\sin(\phi_0 + \kappa s),$$

$$y(s) = -(dca - \tfrac{1}{\kappa}\cos(\phi_0) - \tfrac{1}{\kappa}\cos(\phi_0 + \kappa s), \qquad s \geq 0,$$

$$z(s) = z_0 + s.\cot(\theta). \qquad (5.5)$$

The five track parameters $(\kappa, \phi_0, \theta, dca, z_0)$ unambiguously describe the helix with respect to the origin (0,0,0). These quantities are displayed in figure 5.4.

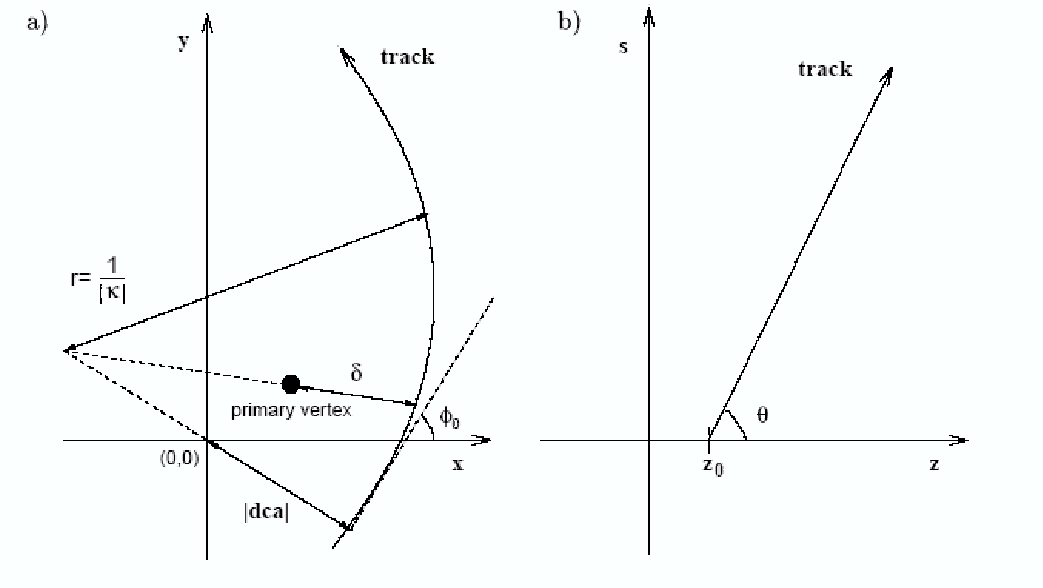

Figure 5.4: *The track parameters* $(\kappa, \phi_0, \theta, dca, z_0)$ *describe the helix in* a) the $r\phi$ and b) the *z s plane with respect to the origin of the H1 coordinate system.*

$\kappa = \frac{1}{r}$ is the curvature or inverse bending radius of the trajectory with positive sign for negative charged particles and vice versa. The flight direction in the transverse plane is given by azimuthal angle ϕ_0. The angle ϕ_0 is measured at the point of closest approach to the z axis which is seen as the starting point of the helix (s = 0).

The distance of the closest approach *dca* denotes the signed minimal radial distance of the origin (0,0) in the $r\phi$-plane. The sign of *dca* is chosen equal to the sign of κ, if the origin is inside the circle which describes the track in the $r\phi$-plane, otherwise it is chosen opposite to it. In the *zs* plane the track is described by a straight line which intercepts the *z*-axis at point z_0. It has a gradient of $\cot(\theta)$, where the polar angle θ gives the flight direction with respect to the positive *z*-axis.

The reconstruction of flight trajectories in the Central Jet Chamber and their corresponding track parameters are determined from a fit to the measured hits in the CJC. The pattern recognition algorithm fits the track parameters in the transverse plane first because the hit resolution in $r\phi$ (~200μm) is superior to the *z* resolution by two orders of magnitude. For the track fit a circular trajectory is assumed. The parameters (θ, z_0) describing the longitudinal track component and are determined from a straight line fit in the *zs* plane.

If a real particle travels through the tracking devices its flight direction is distorted mainly by multiple scattering in the material of the detector. When extrapolating a track measured in the CJC to the CST or still further to particles' production point inside the beam pipe this effect has to be taken into account. The track extrapolation routine CSTCOR handles the distortion coming from multiple scattering, energy loss and inhomogeneities of the magnetic field. A detailed description of the CSTCOR can be found in [68].

5.2.2 CST improved tracks

The position measurements of the CST hits provide the accuracy necessary to resolve the rather small distances separating the production and decay vertices of long lived heavy hadrons. However, the two CST layers alone are not sufficient to reconstruct a track. Therefore the identified CJC tracks are extrapolated to both layers of the CST using CSTCOR routine.

The linking of CST hits and CJC tracks is done using the linking routine CSTLIN [69]. In this algorithm non-vertex fitted tracks (DTNV) are chosen as input and the linking takes place separately in the $r\phi$-plane. The CST improved track parameters can be obtained using p-side information (cf. section entitled CST in chapter2) alone without being affected by possible n-side inefficiencies which can occur due to a worse S/N ratio and hit ambiguities on the *n*-side. If CST hits are found in both the inner and outer layers, they are linked simultaneously, i.e. the hit combination of the inner and outer layers is chosen which maximises the total link probability. This method is far better compared with a separate linking, since the positions of all hits emerging from one particle are correlated.

The CST improved $r\phi$ track parameters are obtained according to the following procedure: For each CJC non vertex fitted track and all possible combinations of *p*-side hits from the inner and outer CST layers, a circle track fit is applied minimizing the following χ^2 function to determine the new track parameters$\bar{T}$:

$$\chi^2 = \left(\vec{T} - \vec{T}_{CJC}\right)^t V_{CJC}^{-1}\left(\vec{T} - \vec{T}_{CJC}\right) + \sum_{hits\ j} \frac{\Delta(\vec{T}, hit_j)^2}{\sigma_\Delta^2}, \qquad (5.6)$$

where $\vec{T} = (\kappa, \phi_0, dca)$ represents the $r\phi$ track fit parameters, $\vec{T}_{CJC}$ and V_{CJC} denote the track parameters and their covariance matrix measured with $CJC.\Delta(\vec{T}, hit_j)$ and σ_Δ stand for the Euclidean distance between the track and the ***j-th*** CST space point and its calculated error. The sum runs over all CST hits linked to the CJC parameters in the *zs*-plane. The solutions with maximal number of CST hits are preferred but must have a reasonable χ^2**.** If more than one CJC track can be associated to one CST hit, the CJC track with the smallest extrapolation error is chosen. The combined CJC tracks with CST information are referred to as *CST tracks* in this thesis. Figure 5.5 shows schematically the different steps involved to obtain CST improved tracks i.e.'*CST tracks'*.

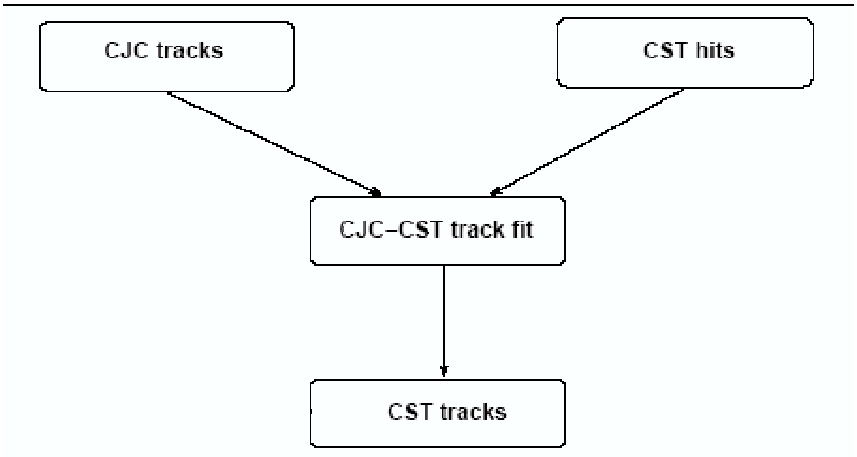

Figure 5.5: *CST track reconstruction.*

5.2.3 Reconstruction of the Primary Vertex

The *beam spot* is the transverse profile of the interaction region at HERA, which extends over a few 100 micrometers with a rather stable mean position for a sequence of runs. In order to ascertain the so called *run vertex* the average coordinates x_{beam} and y_{beam} (both defined at $z = 0$) of the *ep* interaction point as well as the beam tilts[2] α_x and α_y are determined by collecting information from many events.

[2] The incoming electron and proton beams at H1 are slightly tilted with respect to the z-axis.

The run vertex coordinates are obtained by a least-squares fit minimising the overall distances of closest approach using only well measured non-vertex fitted tracks with high transverse momentum.

CSPRIM is the standard procedure at H1 for the reconstruction of the *primary vertex* and a full description of this procedure may be found in [71]. To ensure a high reconstruction quality, it is based on the selection of CST improved tracks and makes use of the CST improved run vertex as constraint. The track selection requires all tracks to be compatible with the run vertex within two standard deviations.

5.3 Impact Parameter Resolution

A good understanding and description of the impact parameter forms the corner stone of this analysis. This is crucial in two respects. Firstly, the resolution has to be small enough to allow the separation of the tracks coming from long lived hadrons from the tracks originated from the decay of the short lived hadrons (i.e. zero lifetime) background. Secondly, the description of impact parameter has to be well understood in order to keep the systematic error small.

Figure 5.6 illustrates the various sources which add up to the total impact parameter resolution. The resolution of the impact parameter is far better now (i.e. HERAII) and in this analysis than before the H1 Tracking detectors upgrade (i.e. HERA I). For tracks with hits in both layers of the CST the intrinsic resolution due to uncertainties on the internal alignment of the CST with respect to the other detector components is measured to be $28\,\mu m$ ($33\,\mu m$ before the upgrade). The effects from *multiple scattering* with the beam pipe and the first layer of the CST are strongly P_T dependent and contribute by $\approx 70\,\mu m/P_T[GeV]$ ($\approx 90\,\mu m/P_T[GeV]$ before the upgrade). Further contributions all depend on the reference point to which the impact parameter is measured, for instance when using the run vertex as reference, the impact parameter is denoted as dca_{RV}, and when the impact parameter is measured with respect to the real, reconstructed primary vertex, it is called dca_{PV} or simply δ. Therefore the primary vertex resolution, the beam spot and the uncertainties on the run vertex and the beam tilt can contribute to the total impact parameter resolution.

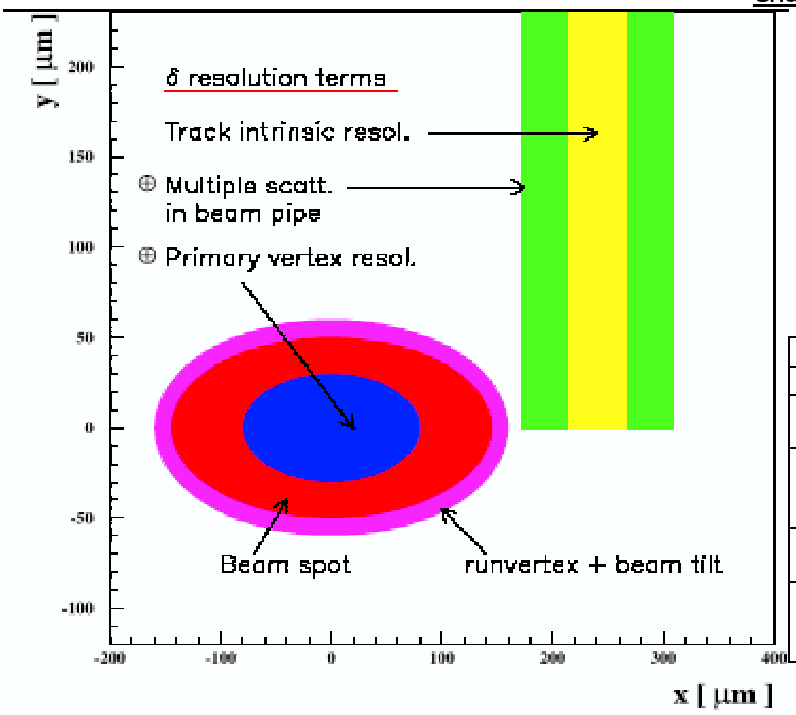

Resolution	HERA I	HERA II
intrinsic	$\approx 33\ \mu m$	$\approx 28\ \mu m$
Multiple scattering	$\approx 90\ \mu m/P_t$	$\approx 70\ \mu m/P_t$
Beam spot	x: 145 μm y: 25 μm	x: 90 μm y: 20 μm
Run vertex	$4-20\ \mu m$	$2-5\ \mu m$
Primary vertex	x: 51 μm y: 23 μm	x: 50μm y: 20 μm

Figure 5.6: *Schematic view of the various contributions to impact parameter resolution* [71]. *The table on the right shows these contribution in HERA I and HERA II (in which the data for this analysis were gathered), hence the resolution of the detector is superior in HERA II phase of operation compared with HERA I phase.*

5.3.1Track resolution

Now that different contributing sources to the resolution of the impact parameter have been identified, the contributing sources are discussed in detail. In order to preserve a high statistics data sample, in the final selection, tracks down to a transverse momentum of 300 MeV are analysed. In the low P_T region the impact of multiple scattering effects is large and must be well controlled.

The description of the track resolution can be investigated by looking at the CJC-CST track linking probability, P_{link}, which is a direct measure of the accuracy of the covariance matrix of the track parameters. The link probability of the CST hits with the CJC tracks is defined as

$$P_{link}(\chi^2, N) = \frac{1}{\sqrt{2^N}\Gamma(N/2)} \int_{\chi^2}^{\infty} e^{-\frac{1}{2}t} t^{-\frac{1}{2}N-1} dt, \qquad (5.7)$$

where χ^2 is defined in equation (5.6), and N denotes the number of linked CST hits, i.e. the available number of degrees-of-freedom. P_{link} denotes the probability of successful matching of the CST hits and CJC tracks. Strictly speaking, P_{link} is the probability of having a larger χ^2 value than achieved by the minimisation algorithm defined in equation (5.6). The probability distribution should be flat between 0 and 1 if the covariance matrix is accurately described.

In figure 5.7 the CJC-CST link probability for tracks with $P_T > 0.3\ GeV$ (as in the final track selection) is shown. In the left plot the link probability for one CST hit and one CJC track can be seen while in the right plot the link probability of two CST hits and two CJC tracks is shown. It is these P_{link} (i.e. two hits and two tracks) that are used in this analysis. Furthermore, $P_{link} > 0.001$ was required. Earlier analyses were carried out with a $P_{link} > 0.1$ [67].

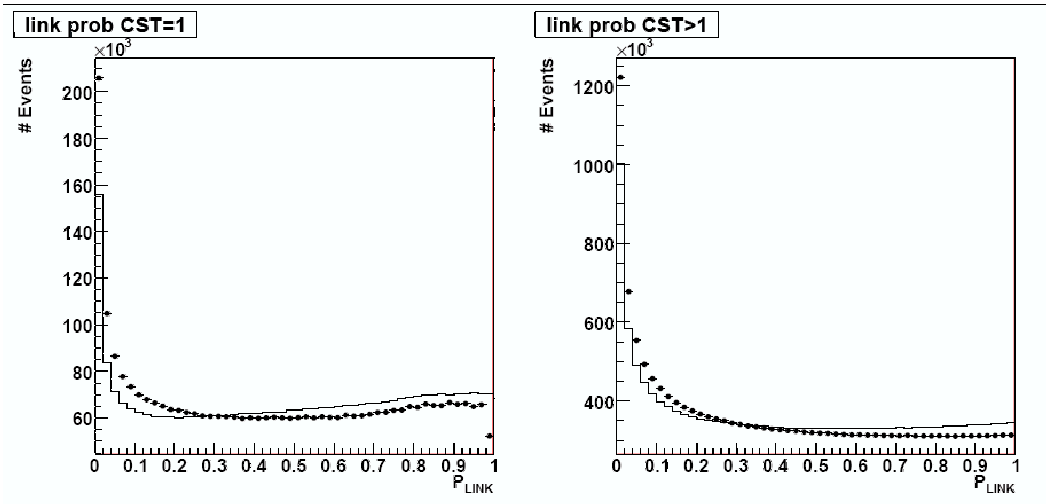

Figure 5.7: *Shows the link probability, P_{link},, for matching successfully one(more than one) CJC track(s) to a CST hit(s) on the left plot (on the right plot).The data(black points with error bars) are adequately described by Monte Carlo(solid black line) the difference is due to the CJC error description.* [67] [67]

5.3.2 Track Finding Efficiency

Based on the CJC-CST link probability the track finding efficiency can be investigated. For this purpose tracks with at least 2 CST hits and $P_{link} > 0.001$ are selected. The CST efficiency is defined as the ratio of the number of tracks fulfilling these CST cuts over the total number of CJC tracks.

Within the CST range, the efficiency to obtain a CST track from a CTD track is 91% for $e^{-}p$ and 95% for $e^{+}p$ (figure 5.8).

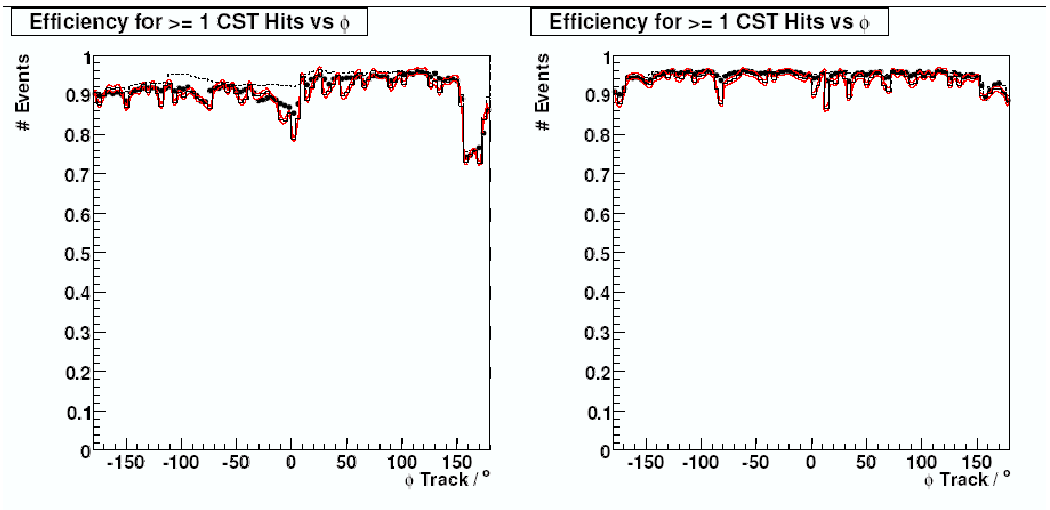

Figure 5.8: *The efficiency of one or more CST hits is shown above and it was found to be 91% for $e^{-}p$ (left) and 95% for $e^{+}p$ (right). The Monte Carlo efficiency is shown separately for the default (solid black line) and modified (dashed red line) version. The solid black dots are the data.*

The total CST track finding efficiency includes the CST hit efficiency, the CJC-CST linking efficiency and losses due to inactive CST regions. Figure 5.9 shows the efficiency of CST tracks with respect to P_T and z_{CST} direction of tracks. The efficiency is seen to be nearly flat but slowly falling with increasing P_T (i.e. track P_T, figure 5.9, left). The default Monte Carlo efficiency is a bit higher, which is due to the still imperfect description of the CJC-CST link probability (cf. figure 5.7).

In order to account for this small discrepancy in the simulation, the track finding efficiency is downgraded by approximately 1.5% with a small P_T dependence (over all track error is 2.2%). The improved Monte Carlo simulation is shown as solid black line. The agreement between data and simulation is good: this holds also for the efficiency as a function of z_{CST}, displayed in figure 5.9 (right).

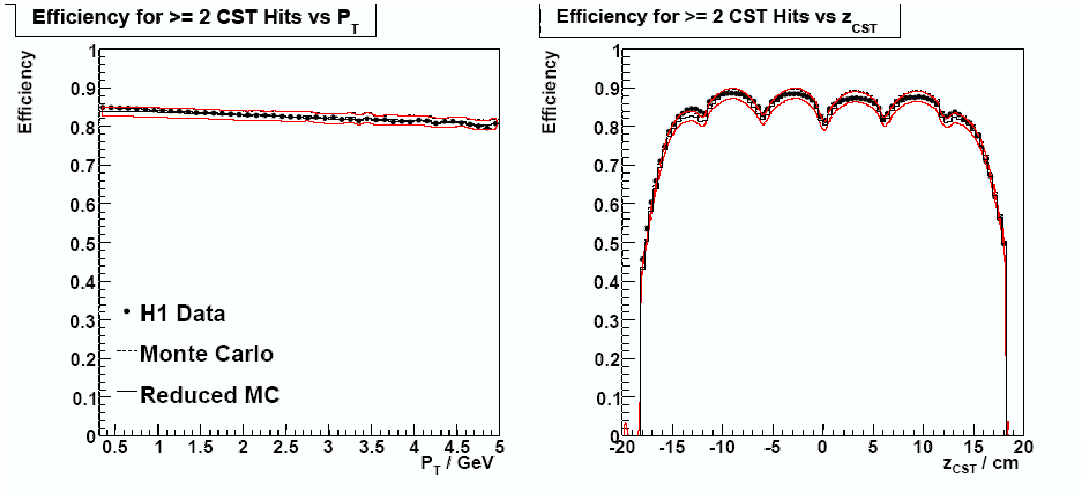

Figure 5.9: *CST track finding efficiency for tracks with at least 2 CST hits and* $P_{link} > 0.001$ *as function of* P_T^{track}*(a) and* z_{CST}*(b). The Monte Carlo efficiency is shown separately for the default (dashed red line) and modified (solid black line) version. The distribution of the data are shown as the solid black dots.*

5.3.3 Impact Parameter Resolution

In order to separate contributions from the primary vertex fit, the run vertex is used as a reference in the impact parameter definition. For tracks with at least two CST hits and a minimum transverse momentum of $P_T > 0.3$ GeV the Gaussian width of the dca_{RV} distribution as a function of the track azimuthal angle ϕ is shown in figure 5.10. Neglecting the error on the run vertex, the width of dca_{RV} depends on the beam

spot size and the track resolution. The ϕ dependence of the dca_{RV} resolution is expected to follow a function of the form

$$\sigma^2_{dca_{RV}}(\phi) = \sigma^2_{T\kappa} + \sigma^2_x sin^2(\phi) + \sigma^2_y cos^2(\phi), \qquad (5.8)$$

where $\sigma_{T\kappa}$ accounts for the track resolution and σ_x and σ_y represent the transverse size of the beam spot. The parameters of the beam spot have been taken from H1 measurements in the HERA II phase and are $\sigma_x = 90\ \mu m$ and$\sigma_y = 20\ \mu m$ (cf. to figure 5.6, right table). These parameters are used in both the simulation and the fit. The simulation (red dots) seems to agree well with the data (black dots) in figure 5.10.

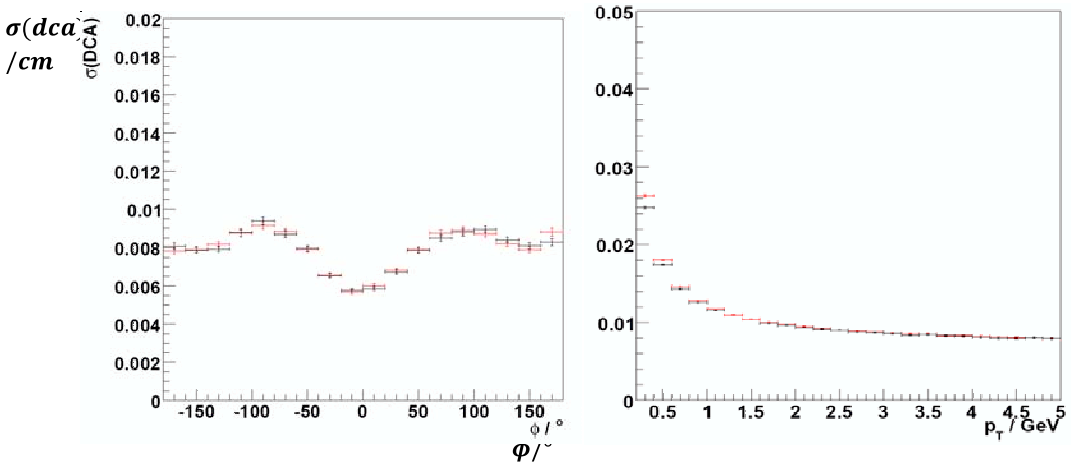

Figure 5.10: *Gaussian width of dca_{RV} distribution as a function of the track direction around the beam. Tracks with at least two CST hits and $P_T > 0.3\ GeV$ are shown for data (black dots) and simulation by RAPGAP (red dots). The shape of the curve corresponds to $\sim \sigma^2_x sin^2(\phi) + \sigma^2_y cos^2(\phi)$ with parameter $\sigma_x = 90\ \mu m$ and $\sigma_y = 20\ \mu m$. On the right the distribution is shown as a function of P_T and it can be seen that the resolution improves with increase in P_T.*

The contribution coming from tracks is constant at $\approx 70\ \mu m$, the extension of the beam spot can be read from the dotted line. As expected, for $\phi = \pm 90°$ essentially the large dimension of the beam ellipse in x direction is seen, resulting in a resolution of $\approx 90 \mu m$ as, whereas towards $\phi = 0°$ ($\phi = 180°$) the resolution reaches $\approx 25 \mu m$ corresponding to the beam extension in y. Figure 5.11 shows the DCA errors, there are two main sources, the uncertainty on track and the uncertainty on the primary vertex reconstruction, the total error is the sum of these in quadrature.

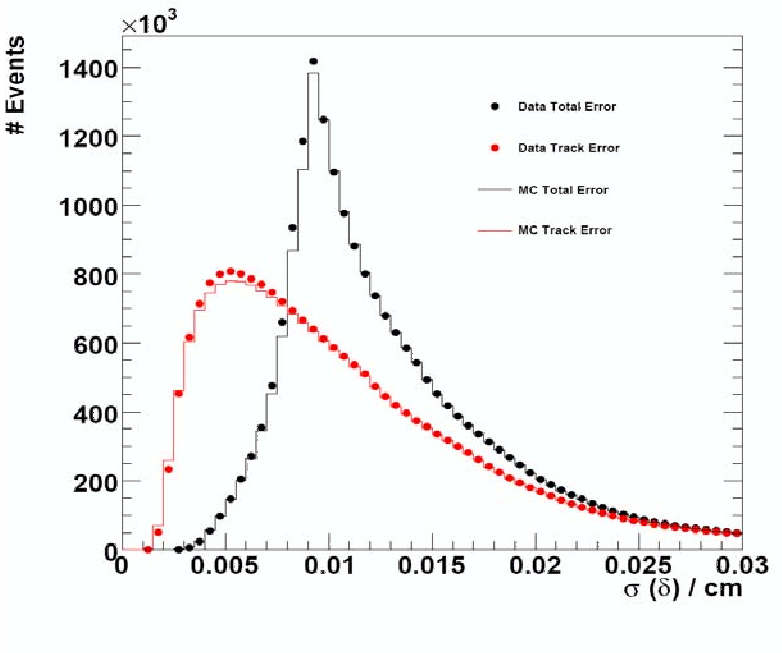

Figure 5.11: *The error on DCA, the contribution from data and Monte Carlo simulation are shown.*

In summary, using the run vertex as an anchor for the impact parameter measurement results (for tracks with $P_T > 0.3$ GeV) in a resolution of $\approx 100 - 160\ \mu m$, depending on the track direction in ϕ. With the reconstruction of the run vertex and primary vertex as well as the improved track resolution the best impact parameter resolution achieved with tracks down to 300 MeV is about $110 \mu m$. Comparing this to the true impact parameter expected for charm and beauty of 63 μm and 148 μm respectively we see why a good understanding of δ-resolution is crucial. This resolution improves with higher values of track P_T (cf. figure 5.10, the plot on the right), because of the strong dependence of the resolution on the transverse momentum arising from multiple scattering in the material in front of the detector, in the case of CST tracks the beam pipe and the first silicon layer. The shape in figure 5.10 (right plot) can be described with

$$\sigma_{dca}^2 = \sigma_{int}^2 + (A_{MS}/P_T)^2, \qquad (5.9)$$

where σ_{int} denotes the intrinsic resolution and the parameter A_{MS} describes the multiple scattering. The asymptotic value σ_{int} achieved for high momentum tracks and

depends only on the detector's intrinsic hit resolution and the length of the extrapolation's lever arm from the detector to the interaction region. $A_{MS} \approx 80\mu m/\text{GeV}$ and is proportional to the square root of the material thickness x traversed, measured in units of the mean radiation length $X_0 \sim \sqrt{x/X_0}$.

Additional techniques have been used in order to separate different flavours the details of which can be found in chapter 6 of this thesis.

5.4 HFS Reconstruction and Jet Finding

As well as track and vertex reconstruction, the analysis method also needs a means of estimating the direction of the decaying hadron. As explained in section 5.2, this can be obtained by forming jets from reconstructed hadronic final state objects and using the direction of the highest P_T jet (or by using information from the scattered electron). In this subsection, the hadronic final state reconstruction and jet finding is described.

5.4.1 HFS Reconstruction

The HADROO2 algorithm [58] was used in this analysis to reconstruct the hadronic energy of events. The basic idea behind the HADROO2 algorithm is to use information from both track measurement and the calorimeter, depending on the uncertainty of the measurements in the respective devices. Only a brief description of the algorithm is given here.

Track and Cluster Selection

The HADROO2 algorithm starts by selecting good quality tracks as defined by the heavy flavour group, the so called "Lee West" tracks [72]. These tracks are measured with the central and forward tracking detectors. The tracks are classified in three categories, Central, Combined and Forward. For details on the specification see [58]. Figure 5.12 depicts the ranges in θ for these three categories of tracks. For HERA II data and Monte Carlo, pure forward and combined tracks are excluded because their

kinematics as well as their error measurements are not well studied and described at present (this analysis relies on tracks$30 < \theta < 150°$).

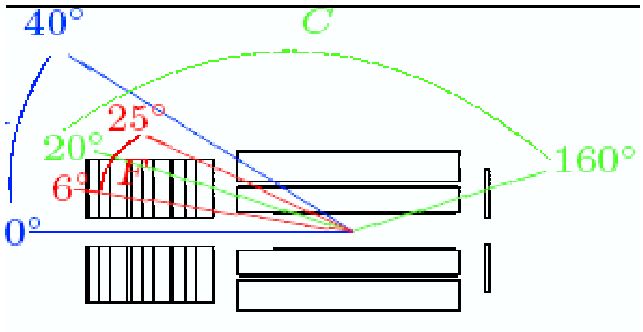

Figure 5.12: *Illustrates the different ranges for Central (green), Combined(blue) and Forward (red) tracks with regards to the angle θ [58].*

Calorimetric clusters are made out of LAr and SpaCal clusters only. The main requirement when selecting the clusters is to suppress the noise coming from the electronics or non *ep*-physics events. Any identified electrons and muons which are not isolated[3] are considered as being part of the HFS but their associated tracks and clusters are removed from the input list.

The algorithm

The HADROO2 algorithm is based on the combination of the selected tracks and clusters. The track and cluster information is matched avoiding double counting of energies. The decision whether to take the track or the cluster information to construct the HFS object is based on a comparison of their relative resolutions. Due to possible contributions of neutral particles the exact precision of the calorimeter is unknown. Therefore the average relative error expected for the calorimeter measurement is calculated using

$$\left(\frac{\sigma_E}{E}\right)_{LAr}^{expected} = \frac{\sigma_{ELAr}^{expected}}{E_{track}} = \frac{50\%}{\sqrt{E_{track}}} \qquad (5.10)$$

[3] A muon is isolated if calorimeter energy in a cylinder (of radius 35 cm in the electromagnetic, and of 75 cm in the hadronic LAr section) around the extrapolated muon track is below 5 GeV.

The track measurement is considered as being superior if

$$\left(\frac{\sigma_E}{E}\right)_{track} < \left(\frac{\sigma_E}{E}\right)_{LAr}^{expected} \quad (5.11)$$

Generally the tracker measurement is better up to 25 GeV for central tracks ($20° < \theta < 160°$). If the condition 5.11 is met, the track information is preferred and the HFS object is created based on the track measurement. In order to avoid double counting of energies, electromagnetic (hadronic) energy in clusters within a cylinder of 25cm (50cm) around the extrapolated track is removed until the discarded energy is approximately equal to the track energy(details in [58]).Possible fluctuations of both measurements are taken into account in this procedure. Potentially remaining cluster energy is due to neutral particles or belongs to another track extrapolated in the same region of the calorimeter.

If condition 5.11 is false and if E_{track} is within 2σ of $E_{cylinder}$ (with $\sigma E_{cylinder} = 0.5\sqrt{E_{cylinder}}$), the track and calorimetric energy measurements are considered to be consistent and the calorimetric measurement is used to create the HFS object.

If the track energy is below the measured cluster energy ($E_{track} < E_{cylinder} - 1.96\sigma_{E_{cylinder}}$), the track measurement is used and the calorimetric energy is subtracted in the same way as described before when the track precision is better than the expected calorimeter precision.

Otherwise, if $E_{track} < E_{cylinder} + 1.96\sigma_{E_{cylinder}}$, the cluster energy defines the HFS object and the track measurement is suppressed.

5.4.2 Jet Finding

In general, measuring jet cross sections provides a powerful tool to study and test the predictions of Quantum Chromodynamics. The observed jets provide a view of the underlying hard quark and gluon interactions that occur at very small distance scales. However, due to the *confinement principle*, single quarks or gluons cannot be detected. Instead partons must combine to a group of colourless hadrons, which are

the measurable final state particles of the reaction. Furthermore, since the quarks and gluons carry non-zero colour charges and the final hadrons do not, there can be no unique association of a jet of hadrons with a single initial quark or gluon. However, with a suitable definition of jet cross section one can minimise the effect of long distance physics and of the inherent jet ambiguities and obtain a fairly precise picture of the short distance dynamics.

The inclusive K_t algorithm [62] has turned out to be best suited in that it minimises the effect of the long distance hadronisation. There are other advantages in using K_t algorithm, for example the fact that the cone algorithm problem with overlapping jets disappears [73].

Another aspect of great importance is that the jet algorithm should be collinear and infrared safe. In perturbative QCD, divergencies occur whenever two massless partons are collinear (parallel) or one massless parton has a vanishingly small (infrared) energy. Both divergencies are cancelled in the total cross section by virtual contributions. For this cancellation to take place the treatment of the two parallel particles must be identical to the treatment of a single particle with their combined momentum. This must also be true in jet calculations: the jet must not be affected by the addition of soft particles.

On the other hand, from the experimental point of view, the jet algorithm must not depend on the resolution of the detector, e.g when two parallel particles go into the same calorimeter cell, or for example in trigger response when additional low energy particles are emitted.

In the present analysis jets are always defined using the inclusive K_t jet algorithm. The K_t jet algorithm is a cluster algorithm which starts by finding pairs of particles nearby in phase-space and merging them together to form new pseudo-particles which are themselves merged in an iterative process to become the output jets. In the current analysis the algorithm is applied in the laboratory frame using a P_T weighted recombination scheme. The usual way to do this is to require the distance $\sqrt{\Delta\phi^2 + \Delta\eta^2}$ of the two particles in the $\eta\phi$-plane to be smaller than a separation parameter, R, which is required to be one (i.e. R=1). This procedure is repeated until no further merging is possible and the remaining objects are classified as jets. For a more detailed description of the iteration procedure see [62].

Chapter 6

"Three quarks for Muster Mark …"

James Joyce, Finnegan's wake

Flavour Separation

In this section the charm and beauty "lifetime tagging" method which is used for the measurement of the cross sections presented in this thesis is discussed. The chapter begins by introducing the different tagging methods used in HERA. Then the significance distributions S_1, S_2 and S_3 are discussed in detail, followed by the fit procedure. The chapter concludes with a discussion of scaling factors.

Heavy Flavour Tagging Methods

There are five basic tagging methods used at HERA for separating different quark flavours, figure (6.1).

Full reconstruction of decays of heavy flavoured hadrons into charged tracks, e.g. $D^+ \to K^-\pi^+\pi^+$ is used at HERA only for charm tagging. Due to the small statistics brought about by comparatively low beauty production rates and the small branching ratio for suitable decay channels this method is not used for beauty tagging.

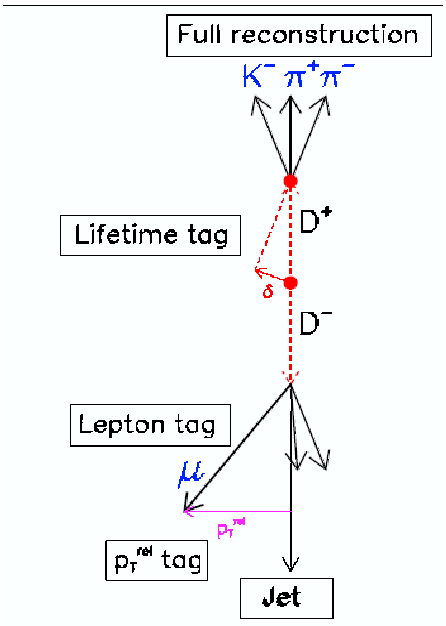

Figure 6.1: *Basic tagging methods for heavy flavour events.*

Muons or electrons from semileptonic *b* and *c* decays are used in *Lepton tagging*. This method is sensitive for beauty tagging, since beauty decay produces leptons of relatively high momenta that can be readily identified.

In P_T^{rel} *tagging*, the relative transverse momentum P_T^{rel} of lepton (muon or electron) to the axis of the associated jet is used. This method is used to tag beauty hadrons exploiting the large beauty mass which translates to large P_T^{rel} values.

Jets are used to estimate the heavy quark's direction for the lifetime method based on the signed impact parameter of the track and the P_T^{rel} method, but jets are not per se a heavy flavour tag. Jets are used as a general tool to tag and measure the kinematics of outgoing hard partons produced or scattered in the interaction.

Finally, the *lifetime tagging* method which is used in the present analysis, exploits the long lifetimes of *charm* and *beauty* quarks, which lead to displaced secondary decay vertices. These tags are based either on the full reconstruction of the

secondary vertex from the charged decay tracks, or on the displaced signed impact parameter δ of charged tracks, i.e. their distances from the primary vertex.

All the methods mentioned above apart from the *lifetime tag*, suffer from the fact that only a fraction of the charm or beauty quark decays leads to the selected final state. These shortcomings can be circumvented by using an *inclusive tagging method*, based on the long lifetime of *charm* and beauty *quarks*.

In this analysis events containing charm and beauty quarks are identified using the same method as in previous H1 measurements {[60],[67]}. The impact parameters of selected tracks are used to construct significance distributions. For optimal statistical precision different significance distributions are used for events with different multiplicity. The *first significance* distribution S_1, is defined for events where only one track is linked to the jet. The *second significance* distribution S_2, is defined for events with two or more tracks associated with the jet and similarly S_3, the *third highest significance*.

To eliminate a large fraction of the light quark background and to substantially reduce the uncertainty due to the impact parameter resolution, negative bins in the S_1, S_2 and S_3 distributions are subtracted from the corresponding positive bins. Finally the fraction of events containing *charm* and *beauty* are extracted from a simultaneous χ^2-fit to the subtracted S_1 ,S_2 and S_3 distributions and the total number of inclusive events before track selection. The latter information is mainly needed for constraining the light quark contribution.

6.1 Lifetime Tagging Method

In this section the different steps involved in the lifetime tagging are discussed in detail. In order to extract information based on the lifetime of the *charm* and *beauty* quarks the following stages have been followed;

- For each event a 'jet axis' is defined.

- Tracks are associated to the jet axis.
- Background from strangeness events (K_s^0 and Λ decays) is suppressed
- To separate different contributions (i.e. heavy flavour events and light quarks), impact parameter and significance distributions (i.e. S_1 , $S_2$and S_3) are used.
- The fraction of events containing *charm* and *beauty* are extracted from a simultaneous χ^2-fit.

6.1.1 Jet Axis

In order to identify long lived hadrons, a *jet axis or quark axis* is determined. Jets with a minimum P_T of 1.5 GeV, in the angular range of $15° < \theta < 155°$ are reconstructed. Figure 6.2 shows the distribution of the total number of jets (in most cases there is just one) reconstructed per event together with the contributions from various quark flavours.

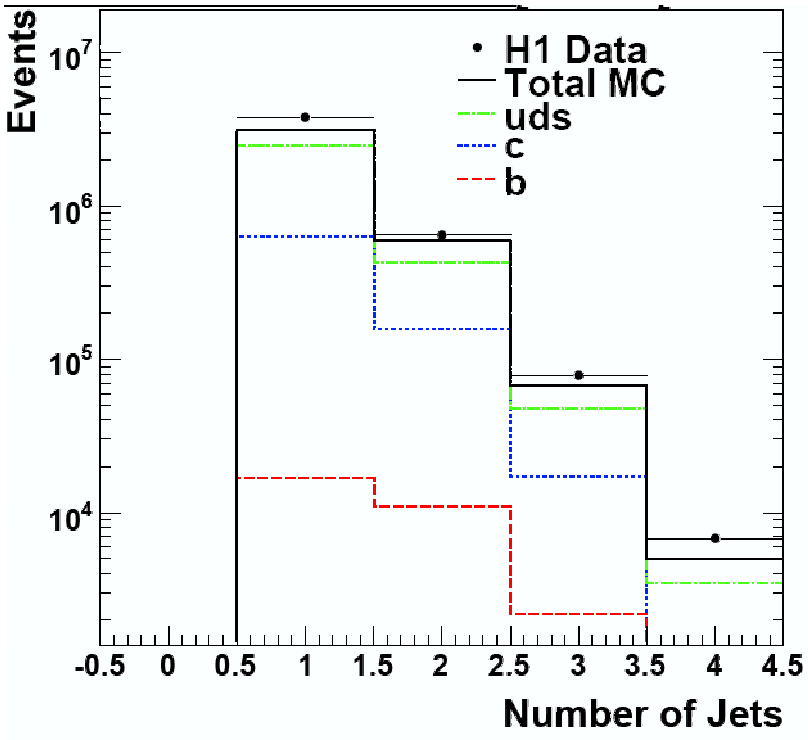

Figure 6.2: *The number of jets per event. The contributions from the various quark flavours are shown in different colours.*

The direction of the quark (quark axis) ϕ_{quark} or *jet axis* is defined by the azimuthal angle of the jet with the highest transverse momentum and is used to calculate a signed impact parameter (δ) for each track (see Figure 6.3). If there are no jets reconstructed in the event. The quark axis is determined from azimuthal angle of the scattered electron (positron) $\phi_{quark} = 180° - \phi_{electron(positron)}$. The distance of the closest approach (DCA) is determined for each CST improved track associated to the quark axis within $|\Delta\phi| < {}^{\pi}/_{2}$.

6.1.2 Matching of Tracks to Quark Axis

For calculation of the DCA only those tracks matched to the quark axis, i.e. that which are close to it in ϕ ($|\Delta\phi| < {}^{\pi}/_{2}$) are used. Tracks with azimuthal angle outside of this $\pm 90°$ cone around ϕ_{quark} are rejected. Figure 6.4 shows the distributions of the number of CST tracks per event before and after track association to the quark axis.

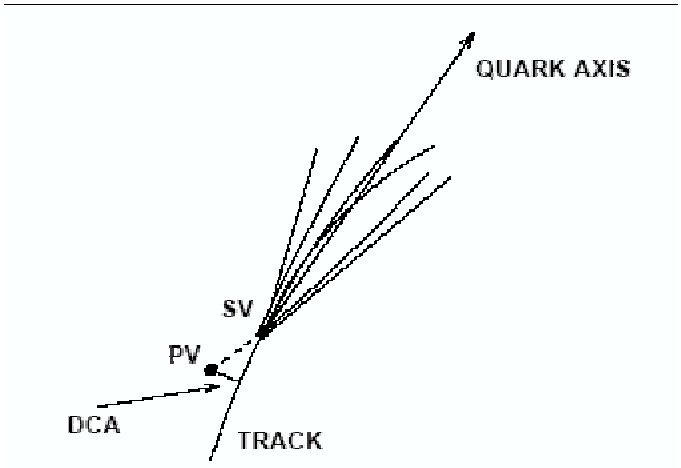

Figure 6.3: *Illustration of the distance of the closest approch (DCA) and quark axis in rϕ-plane.*

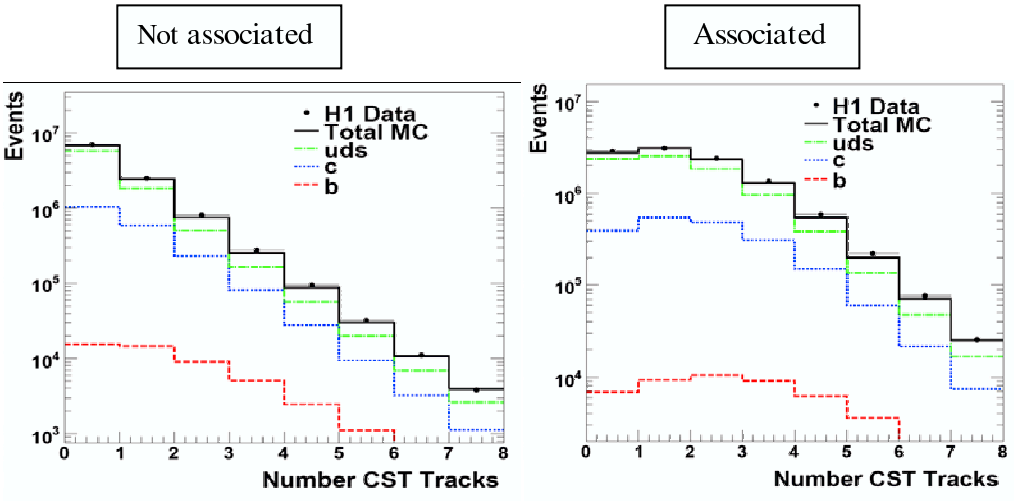

Figure 6.4: *The number of CST tracks per event before (left figure) and after (right figure) track association to the quark axis*

.6.1.3 Details of the Track Selection

Only those tracks that have passed the selection criteria outlined in table 6.1 are considered and only tracks that can be associate to a jet (using criterion described in 6.1.3) are selected.

Table 6.1 summarises the track selection criteria which ensure a track reconstruction with a reliable precision while keeping enough statistics. Tracks with a transverse momentum greater than 0.3 GeV are selected because at lower transverse momenta the resolution of the impact parameter deteriorates through multiple scattering. Despite the fact that the jet axes are already required to lie within the central region, track angular cuts are needed to guarantee that each asscoiated and selected track falls inside the CST acceptance range and is well-measured.

Track Selection	
Transverse momentum	$P_T > 300$MeV
Angular region	$15° < \theta < 155°$
CJC radial track length	$l_{track} > 36\ cm$
CJC track start radius	$R_{Start} < 50$ cm
CST hits	$N_{CST} \geq 2$
CJC-CST Link probability	$\mathcal{P}_{link} > 0.001$

Table 6.1: Track selection criteria.

The radial track length is determined by the design of the jet chambers with a maximum track length of 64.1 cm (the difference between the outer CJC2 and inner CJC1 radii). For reasonable determination of the CJC track parameters the minimum radial track length is required to be 36 cm. To ensure precise extrapolation of the CJC track to the CST, the start radius of the CJC track must be inside the CJC1 (i.e. $R_{Start} < 50$ cm).

The CST cuts provide the necessary quality of the track reconstruction close to the interaction region. At least two hits in the two layers of the CST are demanded with a minimum CJC-CST track link probability of 0.1%, the lowest value possible (recall that $\mathcal{P}_{link}$ is the probability of having a larger χ^2 value than achieved by the minimisation algorithm).

Figure 6.5 shows some of the control distributions of the parameters discussed above . All tracks that fulfil the track cuts according to table 6.1, and are associated with a jet, enter these distributions. The data are compared with the

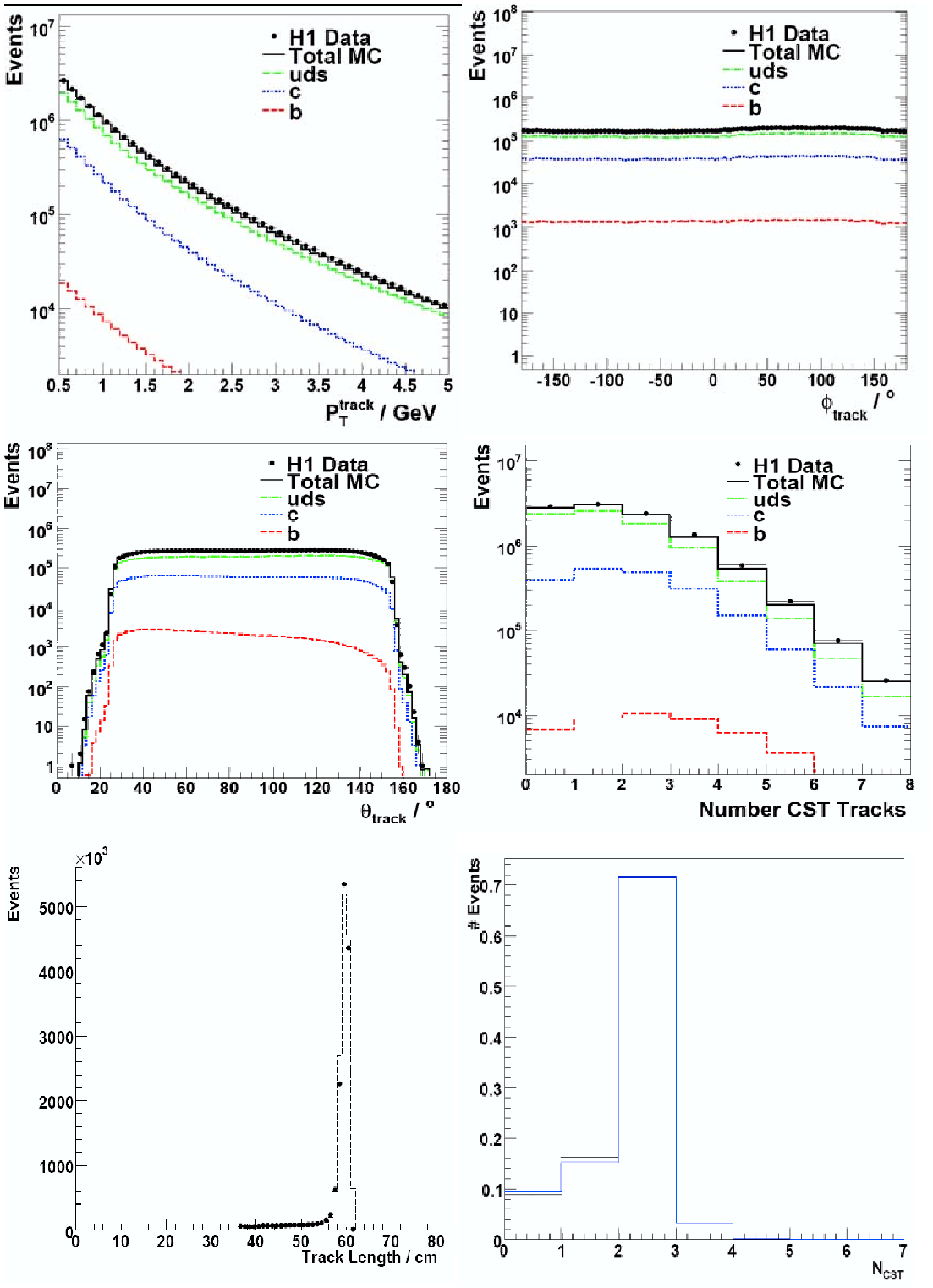

Figure 6.5: *Control distributions of the selected tracks. The expectation from the RAPGAP Monte Carlo simulation is included in the figures (black solid lines), the contributions from different flavours are shown (colour coded). In the last couple of plots (track length and number of CST hits) only the total expectation from MC (solid blue) and the data(solid dots) are shown.*

expectation from RAPGAP Monte Carlo simulation. The contributions from different quark flavours are shown separately with relative normalisations according to the individual scale factors for each flavour as described in section 6.3.

The overall agreement between data and simulation is good. Especially the track transverse momentum and the angular spectra are well reproduced by the Monte Carlo simulation.

In the distribution of the number of selected CST tracks a small shift between data and simulation is observed. The track multiplicity is seen to be somewhat higher in data, albeit the descriptions still reasonably agree. The small deviations are mainly due to a non-perfect modelling of the multiplicities in light quark jets and have a negligible effect on the overall measurement given that we are predominantly concerned with heavy flavour jets.

6.2 Impact Parameter and Significance in Lifetime tagging

6.2.1 Impact Parameter

The different quark flavours that contributes to the cross section can be distinguished on the basis of differences in the reconstructed impact parameter spectrum of selected CST tracks.

Recall that the impact parameter (δ) is defined as the transverse distance of closest approach (DCA) of the track to the primary vertex (cf. figure 6.3). The δ is constructed using tracks matched to the quark axis in $\phi(|\Delta\phi| < {}^{\pi}/_{2})$. The sign of the impact parameter is, defined as follows. If the angle between the jet axis and DCA is less than 90°, the impact parameter is defined to be positive, otherwise the impact parameter is said to be negative. Tracks from the decay of long lived hadrons predominantly will have a positive impact parameter { [29], [67]}.

The distribution of the reconstructed signed impact parameter and its error is shown in figure 6.6. The simulation gives a good description of the data. Due to the long lifetimes of *charm* and *beauty* flavoured hadrons the impact parameter distribution for heavy quarks is asymmetric, the number of tracks with positive values exceeding the number of tracks with negative values.

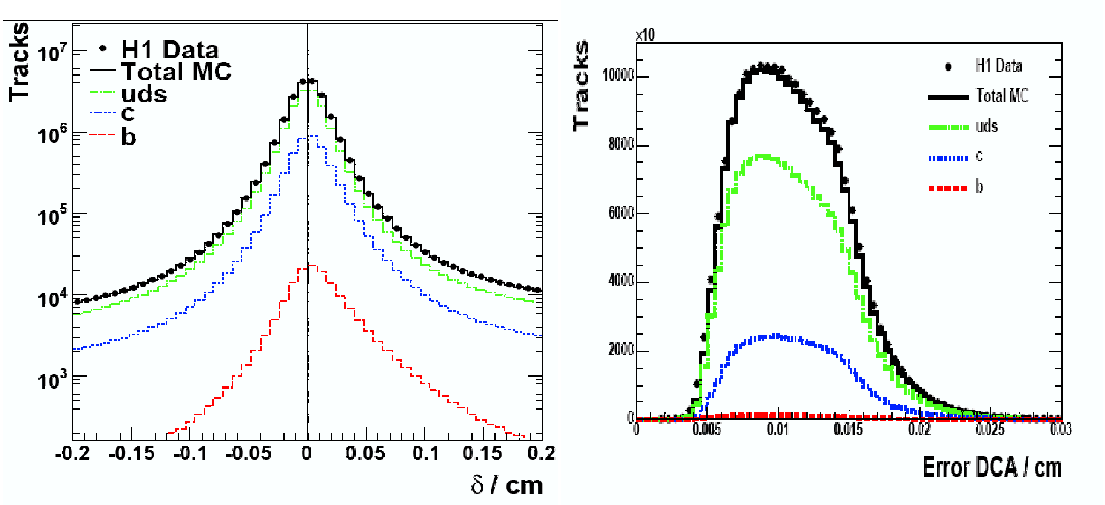

Figure 6.6: *Distribution of the reconstructed impact parameter (left) and its error (right).The data is well described by the Monte Carlo simulation. The asymmetric distribution of heavy quarks can be observed (red and blue colours) with a positive skew, whereas the light quarks (green) distribution is symmetric around zero..*

The asymmetry seen at $|\delta| > 0.1\ cm$ is due to decays of long lived strange particles such as K_s^0 (see next section). In order to reduce the effects of the strange component, a cut of $|\delta| < 0.1\ cm$ is imposed on all the selected tracks. Figure 6.7 shows the DCA distribution with this cut applied.

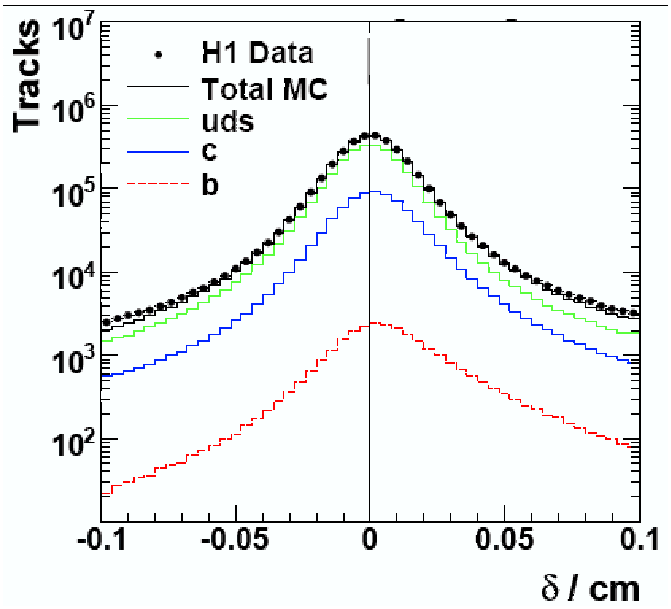

Figure 6.7: *Distribution of the reconstructed impact parameter with* $|\delta| < 0.1\ cm$ *cut.*

6.2.2 Significance

Significance is defined as the ratio of the impact parameter to its error.

$$S_i = \frac{\delta_i}{\sigma_{\delta_i}} \tag{6.1}$$

where δ_i is the impact parameter of selected track (i) and σ_{δ_i} is the error of the impact parameter for that track. The distribution of the σ_δ receives contributions from the vertex and track errors and reaches values of $200\mu m$ (towards the tail end of the distribution) at maximum and as shown in figure 6.6 (right plot) it is described well by the simulation.

The significance distribution for all selected tracks is shown in figure 6.8 with a cut of $|\delta| < 0.1\ cm$.

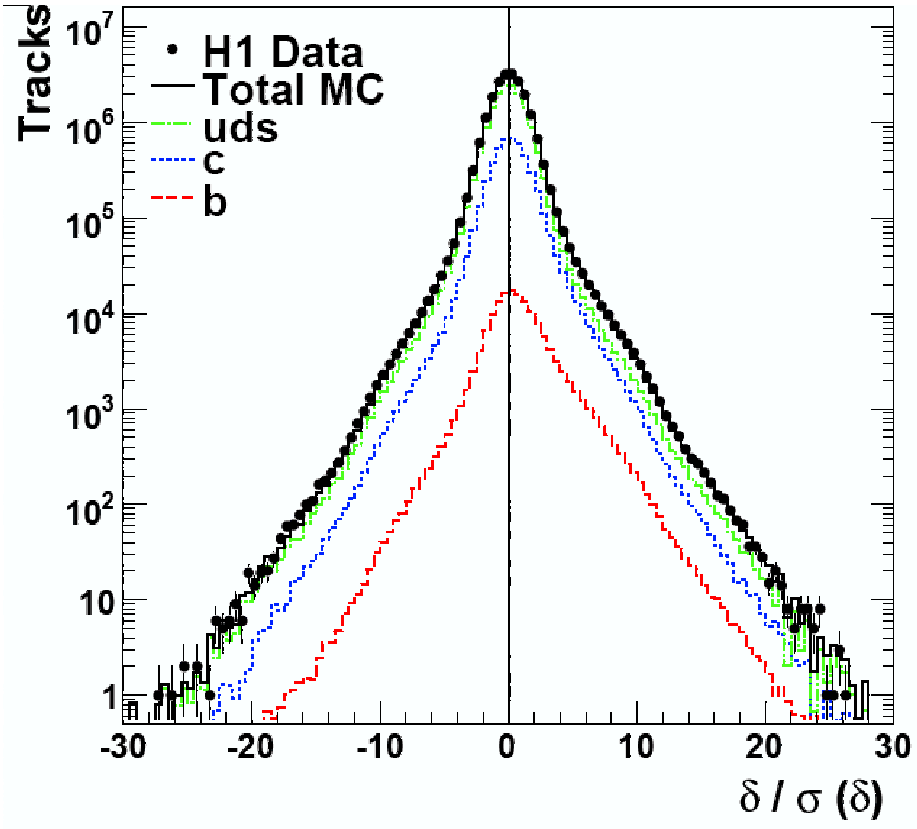

Figure 6.8: *Distribution of the significance for all tracks with a cut of* $|\delta| < 0.1$ *cm. The simulation from the RAPGAP Monte Carlo is included in the figure, showing the contributions from the various quark flavours (colour coded) after applying the scale factors obtained from the fit to the subtracted significance distributions of the data(see section 6.3)*

The construction of the significance optimises the flavour separation, because the error reflects the influence of the specific decay topology and multiple scattering on the impact parameter measurement. The simulation describes the data very well, apart from the tails of the distribution where imperfect modelling of the resolution by the simulation leads to a small discrepancy between the data and the simulation. This discrepancy is treated as a systematic error (cf. chapter 7).

In order to enhance the flavour separation power of the significance method, different significance distributions for events with different track multiplicity are used. The *first Significance* distribution (S_1) is defined for jets where exactly one

reconstructed CST track is linked to the jet, and is simply the absolute significance of the track. The *second significance* distribution (S_2), defined only for jets with at least two or more reconstructed CST tracks associated to the jet, is the significance of the track with the second highest absolute significance. Similarly the *third significance* distribution (S_3) is defined for tracks with the third highest absolute significance. The distributions of each of these quantities i.e. S_1, S_2 and S_3 are made for all selected events. The events contributing to the S_2 distribution also contribute to the S_1 distribution. Similarly, those events contributing to the S_3 distribution also contribute to the S_2 and S_1 distributions. For events in which S_2 and /or S_3 are defined, the signs of the significances are required to be the same as the sign of the S_1 significance. If this is not the case, the event is rejected.

Specifically, for jets contributing to the distribution of S_2 , it is required that the track with the first and the track with the second highest absolute significance have the same sign of δ. The reason for including the second highest significance is that it provides a greater separation power between heavy and light quarks. This can be observed in figure 6.9. In light quark events it is very unlikely that two tracks are produced at large significance due to resolution effects.

In order to reduce the uncertainty due to the resolution of δ and the light quark normalisation, the contents of the negative bins in the S_1, S_2 and S_3 distributions are subtracted from the contents of the corresponding positive bins. The subtracted distributions are shown in figure 6.10. It can be seen that the resulting distributions are dominated by *c* quark events, with a *b* quark fraction increasing towards the upper end of the distributions.

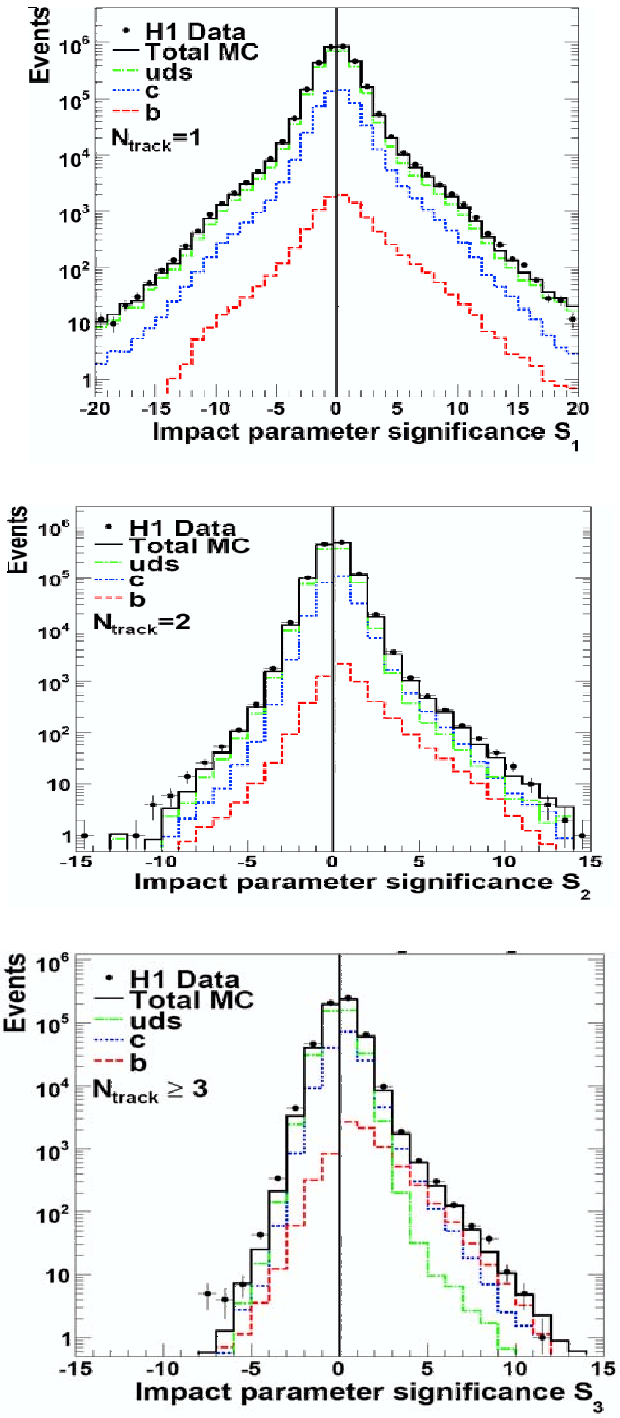

Figure 6.9: *The significance distribution (a) first significance, S_1 (b) second significance, $S_2$and (c) the third highest absolute significance S_3 of the selected tracks. Included in the figure is the expectation from Monte Carlo simulation for light, c and b quarks. The contributions from various quark flavours are shown after applying the scale factors (see section 6.3) obtained from the fit to the data.*

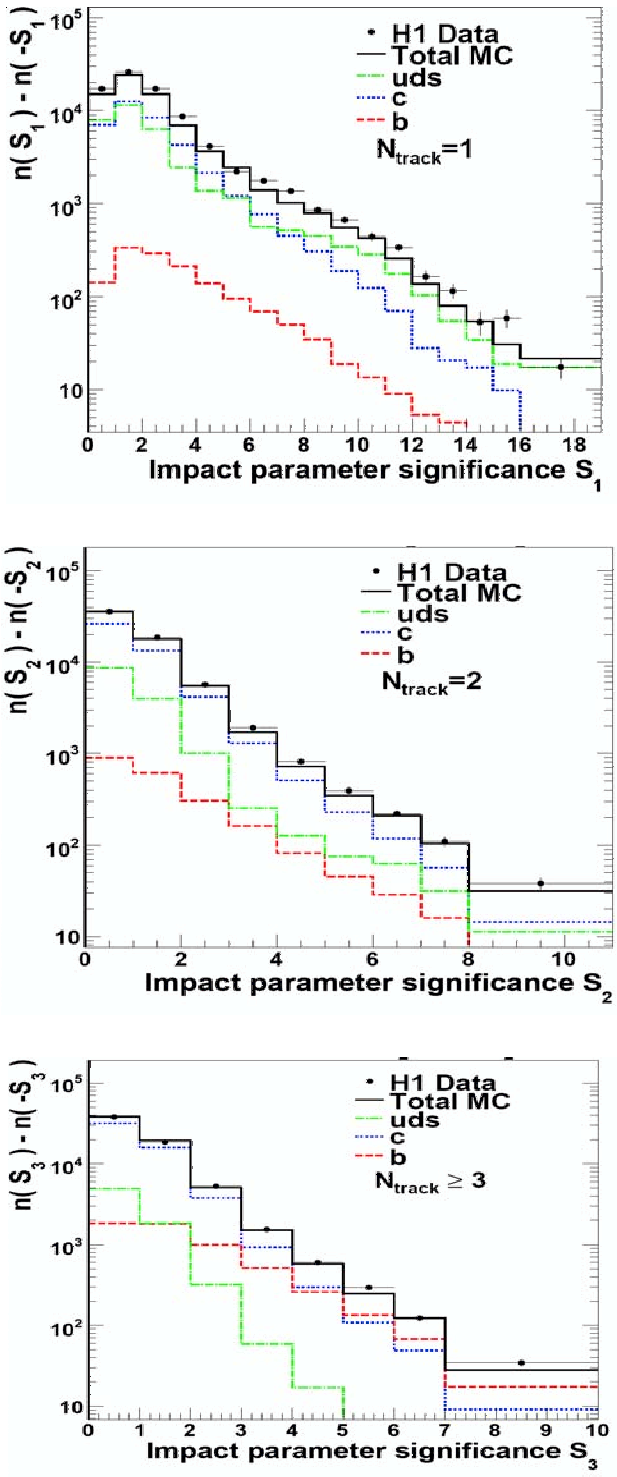

Figure 6.10: *The subtracted distributions of S_1, S_2 and S_3. The figures include the expectation from Monte Carlo simulation and show the different contribution from various quark flavours after applying the scale factors (see section 6.3) obtained from the fit to the data.*

The significance distributions were made for each individual P_T bin. Figure 6.11 shows the distribution for one of the bins.

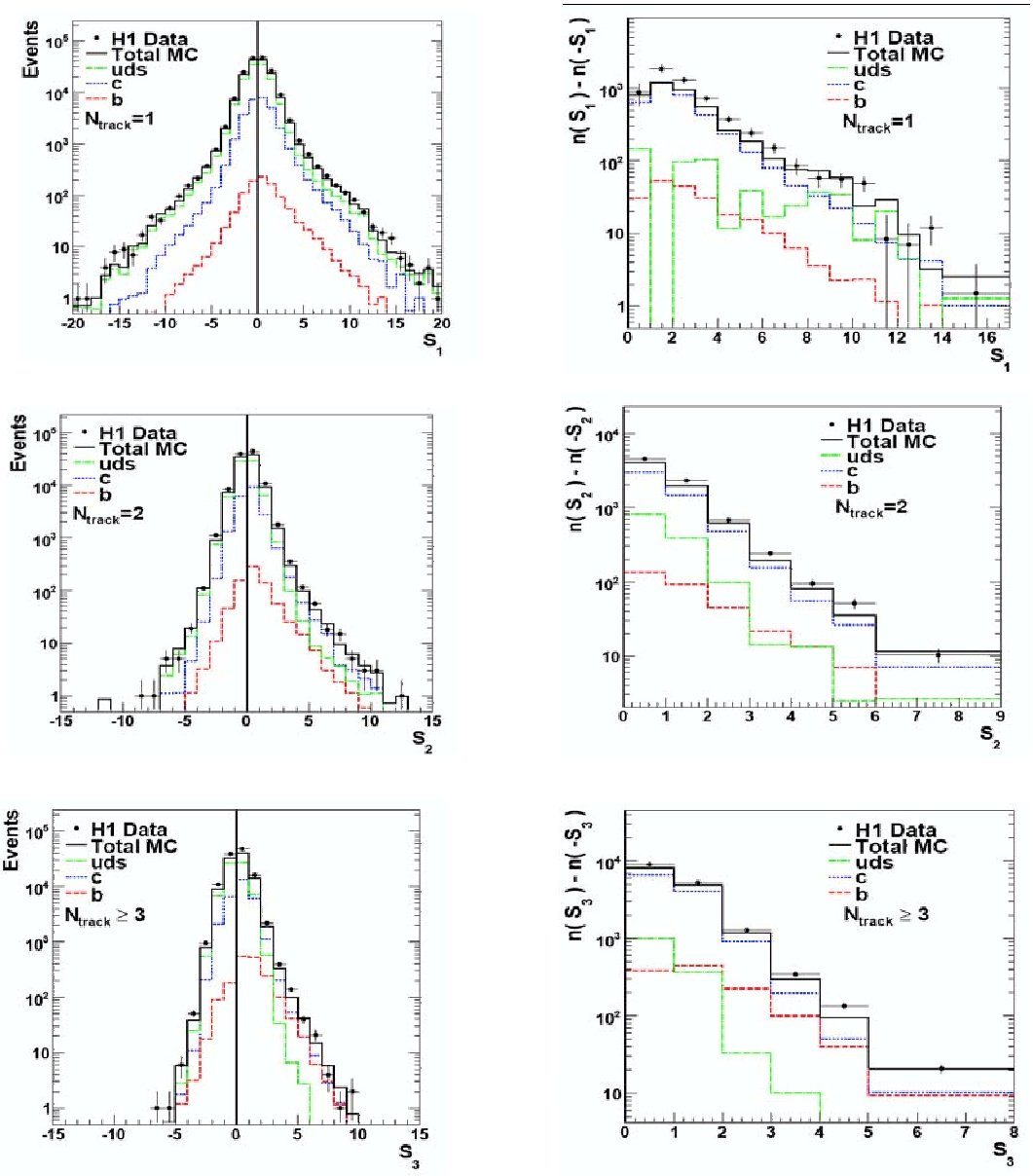

Figure 6.11: *The significance and the subtracted distributions of S_1, S_2 and S_3 for bin $6\ GeV > P_T > 8\ GeV$. The figures include the expectation from Monte Carlo simulation and show the contributions from various quark flavours after applying the scale factors obtained from the fit to the data.*

Although the S_2 distribution provides better separation between *charm* and *beauty*, events with only one selected CST track, the distributions from S_1 are retained to improve the statistical precision of the fit.

6.3 Fit Procedure

After performing the subtraction of negative bins from positive bins explained above, the number of events in the tails of the S_1 and S_2 distributions in data and Monte Carlo simulation is small. Therefore, in order to retain the Gaussian limit in the fit, bins with insufficient statistics are combined into larger bins in the subtracted significance distributions (cf. figure 6.10).

The charm, beauty and light quark fractions in the data are then extracted by simultaneously fitting the observed, subtracted S_1 and S_2 distributions and the total number of events before any CST track selection, N_{tot}^{data}. The Monte Carlo *b*, *c* and light quark distributions are used as shape templates and are allowed to be modified by the *scale factors* P_b, P_c and P_l, respectively, such that

$$\chi^2 = \sum_i \frac{(N_i^{data} - P_b N_{bi}^{MC} - P_c N_{ci}^{MC} - P_l N_{li}^{MC})^2}{\sigma^2(N_i^{data}) + (P_b\sigma(N_{bi}^{MC}))^2 + (P_c\sigma(N_{ci}^{MC}))^2 + (P_l\sigma(N_{li}^{MC}))^2} + \frac{(N_{tot}^{data} - P_b N_{totb}^{MC} - P_c N_{totc}^{MC} - P_l N_{totl}^{MC})^2}{\sigma^2(N_{tot}^{data}) + (P_b\sigma(N_{totb}^{MC}))^2 + (P_c\sigma(N_{totc}^{MC}))^2 + (P_l\sigma(N_{totl}^{MC}))^2}$$

is minimised. Here, with i runs over all bins of the subtracted S_1 and S_2 distributions and N_i^{data} is the number of events observed in the i^{th} bin. Only the statistical errors of the data and Monte Carlo simulation are taken into account.

The fit to the S_1 and S_2 distributions mainly constrains P_c and P_b, where the *c* and *b* quark fractions are distinguished by their different shapes. In contrast, the light quark normalisation is constrained by the total number of jet events without any track association. The results of the fit to the complete data sample are shown in figure 6.9. The fit gives a reasonable description of all the significance distributions, with a

$\chi^2/_{n.d.f}$ of 98/48. The number of the degrees of freedom (*n.d.f*) in the fit is the number of bins in the subtracted S_1 ,S_2 and S_3 distributions, plus one (for the total number of events), minus three for the free parameters of the fit (i.e. P_c, P_b and P_l).

The *c* and *b* scale factors are found to be anti-correlated with an overall correlation coefficient of -0.61. Consistent χ^2 values are also found for the fits to the samples when varying the number of P_T bins in the fit. The scale factors obtained from the fit to the complete data sample are;

$$P_l = 1.176 \pm 0.006$$

$$P_b = 1.001 \pm 0.025$$

$$P_c = 1.025 \pm 0.056 \qquad (6.2)$$

It can be seen from the distributions of subtracted S_1, S_2 and S_3 and the fit result in figure 6.10 that the distributions are dominated by charm events, with an increasing fraction of beauty quark events towards larger values of significance. The contribution from light quarks is seen to be small.

Chapter 7

"All things are subject to interpretation whichever interpretation prevails at a given time is a function of power and not truth."

Friedrich Nietzsche

"The truth is rarely pure and never simple."

Oscar Wilde

The Results

This chapter starts with a discussion on the process of the cross section extraction; the measured values for the cross sections are presented, followed by a discussion on hadronisation correction. Then a description of the systematic errors that have been considered in the final calculation of the results is followed. This chapter concludes with comparison of the results with the QCD models including NLO predictions of charm and beauty cross sections

7.1 The Cross Section

The collision or interaction of two particles is generally described in terms of the *cross section.*

This quantity is proportional to the probability for a reaction to occur and may be calculated if the form of the basic interaction between the particles is known. The cross section is a measure of the effective surface area seen by the impinging particles. In this

thesis, the cross sections are presented as a function of the transverse momentum and pseudorapidity of the leading jet. They are calculated for a total of six bins in P_T^{Jet} and four bins in η^{Jet}.

7.2 Determination of the Cross Sections

The jet production cross section can be measured by counting the number of measured events containing a jet (N^{data}) produced in the visible range correcting for detectors efficiencies and normalising to the corresponding integrated luminosity ($\mathcal{L}_{data}$) collected by the experiment

$$\sigma_{data}^{meas}(ep \longrightarrow ejX) = \frac{N^{data}}{\mathcal{L}_{data}.A} \quad . \tag{7.1}$$

The factor A in equation (7.1), represents the correction for detector efficiencies and acceptance. This includes contributions depending on geometry and limited resolution of the detector as well as on the selection cuts and the performance of the algorithms used for the reconstruction. The factor A is determined from the Monte Carlo simulation by dividing the number of reconstructed and generated events:

$$A = {N_{MC}^{rec}}\Big/{N_{MC}^{gen}} \, . \tag{7.2}$$

For Monte Carlo simulation the visible cross section is defined as

$$\sigma_{MC}^{vis}(ep \longrightarrow ejX) = \frac{N_{MC}^{gen}}{\mathcal{L}_{MC}} \tag{7.3}$$

with $\mathcal{L}_{MC}$ being the generated Monte Carlo luminosity. Combining equations 7.1 with equations 7.2 and 7.3 the measured cross section of data can be written as

$$\sigma_{data}^{meas}(ep \longrightarrow ejX) = \frac{N_{rec}^{data}\mathcal{L}_{MC}}{N_{MC}^{rec}\mathcal{L}_{data}} \times \sigma_{MC}^{vis}. \tag{7.4}$$

For the measurement of charm and beauty cross sections the first factor in equation 7.4 is the same as that of the scale factors P_b and P_c which are obtained from the fits of the subtracted impact parameter significance distributions to the data as explained in the previous chapter. i.e. $P_q = \frac{N_{rec}^{data}\mathcal{L}_{MC}}{N_{rec}^{MC}\mathcal{L}_{data}}$, where q is either c or b.

Therefore one can rewrite equation 7.4 in terms of these scale factors for charm and beauty:

$$\sigma^{meas}_{data_c}(ep \longrightarrow ej_cX) = P_c \times \sigma^{vis}_{MC\,c}$$
$$\sigma^{meas}_{data_b}(ep \longrightarrow ej_bX) = P_b \times \sigma^{vis}_{MC\,b} \quad . \qquad (7.5)$$

In making the measurements of the differential charm and beauty cross sections, the fit is performed separately in each bin *i*. Then the bin-integrated cross section prediction of RAPGAP Monte Carlo is multiplied with the resulting scale factors P_{c_i} and P_{b_i}, the product is divided by the respective bin size, to produce the differential cross section.
The cross sections are presented corrected to the level of stable hadrons (after decay of the heavy mesons) and in the phase space region defined by $4.5 < Q^2 < 1585\ \mathrm{GeV}^2$, $0.07 < y < 0.625$, $P_T^{Jet} > 6$ GeV and $|\eta^{Jet}| < 1.5$.

7.3 The Measured Differential Cross Sections

The measured differential cross sections as functions of transverse momentum (pseudorapidity) of the leading jet are shown in Figures 7.1 (7.2) as black points. The inner error bars in the figures indicate the statistical uncertainty and the outer error bars show the systematic and statistical errors added in quadrature. A description of the systematic errors and their evaluation is given in the next section. The histograms are predictions from the leading order Monte Carlo simulations and will be described in section 7.5.

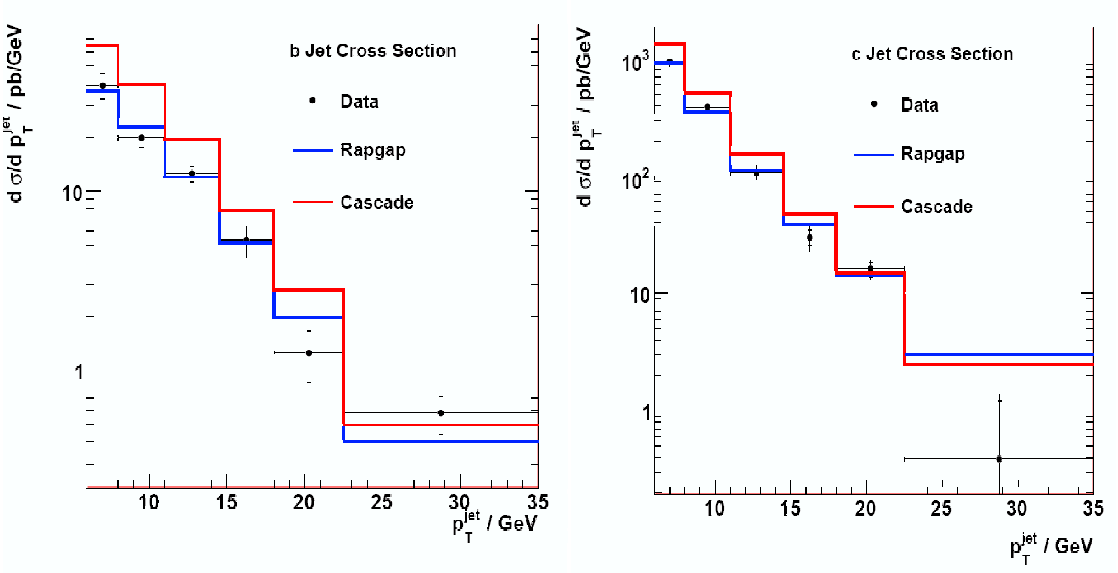

Figure 7.1 *Differential charm and beauty jets cross sections. The figure on the left (right) shows Beauty (Charm) jet cross section as a function of transverse momentum of the leading jet,* $d\sigma/dp_T$. *The solid black dots are the data points, the inner error bars indicate the statistical uncertainty and the outer error bars shows the statistical and systematic errors added in quadrature. The solid blue line (red) shows the expectations of the RAPGAP (CASCADE) Monte Carlo. As it can be observed from the plots, the data are well described by RAPGAP Monte Carlo in comparison to the CASCADE Monte Carlo expectation.*

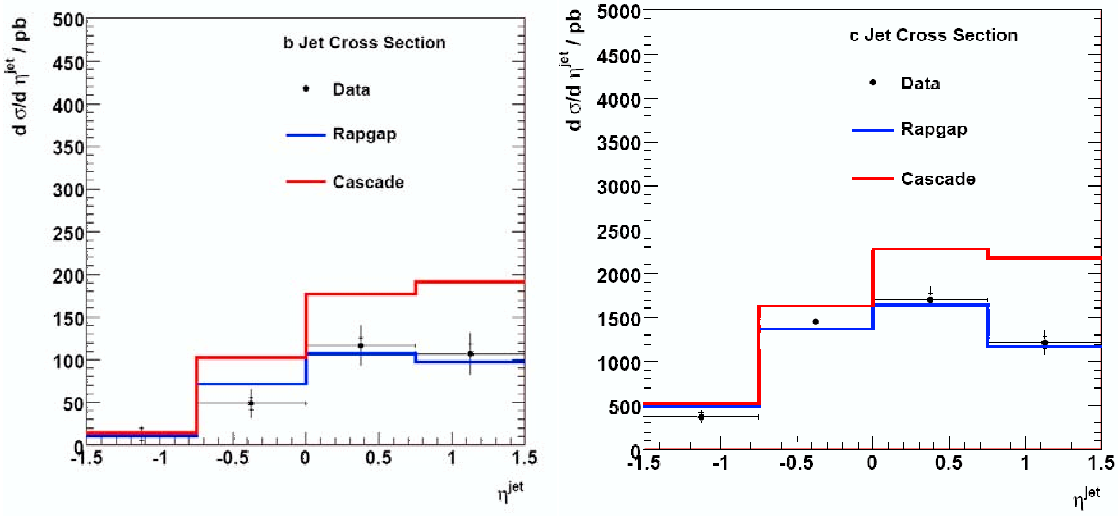

Figure 7.2: *Differential charm and beauty jets cross sections. The figure on the left (right) shows Beauty (Charm) jet cross section as a function of pseudorapidity of the leading jet,* $d\sigma/d\eta$. *The solid black dots are the data points, the inner error bars indicate the statistical uncertainty and the outer error bars shows the statistical and systematic errors added in quadrature. The solid blue line (red) shows the expectations of the RAPGAP (CASCADE) Monte Carlo.*

Numerical values for the differential cross section in individual bins of the transverse momentum of the leading jet are given in tables 7.1 and 7.2 for charm and beauty jets respectively. Corresponding numbers for the differential cross sections as functions of the pseudorapidity of the leading jet, are given in tables 7.3 for charm and 7.4 for beauty.
(For the numerical results of the differential cross section of charm and beauty jet as a function of the transverse momentum and pseudorapidity of the leading jet as predicted by the RAPGAP and CASCADE Monte Carlos, see Appendix A).

Charm						
P_T range [GeV]	$d\sigma/dp_T$ [Pb/GeV]	Stat error	Sys error	Total error	Had_{corr}	QED_{corr}
6 - 8	985.8	36.44	74.50	82.93	1.043	0.964
8 - 11	407.3	15.91	29.85	33.83	1.028	0.958
11 - 14.5	111.9	7.99	12.38	14.73	1.038	0.952
14.5 - 18	31.8	4.83	5.71	7.48	1.061	0.954
18 - 22.5	17.3	2.62	1.94	3.26	1.060	0.943
22.5 - 35	0.4	0.90	0.59	1.08	1.064	0.934

Table 7.1: *The measured differential cross section of charm jet together with statistic, systematic, and total errors for each individual P_T interval are listed. Also shown in the tables are the Hadronisation and QED correction factors for each P_T interval.*

Beauty						
P_T range [GeV]	$d\sigma/dp_T$ [Pb/GeV]	Stat error	Sys error	Total error	Had_{corr}	QED_{corr}
6 - 8	40.2	6.48	16.66	17.88	1.188	0.966
8 - 11	20.5	2.45	5.13	5.69	1.126	0.965
11-14.5	13.3	1.30	1.93	2.33	0.944	0.943
14.5-18	5.8	0.83	0.75	1.12	0.904	0.923
18 -22.5	1.4	0.43	0.33	0.54	0.907	0.927
22.5-35	0.6	0.15	0.08	0.17	0.953	0.962

Table 7.2: *The measured differential cross section of beauty jet together with statistic, systematic, and total errors for each individual P_T interval are listed. Also shown in the tables are the Hadronisation and QED correction factors for each P_T interval.*

Charm						
η range	$d\sigma/d\eta$ [Pb]	Stat error	Sys error	Total error	Had_{corr}	QED_{corr}
(-1.5) – (-0.75)	402.6	52.88	52.54	74.54	1.30	1.004
(-0.75) – (0.0)	1540.1	58.39	118.23	131.86	1.07	0.916
(0.0) – (0.75)	1778.5	65.87	140.01	154.73	1.02	0.943
(0.75) – (1.5)	1236.7	67.73	122.52	139.99	0.92	0.958

Table 7.3: *The measured differential cross section of charm jet together with statistic, systematic, and total errors for each individual η interval are listed. Also shown in the tables are the Hadronisation and QED correction factors for each corresponding η interval.*

Beauty						
η range	$d\sigma/d\eta$ [Pb]	Stat error	Sys error	Total error	Had_{corr}	QED_{corr}
(-1.5) – (-0.75)	13.5	8.02	7.44	10.94	2.31	0.902
(-0.75) – (0.0)	51.18	7.96	14.74	16.75	1.09	0.951
(0.0) – (0.75)	122.5	9.48	22.40	24.32	0.99	0.952
(0.75) – (1.5)	110.4	11.59	22.52	25.33	1.04	0.969

Table 7.4: *The measured differential cross section of beauty jet together with statistic, systematic, and total errors for each individual η interval are listed. Also shown in the tables are the Hadronisation and QED correction factors for each corresponding η interval.*

7.4 Systematic Errors

The systematic uncertainties on the measured cross sections are estimated by applying variations to Monte Carlo simulation. The following sources of systematic error have been considered:

DCA resolution: An uncertainty in the δ resolution of the tracks is estimated by varying the resolution by an amount that encompasses the differences between the data and simulation (cf. fig, 6.6, 6.10). This was achieved by applying an additional Gaussian smearing in the Monte Carlo simulation of 200μm to 5% of the randomly selected tracks and 12 μm to the rest. The significance distributions S_1, S_2 and S_3 are shown in figure 7.3 with the Monte Carlo expectation before (solid black lines) and after (red dashed lines) DCA smearing in linear (left figures) and logarithmic (right figures) scales.

Track efficiency: The reconstruction efficiency of CJC tracks is uncertain to the level of 1% [75]. As shown in figure 5.9 the CST track finding efficiency has an uncertainty of 2%. Hence the overall uncertainty on the track finding efficiency is 2.24%.

Errors associated with D and B meson production: The uncertainties on the various *D* and *B* meson lifetimes, decay branching fractions and mean charge multiplicities are estimated by varying the input values of the Monte Carlo simulation by errors on the world average measurements. For the branching fractions of *b* quarks to hadrons and the lifetimes of the *D* and *B* mesons the central values and errors on the world averages are taken from [76]. For branching fractions of *c* quarks to hadrons the values and uncertainties are taken from [77]. For the mean charged track multiplicities the values and uncertainties for *c* and *b* quarks are taken from MARKIII [78] and LEP/SLD [79] measurements, respectively.

Fragmentation function error: An uncertainty on the fragmentation function of the heavy quarks is estimated by repeating the fits with RAPGAP simulation in which the Bowler fragmentation function [80] is used for the longitudinal fragmentation instead of the Peterson function.

QCD model: An uncertainty on the QCD model of heavy quark production is estimated in the following way: The prediction from RAPGAP is reweighted up and then down (with weights that depend smoothly on P_T^{jet}) by the largest amounts that just maintain a reasonable description of the *shape* of the data distributions. The systematic errors are then taken to be the differences between these reweighted predictions and the original. A similar procedure was used for the systematic errors in the pseudorapidity distributions. Figure 7.4 shows the normalised differential cross sections as a function of transverse momentum and pseudorapidity of the leading jet together with the reweighted RAPGAP Monte Carlo predictions. It can be seen that the reweight function spans the error on the cross section. This procedure leads to errors of 4-10% for the charm and 6-25% for the beauty cross sections depending on the bin.

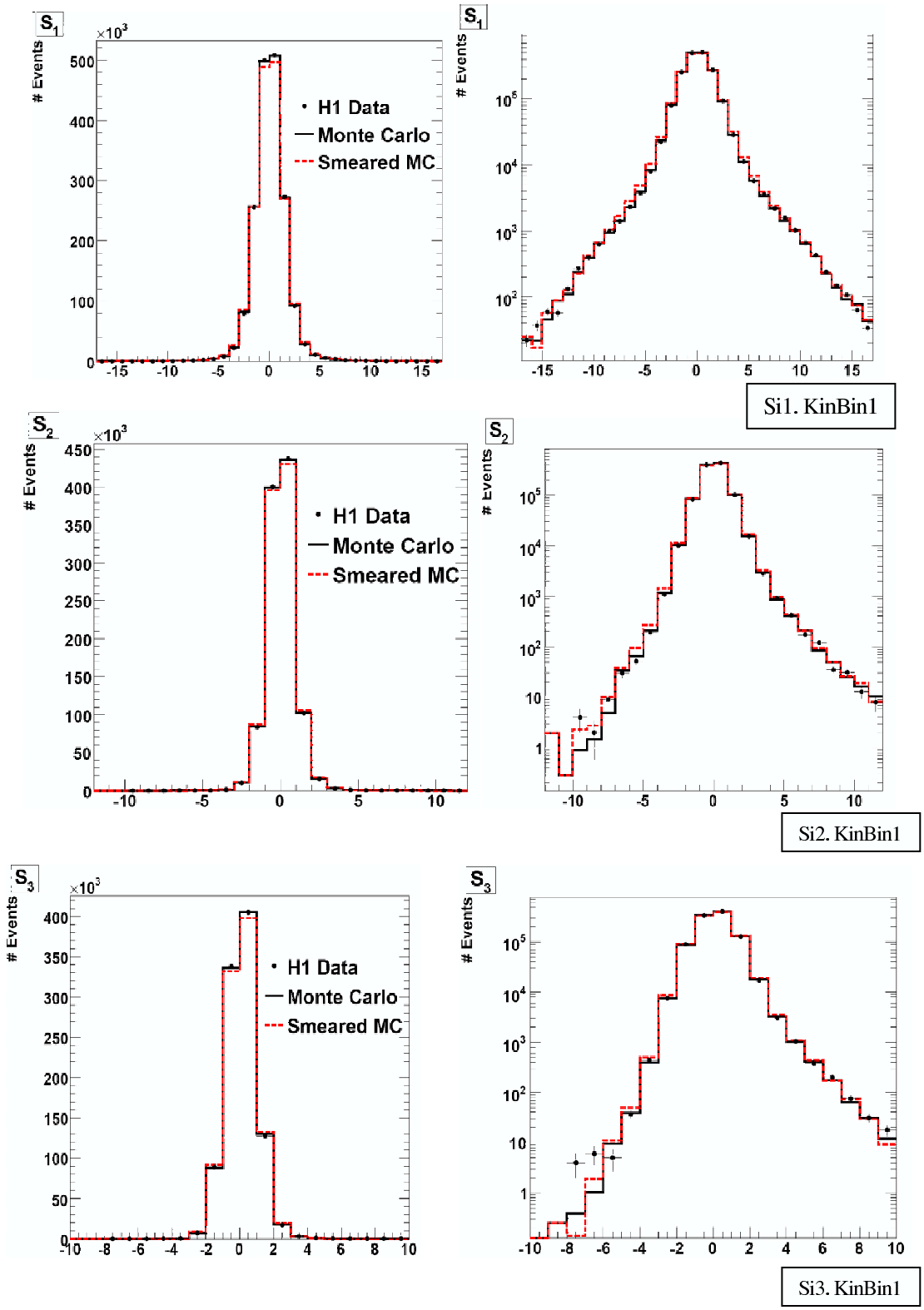

Figure 7.3: *The significance distributions S_1, S_2 and S_3 in linear (left figures) and logarithmic (right figures) scales for the interval $4 < P_T \leq 6$ GeV. The Monte Carlo expectations are also shown before (black lines) and after (red dashed lines) DCA smearing.*

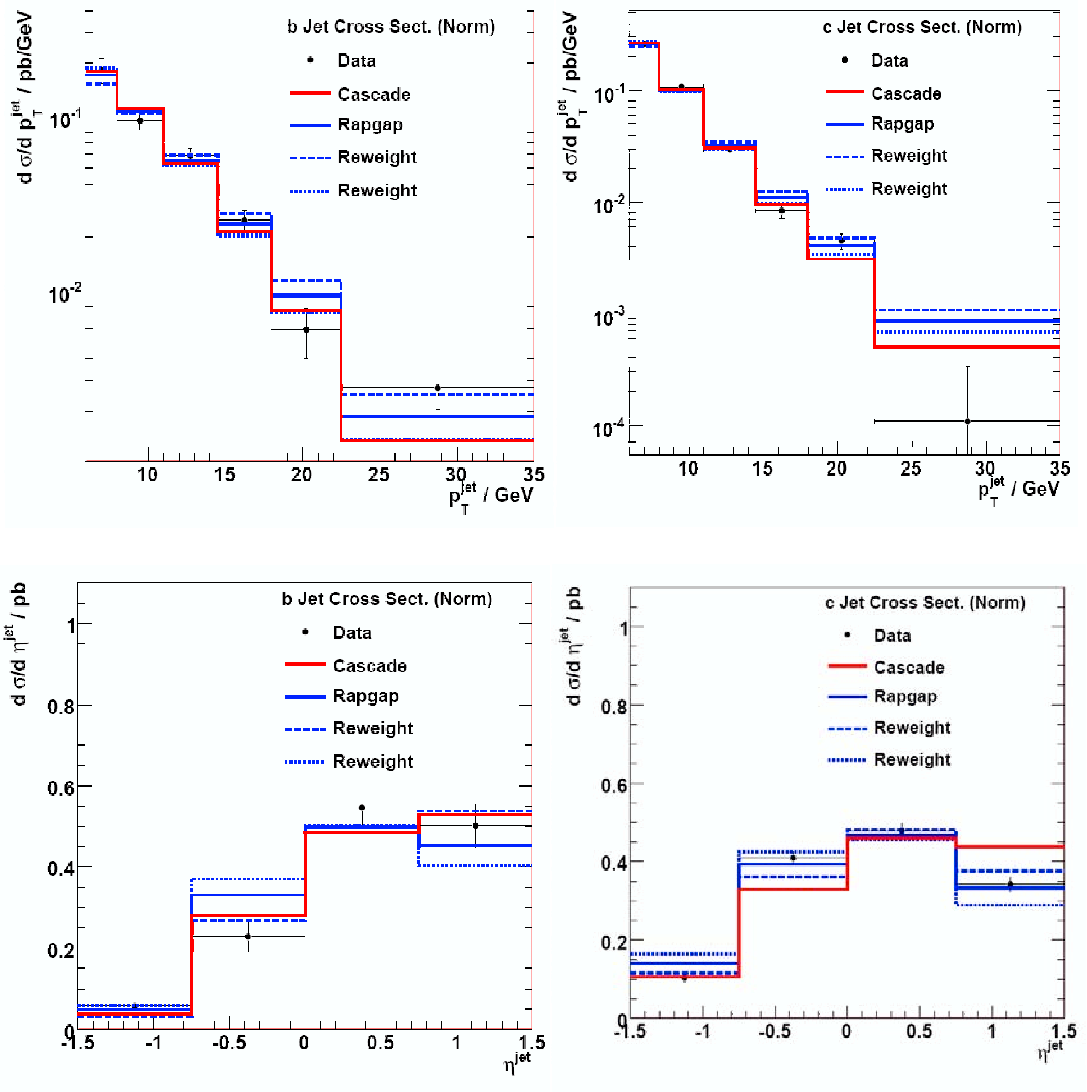

Figure 7.4: *Differential charm and beauty jets cross-sections normalised, so that the area under the curve is unity, as a function of the transverse momentum of the leading jet for beauty (top-left) and charm (top-right) Also shown are the normalised cross sections as a function of pseudorapidity of the leading jet for beauty (bottom-left) and charm (bottom-right). The solid black dots are the data points, the inner error bars indicate the statistical uncertainty and the outer error bars shows the statistical and systematic errors added in quadrature. The solid blue line (red) shows the expectations of the RAPGAP (CASCADE) Monte Carlo.*

Light quark DCA asymmetry: The uncertainty on the asymmetry of the light quark δ distribution is estimated by repeating the fits with the subtracted light quark significance distributions changed by $\pm 30\%$. The estimate was obtained by studying the light quark asymmetry in the region $0.1 < |\delta| < 0.5\ cm$, i.e. outside of the signal region, where the contribution to the distribution from light quarks is enhanced. In this region a clear K^0 peak at $m_{K^0} = 498$ MeV can be seen in the $\pi^+\pi^-$ mass spectrum. This is shown in figure 7.5 where the data (points) are compared with the Monte Carlo predictions (black histograms). The red dashed histograms show the result of varying the light quark contribution to the predictions by $\pm 30\%$ within which range, the prediction is still consistent with the data. The left and right figures show the distributions for e^-p and e^+p data separately.

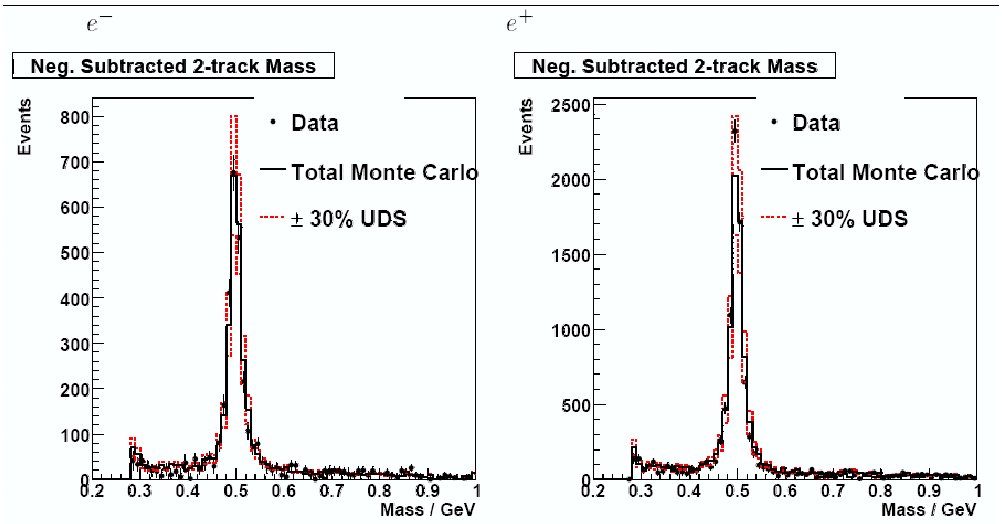

Figure 7.5: *The mass of two tracks for the negative subtracted events with* $0.1 < |\delta| < 0.5\ cm$ *for* e^-p *(*e^+p*) left (right). Also shown in the plots are the contribution from the variation of the expectation of Monte Carlo by* $\pm 30\%$.

Quark axis error: An error on the quark axis is estimated by shifting the quark axis by 2°(5°) for events with (without) a reconstructed jet. These shifts were estimated by comparing the difference between ϕ_{quark} and the track azimuthal angle in data and Monte Carlo simulation.

Hadronic energy scale: Since there is no in situ hadronic energy calibration to this data set, a 4% uncertainty on the hadronic energy scale is applied [58].

Other sources of systematic error pertaining to the NC selection were also considered [81]: a 1.5% uncertainty on the luminosity measurement; an uncertainty on the scattered positron polar angle of 0.3 mrad and energy of 0.3-1.0% depending on the energy; a 0.5% uncertainty on the scattered positron identification efficiency; a 0.5-2% uncertainty on the positron track cluster link efficiency; a 1% uncertainty on the tigger efficiency and uncertainty on the cross section evaluation due to the QED radiative corrections(cf. tables 7.1 – 7.4).
Table 7.5 summarises the main systematic errors.

Source	Uncertainty	Error $c\bar{c}$ /	Error $b\bar{b}$ /
Track efficiency	$\pm 2.22\%$	1-2.5	6-20
DCA resolution	$\pm 12\ \mu m (\pm 200 \mu m\ tails)$	1-5	1-8
uds asymmetry	30% uncertainty	4-15	2-30
Fragmentation	Bowler/Lund	1-10	2-11
QCD model	P_T/η	4-10	6-25
Had Scale	4%	0-4	0-5
Jet(HFS)Axis	2°(5°) shift	1-10	1-10
B Multiplicity	LEP / SLD	0-1	3-5
D Multiplicity	MARKIII	2-3	2-10
total		9-25	14-45

Table 7.5: *The systematic errors.*

7.5 Comparison with Leading Order Models

The data in Figures 7.1 and 7.2 are compared with the predictions from the RAPGAP and CASCADE Monte Carlo simulations.

As explained in more detail in Chapter 3, RAPGAP [51] is an event generator based on the combination of exact leading-order (LO) matrix elements with higher-order QCD radiation simulated in the form of initial and final-state parton showers. The latter are simulated in the leading-logarithmic approximation based on the DGLAP evolution equations [32]. For this analysis, the CTEQ5F3 parameterisation of the proton parton densities was used. Production of $b\bar{b}$ and $c\bar{c}$ pairs via photon-gluon fusion (PGF) is used to simulate the signal. Charm and beauty masses were set to 1.5 GeV and 4.75 GeV, respectively. Heavy-quark hadronisation was modelled by Bowler fragmentation function [80]. The rest of the hadronisation was simulated using the Lund string model [89] as implemented in JETSET [53]. The RAPGAP MC also includes the LO electroweak corrections calculated using the HERACLES program [54].

The CASCADE MC [52] also uses $\mathcal{O}(\alpha_s)$ matrix elements but allows the incoming partons to be off-shell and the parton evolution is based on the CCFM equations [36]. The latter are derived from the principles of K_T factorisation and colour coherence.

It is clear from the figures that the RAPGAP LO prediction (blue histogram in Figures 7.1 and 7.2) gives a good overall description of the data in all four differential cross sections. The CASCADE predictions on the other hand do not describe the data within errors and tend to overestimate the data everywhere. Furthermore they give the wrong shape for the pseudorapidity distributions predicting too high a cross section in the forward, positive pseudorapidity region. These remarks apply to both the charm and the beauty differential cross sections.

7.6 Next-to-Leading Order Calculations

Comparison of the Standard Model with the measurements of the NC *ep* cross-sections depends both on the model's explicit predictions for the interaction of a positron (electron) with a quark and the partonic content of the proton. The parameters of the electroweak

theory which describes positron (electron)-quark scattering in the Standard Model have been measured precisely, and are therefore fixed to their world average values [76] in this comparison. The parton distribution functions (PDFs), which describe the partonic structure of the proton, are not predicted by QCD and so must be obtained from the data. PDFs together with their uncertainties are available from global NLO QCD fits to the data performed by various groups including the CTEQ group whose PDF's are used here.

The NLO predictions were calculated with the MC integration package HVQDIS [45] using the CTEQ5F3 PDF set ($\alpha_s(M_z^2) = 0.108$). The NLO QCD expectation is calculated from the results of fit similar to that performed in [88] but using the FFNS scheme with 3 flavours to generate heavy flavour quarks.
The theoretical uncertainties in the NLO calculations were estimated by varying the renormalisation and factorisation scales from their default values, set to $\mu_r^2 = \mu_f^2 = (m_h^2 + P_T^2)$, by factors of four up and down. Here m_h denotes *c* or *b* quark mass.

The theory calculations of the cross sections presented in this chapter produce cross sections on the parton level whereas the cross sections extracted from the data are at the stable hadron level, corrected only for the effects of detector acceptance and efficiency.
Therefore in order to compare the theory calculations with the data, correction factors from parton to hadron level must be applied to each bin of the theoretical prediction. The correction factors were determined the LO RAPGAP Monte Carlo. The hadronisation correction factors are given by the ratio of the cross sections obtained with jets as reconstructed from hadrons after the full event simulation and from jets as reconstructed from partons after parton showers but before hadronisation. An estimate of the NLO hadron level cross sections is thus given by:

$$NLO\ (Hadron\ Level) \cong NLO\ (Parton\ Level) \times \frac{RAPGAP(Hadron\ level)}{RAPGAP(Parton\ Level)}$$

The numerical results for this correction can be found in Tables 7.1-7.4.

For a detailed discussion on the need for QED radiative correction see section 3.2.6. The numerical values for these corrections are shown in tables 7.1-7.4, the numbers are also listed in Appendix A.

Figure 7.6 shows comparisons of the measured charm and beauty differential cross sections with the NLO predictions. The figures show the prediction both uncorrected for hadronisation (blue dashed histogram) and with the hadronisation corrections (red histograms). The hadronisation corrections clearly improve the description of the data, especially at lowP_T and low pseudorapidity of the leading jet. The dotted and dash-dotted red histograms show the result of varying the scale on the NLO prediction.

In both charm and beauty jet differential cross sections as functions of transverse momentum of the leading jet the NLO prediction shows reasonable agreement with the data. The data lies within the boundary of the theory uncertainty band in majority of the bins. Deviations, where the data is lower and outside the theoretical uncertainty, are seen in the highest P_T bin of the charm differential cross section and in the penultimate bin of the beauty cross section. Similar good agreement can be observed in the differential cross sections of charm and beauty jets as functions of pseudorapidity. Exceptions are the second bin for beauty where the NLO prediction overestimates the data and the third and last bins in the charm distribution where it underestimates it. Nevertheless, the overall shapes of the distributions are remarkably akin to those of the NLO predictions.

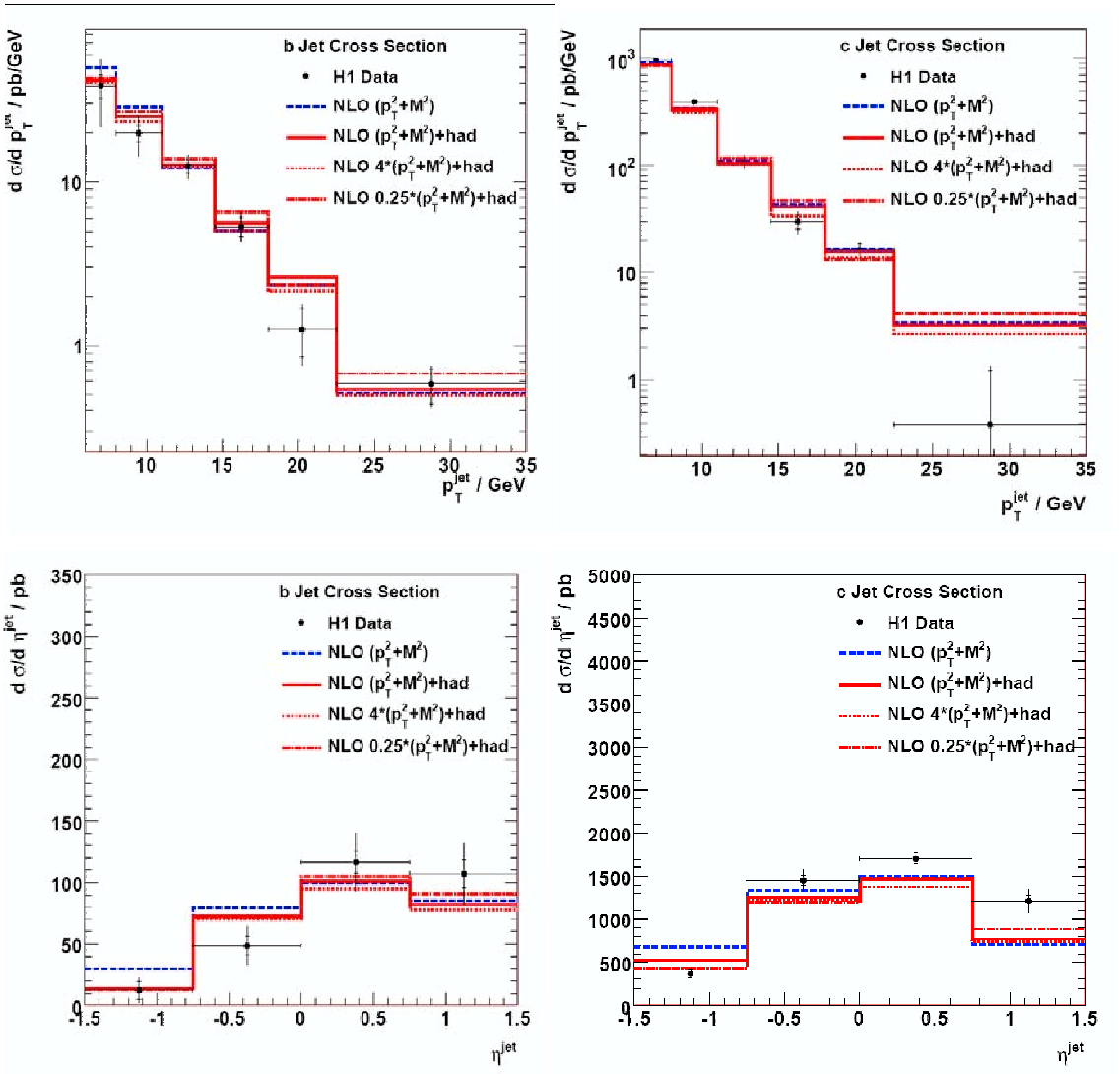

Figure 7.6: *Predictions of the NLO calculation with (red lines) and without (blue) hadronisation corrections applied are compared with the measured differential cross sections as functions of P_T for beauty jets (top-left) and for charm jets (top-right) and with $d\sigma/d\eta$ for beauty jets (bottom-left) and charm jets (bottom-right). The figure also shows the NLO predictions after varying the scales $\mu_r^2 = \mu_f^2 = (m_h^2 + P_T^2)$ by factors of 4 (red dotted lines) and ¼ (red dash-dotted lines).*

Chapter 8

"Non ominia possumus omnes."

Virgil

Summary and Conclusion

Data collected by the H1 experiment at HERA during the years 2006 and 2007 (HERA II data) were used to measure the cross sections for charm and beauty jets in neutral current deep inelastic scattering in $e^{\pm}p$ collisions. The data set used is based on an integrated luminosity of 189pb^{-1} with an $e^{\pm}p$ centre-of- mass energy of$\sqrt{s} = 319$ GeV. A method, based on the distance of closest approach of the track to the primary vertex, is used to separate charm and beauty flavoured mesons from the light quarks. The inclusive K_T algorithm was employed to define jets, which were clustered in the laboratory frame of reference.

The differential jet cross-sections were measured with respect to transverse momentum, P_T^{Jet}, and pseudorapidity, η^{jet},of the leading jet and the results are tabulated in the previous chapter and Appendix A.

Overall, the measured charm and beauty distributions have shapes that are similar to each other in all variables considered indicating that the kinematic effects due to different quark masses are small in the phase space studied.

The measured cross sections were compared with QCD models as implemented in the leading order plus parton shower Monte Carlo simulation programs RAPGAP and CASCADE and in the massive next-to-leading order (NLO) program HVQDIS. The theoretical predictions of perturbative Quantum Chromodynamics agree with the data within the quoted uncertainties across a wide range of the phase space considered. It has been also demonstrated that by using lifetime and significance information one can

measure the cross section of a single jet, without looking for additional information in the decay products such as the presence of a muon and a jet.

The understanding of the gluon and quark distributions in the region of low x has important implications for measurements of the standard model and new physics processes at Large Hadron Collider (LHC).

Further investigation and study of the production mechanism of heavy flavour quarks using the full cumulative data for H1 and ZEUS (combined H1-Zeus) and more precise testing of the various QCD models will lead to a reduction in the statistical and systematic uncertainties in the data. This would be particularly useful for the LHC.

Appendices

Appendix A	**Tables of Results**	**156**
Appendix B	**Reconstruction Methods**	**160**
Appendix C	**Running Coupling Constant**	**163**
Appendix D	**Example Events in the H1 Detector**	**166**

Appendix A

Tables of Results

P_T range [GeV]	$d\sigma/dp_T$ [Pb/GeV] RAPGAP		$d\sigma/dp_T$ [Pb/GeV] CASCADE	
	Charm	Beauty	Charm	Beauty
6 - 8	955.3	37.7	1382.6	67.5
8 - 11	364.1	23.6	531.7	41.0
11 - 14.5	116.9	12.6	159.7	20.6
14.5 - 18	40.8	5.5	50.2	8.4
18 - 22.5	15.1	2.1	16.2	3.0
22.5 - 35	3.3	0.4	2.7	0.5

Table A.1: *The expectation of RAPGAP Monte Carlo and CASCADE MC for cross section of charm jet for each individual P_T interval are listed.*

η range	$d\sigma/d\eta$ [Pb] RAPGAP		$d\sigma/d\eta$ [Pb] CASCADE	
	Charm	Beauty	Charm	Beauty
(-0.15) – (-0.75)	534.3	11.6	573.7	15.4
(-0.75) – (0.0)	1456.1	75.1	1735.6	107.7
(0.0) – (0.75)	1712.1	112.7	2383.2	185.6
(0.75) – (1.5)	1188.2	100.7	2218.3	197.9

A.2: *The expectation of RAPGAP Monte Carlo and CASCADE MC for differential cross section of charm jet for each individual η interval are listed.*

The results in Tables A.3-A.6 are already shown in chapter 7. They are reproduced here for completeness.

Charm						
P_T range [GeV]	$d\sigma/dp_T$ [Pb/GeV]	Stat error	Sys error	Total error	Had_{corr}	QED_{corr}
6 - 8	985.8	36.44	74.50	82.93	1.043	0.964
8 - 11	407.3	15.91	29.85	33.83	1.028	0.958
11 - 14.5	111.9	7.99	12.38	14.73	1.038	0.952
14.5 - 18	31.8	4.83	5.71	7.48	1.061	0.954
18 - 22.5	17.3	2.62	1.94	3.26	1.060	0.943
22.5 - 35	0.4	0.90	0.59	1.08	1.064	0.934

Table A.3: *The measured differential cross section of charm jet together with statistic, systematic, and total errors for each individual P_T interval are listed. Also shown in the tables are the Hadronisation and QED correction factors for each P_T interval.*

Beauty						
P_T range [GeV]	$d\sigma/dp_T$ [Pb/GeV]	Stat error	Sys error	Total error	Had_{corr}	QED_{corr}
6 - 8	40.2	6.48	16.66	17.88	1.188	0.966
8 - 11	20.5	2.45	5.13	5.69	1.126	0.965
11-14.5	13.3	1.30	1.93	2.33	0.944	0.943
14.5-18	5.8	0.83	0.75	1.12	0.904	0.923
18 -22.5	1.4	0.43	0.33	0.54	0.907	0.927
22.5-35	0.6	0.15	0.08	0.17	0.953	0.962

Table A.4: *The measured differential cross section of beauty jet together with statistic, systematic, and total errors for each individual P_T interval are listed. Also shown in the tables are the Hadronisation and QED correction factors for each P_T interval.*

Charm						
η range	$d\sigma/d\eta$ [Pb]	Stat error	Sys error	Total error	Had_{corr}	QED_{corr}
(-1.5) – (-0.75)	402.6	52.88	52.54	74.54	1.30	1.004
(-0.75) – (0.0)	1540.1	58.39	118.23	131.86	1.07	0.916
(0.0) – (0.75)	1778.5	65.87	140.01	154.73	1.02	0.943
(0.75) – (1.5)	1236.7	67.73	122.52	139.99	0.92	0.958

Table A.5: *The measured differential cross section of charm jet together with statistic, systematic, and total errors for each individual η interval are listed. Also shown in the tables are the Hadronisation and QED correction factors for each corresponding η interval.*

Beauty						
η range	$d\sigma/d\eta$ [Pb]	Stat error	Sys error	Total error	Had_{corr}	QED_{corr}
(-1.5) – (-0.75)	13.5	8.02	7.44	10.94	2.31	0.902
(-0.75) – (0.0)	51.18	7.96	14.74	16.75	1.09	0.951
(0.0) – (0.75)	122.5	9.48	22.40	24.32	0.99	0.952
(0.75) – (1.5)	110.4	11.59	22.52	25.33	1.04	0.969

Table A.6: *The measured differential cross section of beauty jet together with statistic, systematic, and total errors for each individual η interval are listed. Also shown in the tables are the Hadronisation and QED correction factors for each corresponding η interval.*

Appendix B

Reconstruction Methods

The measurements of the products of NC DIS events at H1 allow different methods of reconstruction of the kinematic variables that define the event. These methods differ in resolution for each variable due to the different precision with which each component quantity can be measured. There is redundancy between the methods that allows methods to be combined in order to obtain the best resolutions for as many variables as possible.

B.1 The Electron Method

The kinematics describing a DIS event may be described using information from the scattered electron alone [56]. If the energy of the incident electron, E, the scattered electron energy ,E′, and the polar angle of the scattered electron, θ, are known, for example in a well measured neutral current DIS event, the kinematics may be defined as follows:

$$Q_e^2 = 4EE'\cos\left(\frac{\theta^2}{2}\right) \qquad y_e = 1 - \frac{E'}{2E}(1 - cos\theta) \qquad x_e = \frac{Q_e^2}{sy_e} \tag{B.1}$$

The Electron Method gives excellent resolution for the variable Q^2 but the resolution of y decreases at low values of y.

B.2 The Double Angle Method

The Double Angle (DA) Method [56] utilises the angles of the scattered electron and the hadronic final state to reconstruct the kinematic variables, as follows:

$$\Upsilon Q^2_{DA} = 4E^2 sin\gamma(1 + cos\theta) \qquad \Upsilon y_{DA} = sin\theta(1 - cos\gamma) \qquad x_{DA} = \frac{Q^2_{DA}}{s y_{DA}} \qquad \text{(B.2)}$$

where γ is the polar angle of the hadronic system and $\Upsilon = \sin\gamma + \sin\theta - \sin(\theta + \gamma)$. This method is insensitive to the absolute calorimeter energy calibration, but sensitive to the relative calibration between different sections of the detector. The Double Angle Method is not employed in this work except as a means to calibrating the electromagnetic and hadronic energy scales of the calorimeters.

B.3 The Sigma Method

The Sigma Method [57] uses information from both the hadronic final state and the scattered electron to reconstruct the kinematics as follows:

$$y_\Sigma = \frac{\Sigma}{E - P_z} \qquad Q^2_\Sigma = \frac{(E' \sin\theta)^2}{1 - y_\Sigma} \qquad x_\Sigma = \frac{Q^2_\Sigma}{s y_\Sigma} \qquad \text{(B.3)}$$

where $\sum = \sum_{i \neq e} E_i - P_{z,i}$ and $E - P_z = \sum_i E_i - P_{z,i}$. The former sum is over the entire hadronic final state, excluding the scattered electron, *e*. This method has reduced sensitivity to QED radiation from the incoming electron as for the initial beam energy does not feature in the definition. It is best suited for determination of the value *x*.

B.4 The Electron-Sigma Method

The Electron-Sigma Method [57] combines the excellent Q^2 resolution of the Electron Method with the precision x determination from the Sigma Method. It is defined as follows:

$$Q^2_{e\Sigma} = Q^2_e \qquad x_{e\Sigma} = x_\Sigma \qquad y_{e\Sigma} = \frac{Q^2}{sx_{e\Sigma}} \tag{B.4}$$

The Electron-Sigma Method is utilised for the kinematic reconstruction throughout this analysis.

Appendix C

Running Coupling Constant

C.1 Introduction

A physical interpretation of the running coupling can be seen by considering one of the similarities of QCD with QED- the effect known as *charge screening*.

However, one of the main differences between QED and QCD- is, that the exchanged bosons are themselves charged has an effect on the way the "charge screening" functions. QCD also features screening effects but due to the interaction of gluons with each other and because gluons carry away colour charge from the quark(both effects due to their coloured status) the higher-order effects contain additional loops. This has the effect that, as an incident probe penetrates closer to the "bare" charge, it sees ever decreasing amounts of colour and so the measured colour charge decreases. As in QED, this is well described by a running coupling; in this case $\alpha_s(Q^2)$.

From renormalisation arguments the running of the coupling constant α_s with some external energy μ^2 is given by the Callan-Symanzik β function,

$$\frac{d\alpha_s(\mu^2)}{dln\mu^2} = \beta(\alpha_s). \qquad \text{(C.1)}$$

If we introduce some arbitrary energy scale μ_0 at which we chose to renormalize our theory, then if the value of our coupling at μ_0 is given by $\alpha_s(\mu_0^2)$, we obtain the solution

$$ln\,\mu^2 - ln\,\mu_0^2 = \int_{\alpha_s(\mu_0^2)}^{\alpha_s(\mu^2)} \frac{dx}{\beta(x)} \qquad \text{(C.2)}$$

$$= F(\alpha_s(\mu^2)) - F\big(\alpha_s(\mu_0^2)\big). \qquad \text{(C.3)}$$

However the value of $\alpha_s(\mu^2)$ should be independent of our choice of scale μ_0 and so we obtain

$$\ln \mu^2 - F(\alpha_s(\mu^2)) = \ln\ \mu_0^2 - F\big(\alpha_s(\mu_0^2)\big) = C \qquad \text{(C.4)}$$

where C is some constant. From this we obtain

$$\alpha_s(\mu^2) = F^{-1}(\ln \frac{\mu^2}{\mu_0^2} + F\big(\alpha_s(\mu_0^2)\big). \qquad \text{(C.5)}$$

We must now eliminate any dependence on the arbitrary scale μ_0 which can be done by defining a new scale parameter , Λ, such that

$$F\big(\alpha_s(\mu_0^2)\big) = \ln \frac{\mu_0^2}{\Lambda^2} \qquad \text{(C.6)}$$

and that

$$\alpha_s(\mu^2) = F^{-1}(\ln \frac{\mu^2}{\Lambda^2}) \qquad \text{(C.7)}$$

where Λ has to be evaluated experimentally.

C.2 $\boldsymbol{\alpha_s(\mu^2)}$ at Leading Order

Specialising to QCD, the leading order (LO) Callan-Symanzik β function [90] is given by

$$\frac{d\alpha_s(\mu^2)}{d\ln\mu^2} = -b_0\alpha_s^2(\mu^2) \qquad \text{(C.8)}$$

where $b_0 = (33 - 2nf)/12\mu$. Integrated (C.8) leads to

$$\int_{\mu_0^2}^{\mu^2} dt\ \frac{1}{t} = -\int_{\alpha_s(\mu_0^2)}^{\alpha_s(\mu^2)} dx\ \frac{1}{b_0 x^2}$$

$$\ln \mu^2 - \ln \mu_0^2 = \frac{1}{b_0 \alpha_s(\mu_0^2)} \tag{C.9}$$

$$\equiv F(\alpha_s(\mu^2)) - F\big(\alpha_s(\mu_0^2)\big). \tag{C.10}$$

This gives

$$\alpha_s(\mu^2) = \frac{1}{b_0 \ln\left({}^{\mu^2}/_{\Lambda^2}\right)} \tag{C.12}$$

If we define $\tau = \ln \mu^2/\Lambda^2$ then at LO, equation C.11 becomes $\alpha_s(\mu^2) \equiv \alpha_s(\tau) = 1/b_0\tau$. However, at leading order the choice of constant Λ used for the definition of α_s is not uniquely specified. In fact at two similar momentum scales μ and μ' we can expand the coupling $\alpha_s\big(\mu'^2\big)$ at μ' as a series about $\alpha_s(\mu^2)$ at μ.

$$\frac{1}{\alpha_s(\mu'^2)} = \frac{1}{\alpha_s(\mu^2)} - b_0 ln \frac{\mu^2}{\mu'^2} \tag{C.13}$$

which implies that

$$\alpha_s\big(\mu'^2\big) = \alpha_s(\mu^2)\left[\, 1 - \alpha_s(\mu^2) b_0 ln \frac{\mu^2}{\mu'^2}\right]^{-1} \tag{C.14}$$

This results in [91]

$$\alpha_s\big(\mu'^2\big) = \alpha_s(\mu^2)\left[\, 1 + \alpha_s(\mu^2) b_0 ln \frac{\mu^2}{\mu'^2} + \mathcal{O}(\alpha_s^2)\right], \tag{C.15}$$

and so to leading order in α_s we see that $\alpha_s(\mu^2)$ and $\alpha_s\big(\mu'^2\big)$ are identical, so the scales μ and μ' are equivalent and Λ cannot be defined uniquely.

Appendix D

Example Events in the H1 Detector

The following are examples taken from the H1 event display. They are for illustrative purposes only. Several of these example event pictures were selected by J.Meyer as part of the H1 event tutorial which is available at (http://www-h1.desy.de/pictures/H1-event.tutorial.pdf).

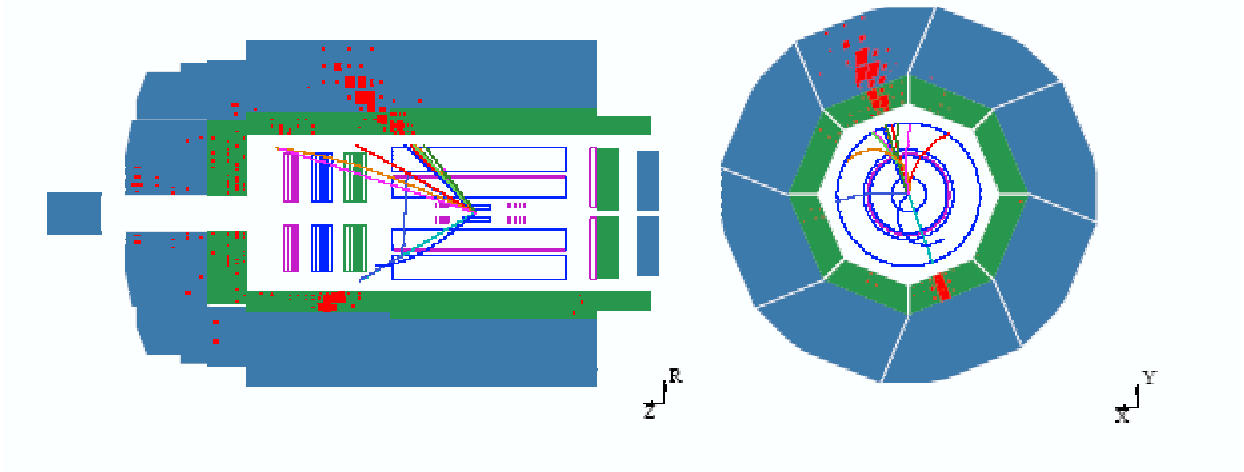

Figure D.1: Shows an example of a NC event with high Q^2 in the H1 Detector from HERA II data taking period.

Examples of events from non-*ep* background processes are shown in figure D.2 (halo-muon and cosmic muon events) and figure D.3 (beam-gas interaction). Such events are taken out by dedicated background finders and their remaining contamination to the NC sample is essentially zero.

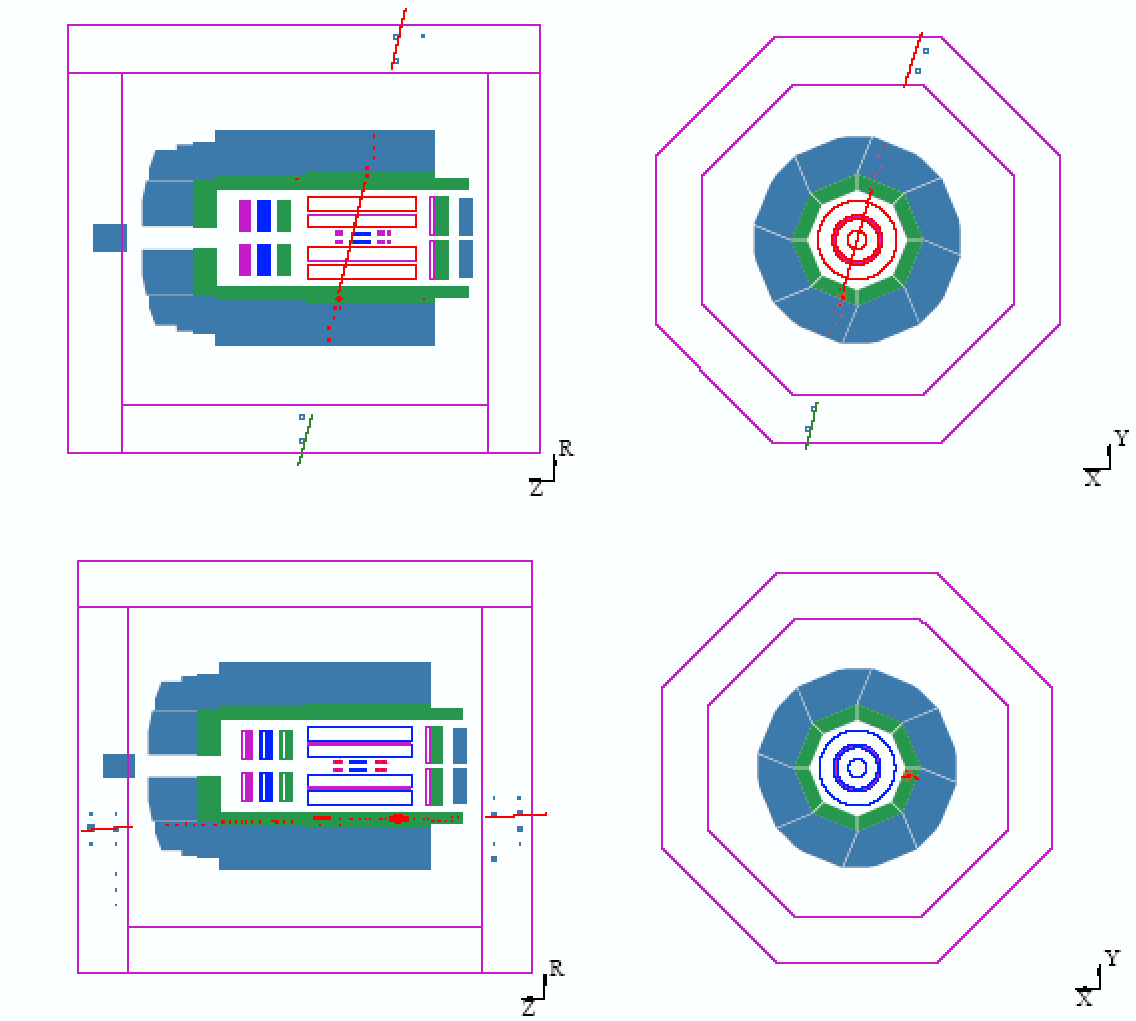

Figure D.2: Cosmic (top) and halo-muon (bottom) events in H1 Detector.

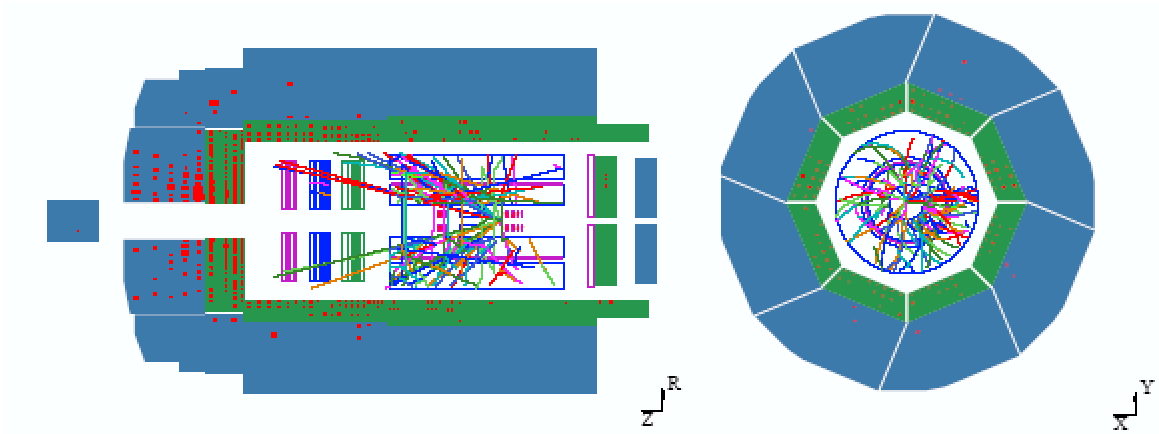

Figure D.3: Beam-gas event in the H1 detector.

Figure D.4 shows the precision of the CST in measuring the decay lengths from primary vertex to secondary vertex, which is very crucial in the current analysis for distinguishing the heavy flavour quarks from the light quark background and to discriminate between the decay length of charm and beauty, the latter will have a longer decay length due to its mass.

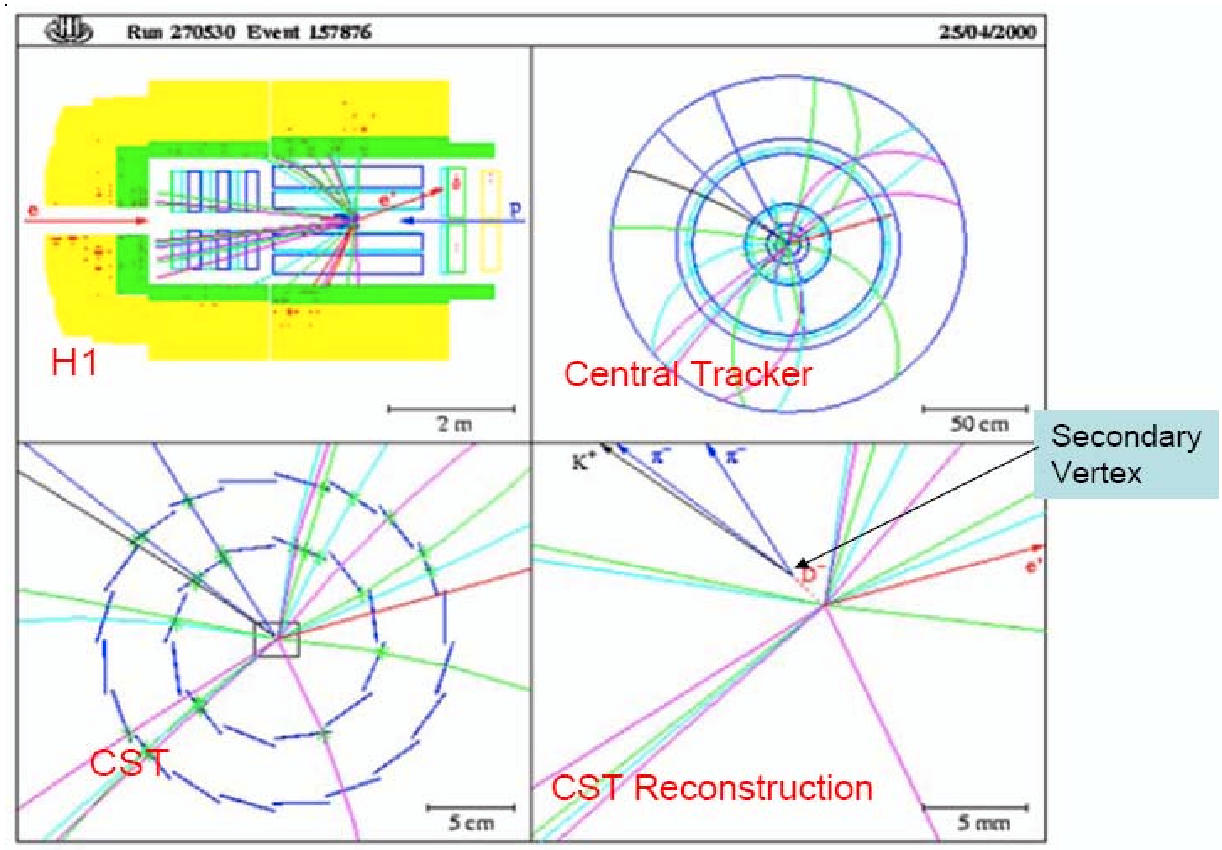

Figure D.4: Shows the precision of the Central Silicon Detector (CST), which measures the hits very precisely (10 micometer) which in turn is instrumental in search for the decay length or secondary vertices of the heavy quark (charm, bottom) decays, the event is from HERA I data taking period.

Figure D.5 shows a NC DIS events with single jet, the interaction region can be clearly identified at the centre of the detector (central silicon detector) and the by products of the interaction, i.e. scattered electron with its energy deposition in Electromagnetic

calorimeter and the hadronic final state particles (jet) with its energy deposition in both EM and Hadronic calorimeters are shown.

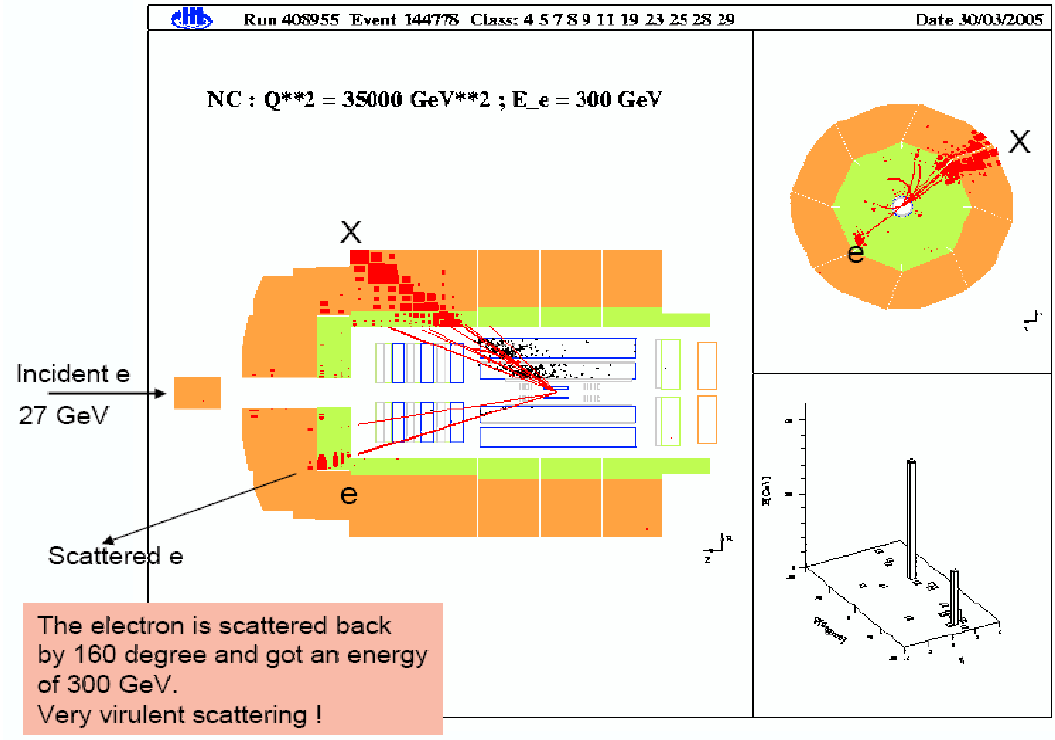

Figure D.5: Shows a NC DIS event with a single jet.

Figure D.6 shows a NC scattered electron with final state QED radiation. The scattered electron radiated a photon which subsequently converts to an electron and anti-electron pair in the detector material. This will have the effect of altering the determined Q^2 of the scattered electron, due to a shift in its position within the detector if the electron and photon are detected as one object and due to a shift in both the energy and position if not. The effect of the final QED radiation has been accounted for in this work by the precise determination of this of its effect on simulated events.

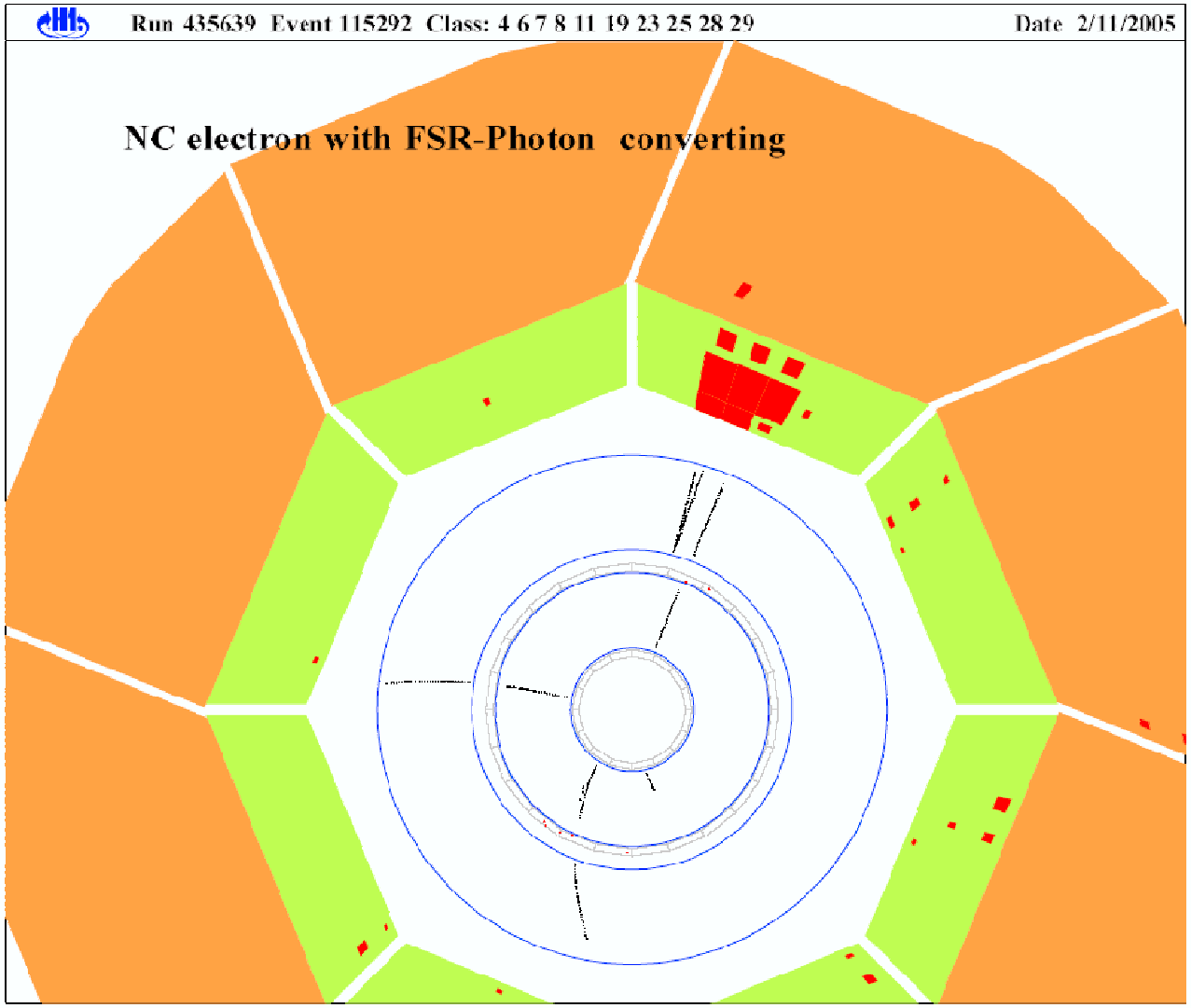

Figure D.6: Shows a scattered electron with final state QED radiation.

References

[1] C. Adloff et al. [H1 Collaboration], Phys.Lett. B 528(2002) 199 [hep-ex/0108039].

[2] H1 Collaboration, I.Abt et al., The H1-detector at HERA, Nucl. Instrum. Meth, **A386** (1997) 310 and 348, DESY-H1-96-01.

[3] J.Burger et al., The Central Jet Chamber of the H1 Experiment, Nucl. Instrum. Meth.**A279** (1989) 217.

[4] S.Egli et al., The Central-Inner Z-Drift Chamber of the H1 Experiment,Nucl. Instrum. Meth. **A283** (1989) 487.

[5] K.Muller et al., Construction and Performance of Thin Cylindrical Multi-wire Proportional Chamber with Cathode Pad Readout for H1 Experiment, Nucl. Instrum. Meth. **A312** (1992) 457.

[6] D.Pitzel et al., The H1 silicon vertex detector, Nucl. Instrum. Meth.**A454** (2000)334.

[7] M.Kausch-Blecken von Schmeling, The silicon microvertex detector of the H1 Experiment: Readout, event reconstruction, and studies on heavy quark decays DESY-THESIS 1998-033.

[8] Collaboration, I.Abet et al., Technical Proposal for the Upgrade of Backward Region of the H1 Detector, DESY Internal Report, **PRC-93-02.**

[9] H1 Calorimeter Group, B.Andrieu et al., The H1 Liquid Argon Calorimeter System., Nucl. Instrum. Meth. **A336** (1993) 460.

[10] "Group, H1 SpaCal; R.D.Appuhn et al, Hadronic Response and e/Pion Separation with the H1 Lead/Fiber Calorimeter,NIM,A 382." [(1996)395.],

H1 SpaCal Group, R.D Appuhn et al., The H1 Lead/Scintillating-fibre Calorimeter, Nucl. Instrum. Meth. **A386** (1997) 397,

H.Bethe and W.Heitler, On the Stopping of Fast Particles and on Creation of Positive Electrons, Proc.Roy.Soc.Lond. **A146** (1934) 83.

[11] H1 Collaboration, Luminosity Measurement in the H1 Experiment at HERA,Contributed paper to ICHEP96, Warsaw 1996, **ICHEP96pa17-026**.

[12] E.Elsen. The H1 Trigger and Data Acquisition, contributed paper to International Symposium on Electronic Instrumentation in Physics, Dubna 1991.H1 Internal Note, **H1-IN-262** (01/1993).

[13] J.C. Bizot et al., Status of Simulation for a Topological Level 2 Trigger, H1 Internal Note, **H1-IN-212** (02/1997).

[14] J.H.Kohne et al., Realisation of a Second Level Neural Network Trigger for the H1Experiment at HERA, H1 Internal Note, **H1-IN-509**(01/1997).

[15] H.Beck, Principle and Operation of the z-Vertex Trigger, H1 Internal Note,**H1-IN-479** (05/1996).

[16] Andreas Meyer, Measurement of Structure Function f2(x,Q2) of the Proton at Low Q2 with the H1 Detector at HERA using the new detector components SpaCal and BDC, DESY THESIS 1997.

[17] R.Burn et al., GEANT3 User's Guide, **CERN-DD/DD-84-1**.

[18] F.E.Close , An Introduction to Quarks and Partons, Rutherford Laboratory, Academic Press(1979).

[19] R.Feynman, Phys.Rev.Lett.23 (1969) 1415.J.Bjorken.E.Pascho, Phys.Rev, 185 (1969) 1975,

S. L. Glashow, Nucl.Phys. 22, 579. 1961.

[20] A.Salam, originally printed in 'Svartholm: Elementary Particle Theory, Proceedings of the Nobel Symposium held 1968 at Lerum, Sweden'. 1968, 367-377.

[21] S.Weinberg, Phys.Rev. Lett. 19, 1264. 1967.

[22] I.J.R. Aitchison and A.J.G.Hey,. Bristol, UK: IOP, 2004.

[23] D.H.Perkins,Introduction to high energy physics. Reading,Massachusetts: Addison-Wesley, 1987. M.Kaku,Quantum Field Theory, A Modern Introduction .,New York, USA: Oxford Univ.Pr, 1993.

[24] F.E.Close, An Itroduction to Quarks and Partons,Rutherford Laboratory, Academic Press ISBN:0-12-17510-3. 1979.

[25] R.Feynman, Phys.Rev.Lett. 23, 1415, J.Bjorken.E.Pascho, Phys.Rev,185, 1975. 1969,.

[26] D.H.Perkins, Introduction to high energy physics, Addison-Wesley,. Reading, Massachusetts, 1987.

[27] G.D.Coughlan and J.E.Dodd, The Ideas of Partricle Physics,. Cambridge, UK: Cambridge University press, 1991.

[28] M.E.Peskin and D.V.Schroeder, An Introduction to Quantum Field Theory,. Reading Massachusetts,: Perseus Books, 1995.

[29] A.Cooper-Sarkar, R.Devenish,Deep Inelaric Scattering. Oxford: Oxford University Press, 2004.

[30] ZEUS Collaboration, Combined ZEUS & H1 Plots for Moriond EW, **moriond04/zeush1.php(2004).** http://www.zeus.desy.de/physics/sfew/PUBLIC/sfew_results/preliminary/, 2004.

[31] F.Halzen and A.D.Martin, Quarks and Leptons: An Introductory Course in Modern Particle Physics. New York: John Wiley & Sons, 1984.

[32] V.Gribov et al., Sov.J.Nucl.Phys.**15**. 1972, 438.

[33] G.Altarelli, G. Parisi, Nucl.Phys. **B 126.** 1977, 298.

[34] E.Kuraev, L.Lipatov, V.Fadin, Sov. Phys. JETP. 44,. 1976, 443.

[35] Y.Balitsky, L.Lipatov, Sov.J.Nucl.Phys. **28.** 1978, 822.

[36] M.Ciafaloni, Nucl.Phys.B 296,(1998) 49. S. Catani, F. Fiorani, G. Marchesini, Phys. Lett. **B 234**, (1990) 339. S. Catani, F. Fiorani, G. Marchesini, Phys. Lett. **B 336**, (1990) 18.

[37] V.Fadin. L.Lipatov, Phys.Lett. **B 246. (**1998) 127. G.Camici.M.Ciafaloni,Phys.Lett. **B 430**, (1998) 349. S. Brodsky. G.Lepage, P.Mackenzie, Phys.Rev. **D 28**, (1983) 228.

[38] J.C. Collins, D.E.Soper and G.Sterman, Adv, Ser.Direct. High Energy Phys.5, 1 (1988)[hep-ph/0409313].

[39]A.D.Martin, W.J.Stirling and R.G.Roberts, Phys. Rev. **D 50** (1994) 6734 [hep-ph/9406315].

[40]H.L.Lai et al., Phys.Rev. **D 55** (1997) 1280 [hep-ph/9606399].

[41] E.Laenen, S.Riemersma, J.Smith and W.L.van Neerven, Nucl.Phys. **B 392** (1993) 162;.

[42] E.Laenen, S.Riemersma, J.Smith and W.L.van Neerven, Nucl.Phys. **B 392** (1993) 229;.

[43] S.Riemersma, J.Smith and W.L.van Neerven, Phys.Lett. **B 347** (1995) 143 [hep-ph/9411431].

[44] S.Frixione, P.Nason and G.Ridolfi, Nucl.Phys. **B 454** (1995) 3 [hep-ph/9506226].

[45]B.W.Harris and J.Smith, Nucl.Phys. **B 452** (1995) 109 [hep-ph/9503484].

[46] F.I.Olness and W.K.Tung, NUcl.Phys. **B 308** (1988) 813;.

[47] M.A.G.Aivazis, J.C.Collins, F.I.Olness and W.K.Tung, Phys.Rev. **D 50** (1994) 3102 [hep-ph/9312319];.

[48] B. Andersson, G. Gustafson, G.Ingelman and T.Sjostrand, " Parton fragmentation and string dynamics" , Phys.Rept. 97 (1983) 31.

[49] C.Peterson, D. Schlatter, I.Schmitt and P.M.Zerwas, "Scaling violations in inclusive e+e- annihilation spectra", Phys. Rev. **D 27** (1983) 105.

[50] P.Nason and C.Oleari, " A phenomenolgical study of heavy-quark fragmentation function in e+e- annihilation", Nucl.Phys. **B565** (2000) 245-266, hep-ph/9903541.

[51] H.Jung,Comput.Phys.Commun.86(1995)147;(see also http://www.desy.de/~jung/rapgap/).

[52] H.Jung and G.P.Salam, Eur.Phys.J.**C 19** (2001) 351 [hep-ph/0012143].

[53] T.Sjostrand,L.Lonnblad and S.Mrenna, arXiv:hep-ph/0108264.

[54] A.Kwiatkowski, H.Spiesberger and H.J.Mohring, Comput.Phys.Commun.69 (1992).

[55] R.Brun, R. Hagelberg, M. Hansroul and J.C.Lassalle, **CERN-DD-78-2-REV**.

[56] S.Bentvelson, J.Engelen and P.Kooijman, Proceedings of the Workshop "Physics at HERA", vol.1, DESY. (1991) 23.

[57] U.Bassler and G.Bernardi, Nucl.Instrum.Meth. **A 361** (1995) 197 [hep-ex/9412004].

[58] M.Peez, B.Portheault, and E.Sauvan,"An energy flow algorithm for Hadronic Reconstruction in OO: Hadroo2," H1 Internal Note **H1-01/05-616.**

[59] H1 Collaboration. C. Adloff et al, Deep-inelastic ep scattering at low x and a determination of Alpha s, Eur.Phys.J. **C21** (2001) 33. [hep-ex/0012053].

[60] H1 Collabroration, A.Aktas et al., Measurement of F_2 CCBar and F_2 BBBar at low Q^2 and x using the H1 vertex detector at HERA, Eur.Phys.J. **C45**(2005) 23, [hep-ex/0507081].

[61] H1 Collaboration, C.Adloff et al. Eur.Phys.J.**C13** (2000) 609.

[62] S.D.Ellis and D.E.Soper, Phys.Rev. **D 48** (1993) 3160 [hep-ph/9305266].

[63] L.Gladilin, Charm hadron production fractions (1999), [hep-ex/9912064].

[64] D.Abbaneo et al., LEP/SLD Heavy Flavour Working Group (2004), **LEPHF 2001-01**.

[65] S.Eidelman et al., Review of Particle Physics, Phys.Lett. **B592**(2004) 1,http://pdg.lbl.gov.

[66] ALEPH Collaboration, D.Buskulic et al, A precise measurement of $\Gamma_{z\to b\bar{b}}/\Gamma_{z-hadrons}$, Phys.Lett. B 313 (1993) 535.

[67] H1 Collaboration, A.Aktas et al., Measurement of $F_2^{c\bar{c}}$ and $F_2^{b\bar{b}}$ at high Q2 using H1 Vertex Detector at HERA, Eur.Phys. J.C40(2005) 349, [hep-ex/0411046].

[68] J.Gassner, "A Measurement of D-Meson Production at HERA by Decay Vertex Indentification," PhD thesis, Swiss Federal Inst. of Technology Zürich, 2002, **ETHZ No.14774**.

[69] O.Behnke, J. Kroseberg, " CSTLIN: Combined CJC-CST Track Fit," H1 internal note.

[70] M.Kausch " The Silicon Microvertex Detector of the H1 Experiment:Readout, Event Reconstruction, and Studies on Heavy Quark Decay," PhD thesis, Univ. Hamburg, 1998, DESY-THESIS-1998-0333.

[71] O.Behnke, H1 internal document.

[72] QHQTRK manual, (Heavy Flavour Working Group track selection code by Lee West).

[73] **CERN-TH/95-176**, talk given at the 10th Topical Workshop on Proton-Antiproton Collider Physics, Batavia, IL, May 9-13, 1995.

[74] H.C.Schultz-Coulon et al., IEEE Trans.Nucl.Sci. 46 (1999) 915.

[75] H1 Tracking Group, http://www-h1.desy.de/idet/itrack/TrackingGroup/home.html, H1 internal document.

[76] Particle Data Group Collaboration, K.Hagiwara et al, Review of particle physics, Phys. Rev.**D66** (2002). n.d.

[77] L.Gladilin, Charm hadron production functions (1999), [hep-ex/9912064].

[78] MARK-III Colaboration, D. Coffman et al, Measurement of the inclusive decay properties of charmed mesons, Phys. Lett. **B263**(1991) 135.

[79] D.Abbaneo et al., LEP/SLD Heavy Flavour Working Group (2004), **LEPHF 2001-01**.

[80] M.G.Bowler, Z. Phys.**C 11** (1981) 169.

[81] H1 Collaboration, C.Adloff et al., Deep-inelastic inclusive ep scattering at low x and a determination of Alpha_s, Eur.Phys.J.**C21**(2001)33, [hep-ex/0012053].

[82] Andreas.B.Meyer, "Heavy Quark Production at Hera" Habilitationsschrift, Hamburg, Desy (2005).

[83] A.Baird et al., IEEE Trans. Nucl.Sci. 48 (2001) 1276 [hep-ex/0104010].

[84] P.Bate "High Transverse Momentum 2-Jet and 3-Jet Cross Section Measurements in Photoproduction" Desy Thesis-h1th-184.

[85] H.Jung, The CCFM Monte Carlo generator CASCADE, Comput. Phys. Commum. 143(2002) 100, [hep-ph/0109102].

[86] V.V. Sudakov, Vertex parts at very high-energies in quantum electrodynamics,Sov. Phys. JETP 3 (1956) 65.

[87] E.Chabert et al, H1 Internal Note H1-1198-556(1998).

[88] C.Adloff et al., [H1 Collaboration], Eur.Phys.J.C 13 (2000) 609 [hep-ex/9908059].

[89] B.Anderson, et al., Phys. Rep. 97 (1983) 31.

[90] D.J.Gross and F.Wilczek, Phys, Rev. Lett. 30 (1973) 1343; Phys.Rev.D8 (1973) 3633; H.D.Politzer, Phys.Rev.Lett. **30**(1973) 1346.

[91] M.Bace, Phys.Lett.**B 78** (1978) 132.